

# Linking Central Valley Deep Aquifer Recharge and High Sierra Nevada Snowpack

Susanna Werth<sup>1</sup>, Manoochehr Shirzaei<sup>2</sup>, Grace Carlson<sup>3</sup>, and Roland Bürgmann<sup>4</sup>

<sup>1</sup>Virginia Tech

<sup>2</sup>Arizona State University

<sup>3</sup>Virginia Polytechnic and State University

<sup>4</sup>University of California, Berkeley

March 13, 2023

## Abstract

California's arid Central Valley relies on groundwater pumped from deep aquifers and surface water transported from the Sierra Nevada to produce a quarter of the United States' food demand. The natural recharge to deep aquifers is thought to be regulated by the adjacent high Sierra Nevada mountains, but the underlying mechanisms remain elusive. We investigate large sets of geodetic remote sensing, hydrologic, and climate data and employ process-based models at annual time scales to investigate possible recharge mechanism. Peak annual groundwater storage in the Central Valley lags several months behind that of groundwater levels, which suggests a longer transmission time for water flow than pressure propagation. We further find that peak groundwater levels lag the Sierra Nevada snowmelt by about one month, consistent with an ideal fluid pressure diffusion time in the Sierra's fractured crystalline body. This suggests that Sierra Nevada snowpack changes likely impact freshwater availability in the Central Valley aquifers. Our datasets, analysis and process-based models link the current precipitation and meltwater in the high mountain Sierra to deep Central Valley aquifers through the mountain block recharge process. We call for new hydroclimate models to account for the role of the Sierra in California's water cycle and for revision of the current management and drought resiliency plans.

## Hosted file

957869\_0\_supp\_10769542\_rr2dfz.docx available at <https://authorea.com/users/546649/articles/629105-linking-central-valley-deep-aquifer-recharge-and-high-sierra-nevada-snowpack>

1 **Linking Central Valley Deep Aquifer Recharge and High Sierra Nevada Snowpack**

2 **S. Werth<sup>1</sup>, M. Shirzaei<sup>1</sup>, G. Carlson<sup>1</sup>, and Roland Bürgmann<sup>2</sup>**

3  
4 <sup>1</sup>Department of Geosciences, Virginia Polytechnic Institute and State University, Blacksburg,  
5 VA, USA.

6 <sup>2</sup>Dept of Earth and Planetary Science, University of California, Berkeley, CA, USA.

7 Corresponding author: Susanna Werth ([swerth@vt.edu](mailto:swerth@vt.edu))

8  
9  
10 **Key Points:**

- 11 • High Sierra snowpack link to deep Central Valley aquifers via mountain block recharge  
12 is consistent with satellite & in-situ observations.
- 13 • Peak groundwater levels lag Sierra's water peak by one month, consistent with fluid  
14 diffusion time in Sierra's fractured crystalline body
- 15 • New hydroclimate models should account for the role of the Sierra Nevada in  
16 California's water cycle  
17

## 18 **Abstract**

19 California's arid Central Valley relies on groundwater pumped from deep aquifers and  
20 surface water transported from the Sierra Nevada to produce a quarter of the United States' food  
21 demand. The natural recharge to deep aquifers is thought to be regulated by the adjacent high  
22 Sierra Nevada mountains, but the underlying mechanisms remain elusive. We investigate large  
23 sets of geodetic remote sensing, hydrologic, and climate data and employ process-based models  
24 at annual time scales to investigate possible recharge mechanism. Peak annual groundwater  
25 storage in the Central Valley lags several months behind that of groundwater levels, which  
26 suggests a longer transmission time for water flow than pressure propagation. We further find  
27 that peak groundwater levels lag the Sierra Nevada snowmelt by about one month, consistent  
28 with an ideal fluid pressure diffusion time in the Sierra's fractured crystalline body. This  
29 suggests that Sierra Nevada snowpack changes likely impact freshwater availability in the  
30 Central Valley aquifers. Our datasets, analysis and process-based models link the current  
31 precipitation and meltwater in the high mountain Sierra to deep Central Valley aquifers through  
32 the mountain block recharge process. We call for new hydroclimate models to account for the  
33 role of the Sierra in California's water cycle and for revision of the current management and  
34 drought resiliency plans.

35

## 36 **Plain Language Summary**

37 Current trends in hydrology and climate indicate a future in which extreme droughts will likely  
38 become the norm for drier regions. To sustain food production in the Central Valley, California,  
39 a major agricultural producer in the United States with a semiarid climate, groundwater supply  
40 and recharge are crucial to management solutions. We report the first remote-sensing  
41 observations directly linking Sierra Nevada's snowpack and groundwater storage to Central  
42 Valley's deep aquifer system recharge. We highlight the importance of high mountain  
43 groundwater systems in the water cycle, significantly contributing to recharging valley aquifers.  
44 We suggest that Sierra Nevada snowmelt and mountain recharge processes should be included in  
45 Central Valley aquifer models for accurate forecasting of the impact of climate extremes on  
46 groundwater supply and for developing effective drought adaptation and resiliency plans.

47

## 48 **1 Introduction**

49 Understanding key natural and artificial processes in recharging aquifer systems is  
50 essential for sustainable water management to store water for future use (Escriva-Bou et al.,  
51 2020, 2021; Ghasemizade et al., 2019). In arid and semiarid regions, such as the lowland Central  
52 Valley (CV) of California adjacent to the Sierra Nevada Mountains (Fig. 1a), artificial (or  
53 intentional) recharge through basins, unlined canals, and injection contributes to the net recharge,  
54 however, due to the natural disconnect between groundwater overdraft in dry areas and surface  
55 water surplus in wet areas, these contributions are likely small (Alley, 2002; Ayres et al., 2021;  
56 Escriva-Bou et al., 2021; Siebert et al., 2010; Zektser & Everett, 2004). Thus, large-scale natural  
57 recharge to deep aquifers is essential for replenishing dryland groundwater resources. In contrast  
58 to artificial recharge, the mechanism of natural recharge to deep aquifers remains elusive in the  
59 CV.

60 California's wet and dry seasons occur during November-April and May-October,  
61 respectively, with a large portion of the Sierra Nevada's precipitation falling as snow during the  
62 winter that supplies snow melt in spring (Fig. S1, S2). The Sierra Nevada's snowpack is thought  
63 to regulate surface water availability in the CV during the summer (Faunt, 2009; Peterson et al.,  
64 2003; Urióstegui et al., 2017). Isotope studies and streamflow analysis of snow-dominated  
65 mountainous watersheds of the western USA suggest that snowpacks via snowmelt significantly  
66 contribute to groundwater recharge, depending on present geology (Earman et al., 2006; Tague et  
67 al., 2008; Tague & Grant, 2009). But the mechanism linking the Central Valley's deep aquifer  
68 recharge to precipitation, underground storage, and water transport in the Sierra Nevada  
69 Mountains is not well-understood (Huth et al., 2004; Jódar et al., 2017; Liu et al., 2017).

70 Deep valley aquifers adjacent to high mountains, such as the CV, are thought to be  
71 recharged by lateral flows from higher elevations (Feth, 1964). The two main processes  
72 considered are Mountain Front Recharge (MFR) and Mountain Block Recharge (MBR, Fig. 2)  
73 (Somers & McKenzie, 2020). MFR often directly recharges shallow unconfined aquifers and  
74 causes a rise in the water table near streambeds from the mountain front to the basin aquifer.  
75 MBR replenishes deeper, often confined, and semi-confined aquifers laterally connected to high  
76 mountain aquifers (Somers & McKenzie, 2020). MBR occurs through fractures in the mountain  
77 block hydraulically connected to deep valley aquifers. Despite their proximity, there is no  
78 consensus on the role of especially MBR from the Sierra Nevada's granitic bedrock block into  
79 the CV aquifers; thus, it is not considered in current large-scale hydrological models used in  
80 water management assessments (Faunt, 2009; Hanson et al., 2012; Markovich et al., 2019).  
81 Meixner et al. (2016) lumped both processes to mountain system recharge (MSR) and estimated  
82 that it accounts for ~20% of GW recharge in the CV. Recent modeling experiments indicate that  
83 MFR drives almost all of the MSR to the CV aquifers (Schreiner-McGraw & Ajami, 2022).  
84 However, another study based on hydrological modeling concludes that MBR is more important  
85 and contributes up to 23% of the total GW recharge to the CV (Gilbert & Maxwell, 2017). These  
86 hydrogeological studies generally agree on the role of MSR components. However, they disagree  
87 on the importance of MBR for recharging deep valley aquifers of the CV, while the spatial extent  
88 of their investigations remains at scales of smaller watersheds that do not cover the entire CV.

89 An observation of groundwater volume change at the scale of the CV is available from  
90 remote sensing techniques, e.g., via their impact on the gravity field observed by the Gravity  
91 Recovery And Climate Experiment (GRACE) or on surface deformation observations with  
92 Global Navigation Satellite System (GNSS) or Interferometric Synthetic Aperture Radar  
93 (InSAR). Some studies, e.g., Murray & Lohmann (2018), Neely et al. (2021) analyzing high-  
94 resolution deformation maps, suggest direct recharge of deep aquifers from the surface of the CV  
95 following heavy precipitation events and surface water supply surplus during wet years, ignoring  
96 the impermeable clay layers separating shallow and deep aquifers (Faunt, 2009; Shirzaei et al.,  
97 2019) and that there is no evidence of vertical fractures (Carlson, Shirzaei, Ojha, et al., 2020) in  
98 the Valley to provide a direct pathway for the downward flow of surface water. Argus et al.  
99 (2022) use remote sensing data and hydrological models to quantify MBR from the Sierra  
100 Nevada to the CV at about 5 km<sup>3</sup>/yr, though they fail to provide a feasible conceptual or physical  
101 model describing the deep aquifer recharge mechanisms.

102 Quantifying the spatiotemporal relationship between California's high mountains and  
103 deep valley aquifers is essential for developing appropriate plans supporting sustainable  
104 groundwater use. In the climate change era, when drought frequency and intensity have

105 increased globally (Fox-Kemper et al., 2021), including in California (Fig. S3), elevation-  
106 dependent warming (Pepin et al., 2015) disproportionately impacts the water availability and  
107 storage in high mountains. During the last decades specifically, increased evapotranspiration,  
108 decreased or delayed precipitation, and snowfall have caused severe snow droughts in the  
109 western USA, including the Sierra Nevada (Harpold et al., 2017; Hatchett & McEvoy, 2018;  
110 Mote et al., 2018). These droughts also reduce supply for the MBR. Hence, ignoring the MBR  
111 contribution may cause an overestimation of the lowland aquifer resilience to climate change and  
112 excess freshwater demand.

113 During a dry year, up to 70% of the groundwater used in CV is pumped within the  
114 growing season, mainly between April to June (Faunt, 2009), causing a long-term decline in  
115 groundwater levels, with the fastest rates observed in the southern San Joaquin basin (Fig. 1a,  
116 including the Tulare basin) (Faunt, 2009; Faunt et al., 2016; Konikow, 2015; Massoud et al.,  
117 2018; Ojha et al., 2018). Given the poor quality of shallow water in the southern CV (Hanak et  
118 al., 2017), most groundwater demand is addressed by tapping into deep aquifers at ~50 m to  
119 ~500 m depth below the surface, overlain by the confining layer of the Corcoran Clay or other  
120 clay lenses (Fig. 1a). Thus, direct percolation of surface water into deep aquifers is implausible  
121 (Shirzaei et al., 2019), at least at the time scale of a month to a year, corroborated by  
122 groundwater-age data (McMahon et al., 2011). For instance, Burow et al., (2007) reported a  
123 recharge rate of less than 600 mm/yr for unconfined aquifers in San Joaquin Valley. Thus,  
124 ancient groundwater supports California's water supply today (Healy & Scanlon, 2010).

125 Here, we investigate several big time-dependent datasets, including groundwater level  
126 (GWL, Fig. 1a, S4), surface deformation from Interferometric Synthetic Aperture Radar (InSAR)  
127 and Global Navigation Satellite System (GNSS) (Fig. 1b, S5), Gravity Recovery and Climate  
128 Experiment (GRACE) satellite-derived total water storage (TWS), as well as soil storage (SoS),  
129 snow storage (SnS) and reservoir storage (ReS, Fig. 1c) from hydrological data sources. We  
130 further apply sophisticated time-frequency and correlation analysis to identify hidden and non-  
131 stationary patterns in time series, quantifying their relationships. We specifically focus on  
132 investigating seasonal (i.e., annual) variations in hydrologic and geodetic observation time series  
133 that are sensitive to groundwater dynamics and their inter-annual differences. Based on the  
134 analysis, we build a conceptual model for CV deep aquifer recharge that supports the importance  
135 of MBR and agrees with geodetic remote sensing data over the CV.

136

## 137 **2 Materials and Methods**

138 Our study leverages various hydrologic and geodetic datasets, signal processing,  
139 statistical methods and physical models to quantify groundwater dynamics in the CV and Sierra  
140 Nevada Mountains (Fig. 1a).

### 141 **2.1. Water Storage Components, Precipitation, and Snow Melt**

142 GRACE and GRACE Follow-on missions (hereafter referred to as simply GRACE)  
143 monitor monthly changes in the Earth's gravity field at a spatial resolution of ~300-400 km,  
144 which are converted to equivalent total water storage (TWS) changes close to the surface  
145 (Schmidt et al., 2008; Tapley et al., 2004). In California, associated mass variations can be  
146 attributed to the terrestrial water cycle dynamics at sub-seasonal to interdecadal time scales.  
147 Water flow and storage processes on and below the surface change the region's total amount of

148 water stored in the soil, snowcap, surface- (including reservoirs and rivers), and groundwater.  
149 With that, GRACE total water storage variations reflect water loss, e.g., due to drought or human  
150 activities like intense groundwater pumping, as a mass deficit. Vice versa, for wetter periods, the  
151 surplus of water is detected. This allows for predicting groundwater storage in large aquifers if  
152 storage changes in all other components can be quantified and removed from GRACE TWS  
153 (Famiglietti et al., 2011; Scanlon et al., 2012).

154 Here, we derive groundwater storage (GWS) changes from GRACE observations using  
155 an approach similar to Ojha et al. (2019). We retrieve GRACE TWS variations from the RL06  
156 Level-3 product from NASA's Jet Propulsion Laboratory (JPL) that solves regional mass  
157 variations at a resolution of 3-degree. We do not apply JPL-mascon scale factors, as we calculate  
158 groundwater changes at this native resolution, and we assume leakage between the mascon tiles  
159 to be neglectable. To separate GWS changes from GRACE TWS, we retrieve mass variations in  
160 other storage compartments from multiple data sets. We acquire soil moisture variations from all  
161 available soil layers in the NOAH, CLSM and VIC models of the Global Land Data Assimilation  
162 System (GLDAS) Version 2.1 (Beaudoin & Rodell, 2016; Rodell et al., 2004) at 0.25 (Noah)  
163 and 1-degree (CLSM and VIC) resolution, respectively, for the entire GRACE period. We  
164 average the three models to one ensemble dataset for further analyses after resampling them to a  
165 uniform 0.5-degree resolution (Fig. 1c). For comparison, we also retrieve soil storage changes  
166 from the WaterGAP Global Hydrological Model (WGHM, version 2.2d) at 0.5-degree  
167 resolution, which is available until 2016 (Fig. S12a). We integrate reservoir storage (ReS)  
168 changes from 18 reservoirs with capacities larger than or equal to 0.9 km<sup>3</sup>, inside the margins of  
169 the two mascon cells covering the CV (GRACE region, Fig. 1b), which are retrieved from the  
170 California Department of Water Resources (CDWR, 2017). Snow storage (SoS) changes are  
171 acquired in the form of snow water equivalent from the Snow Data Assimilation System  
172 (SNODAS) (NOHRSC, 2004) over the contiguous United States since the end of 2003. Monthly  
173 water mass variations for each storage compartment are summed across the GRACE region and  
174 the regionally aggregated SoS, SnS and ReS variations are removed from GRACE TWS  
175 variations for this area, after Ojha et al. (2019). The resulting time series for each storage  
176 compartment, including groundwater storage changes during both GRACE mission periods, are  
177 shown in Figure 1c. We assume the GRACE based estimate of GWS to be dominated by  
178 groundwater variations in the CV, where porosity of the aquifers is much larger than that in the  
179 SN Mountains.

180 From the SNODAS dataset we further retrieve driving and output variables related to  
181 snow cover, including 'solid'- and 'liquid precipitation', and 'snowmelt runoff at the base of the  
182 snowpack', to investigate these fluxes in the Sierra Nevada Mountains (Fig. S1, S2) and their  
183 correlation to groundwater dynamics.

## 184 2.2. Groundwater Levels

185 Groundwater availability in the CV is conventionally monitored as water level change in  
186 observation and irrigation wells. The data archives from the United States Geological Survey  
187 (USGS) and the California Department for Water Resources (CDWR) provide more than 40,000  
188 records from wells within the CV. The records have varying start dates, not all are continuously  
189 monitored until today, and only some records provide sufficient temporal sampling rates to study  
190 seasonal variations in GWLs. For this study we have screened 'daily data' and 'field data'  
191 archives from the USGS (USGS, 2021) as well as 'continuous data' and 'periodic data' archives

192 from CDWR (CDWR, 2019) in California and selected records that cover the GRACE mission  
193 period from 2002 to 2020. We have excluded records labeled as ‘irrigation well’ and only  
194 selected sites labeled ‘observation well’. Water levels in irrigation wells are potentially affected  
195 by the localized reduction in pressure during and after pumping from the well. Levels in  
196 observation wells are more likely to represent a regional state of pressure and storage changes in  
197 the entire aquifer. In addition, we categorized data entries that are larger than 3.5 times the  
198 standard deviation of the detrended time series as outliers and excluded them. Moreover, about  
199 half of the records have daily sampling rates and we excluded entire records from the  
200 field/periodic datasets that have less than six entries per year on average. From the initial dataset,  
201 2128 time series (371 from USGS and 1727 from CDWR) provide observation records during  
202 2002-2020 inside the CV. Only 682 records cover at least three years with less than 3 months of  
203 gap (Fig. S4); of those, we select 457 records gathered at depths deeper than 50 m since we want  
204 to focus on time series measured in semi-confined and confined aquifers. About half of the 457  
205 available records are longer than 10 years (Fig. S4a-c). We note that these records were taken at  
206 only 250 unique well locations (circles in Fig. 1a), with some sites containing up to five nested  
207 level meters (Fig. S4d). Most deep sensors at each site are located 50 m to 300 m below the  
208 surface, with about half of the sensors reaching not more than 200 m deep and only a few are 450  
209 m deep or deeper (Fig. 1a, S4e, f). Most usable wells are in the northern Sacramento Valley and  
210 only two dozen sites are in the southern San Joaquin Valley, where only 22 wells measure water  
211 level variations at depths below the Corcoran clay. Examples of GWL time series are shown in  
212 Figure 1a.

### 213 2.3. Surface deformation

214 Surface deformation due to TWS change, including GWS, occurs through two different  
215 processes. Total water mass deforms Earth’s elastic crust, resulting in subsidence for an increase  
216 and uplift for a decrease in water mass. This deformation process has been described and  
217 inverted to quantify TWS in California (Adusumilli et al., 2019; Argus et al., 2022; Borsa et al.,  
218 2014; Carlson et al., 2022; Carlson, Shirzaei, Werth, et al., 2020; White et al., 2022). A second  
219 poroelastic deformation process is due to only groundwater changes occurring in semi-confined  
220 or confined aquifers, where pore spaces and granular matrix of rocks compact and groundwater  
221 levels fall under reduced water pressure. The opposite happens for increasing water pressure.  
222 Changes in water pressure in an aquifer can either be caused by net recharge or discharge, i.e.  
223 GWS change, in the aquifer itself, or initiated by water pressure propagating between the aquifer  
224 and a hydraulically connected outside region (Fetter & Kreamer, 2022). Decades of falling  
225 groundwater levels in the CV deep aquifers have caused continuous land subsidence at the  
226 surface and have been observed to be most severe during droughts (Galloway et al., 1999; Ojha  
227 et al., 2018; Smith et al., 2017; Vasco et al., 2022). It has been shown that elastic loading  
228 deformation in California is of the opposite sign and up to two magnitudes smaller than the  
229 poroelastic deformation occurring at the surface of the CV (Carlson, Shirzaei, Werth, et al.,  
230 2020).

231 To study seasonal variations in vertical land motion (VLM) since the early 2000s, we use  
232 vertical deformation time series from the daily tenv3 GNSS solutions from the Nevada Geodetic  
233 Laboratory (NGL). The solutions are processed at NGL using GipsyX software and are  
234 transformed into the IGS14 reference frame. Additional processing information can be found on  
235 the NGL website (<http://geodesy.unr.edu/gps/ngl.acn.txt>). We do not apply any further  
236 corrections to the GNSS time series for the rest of the analysis. From 1184 stations in California,

237 we selected 170 with a minimum record of 5 years between 2002-2020 and exhibiting a seasonal  
238 amplitude larger than the time series median standard deviation. Most stations began  
239 observations around 2008, with a length of 15 years (Fig. S5b). Of these stations, 37 are located  
240 within the CV boundaries (red triangles, Fig. 1b). Example time series at three sites throughout  
241 the study area are shown in the inset of Figure 1b. We determine the seasonal component of  
242 GNSS vertical land motion and the timing of maximum uplift and maximum subsidence using a  
243 time-frequency analysis (see Section 2.4).

244 We further measure the surface deformation in terms of line-of-sight (LOS) over the  
245 southern CV using Interferometric Synthetic Aperture Radar (InSAR). The SAR dataset includes  
246 238 C-band images from descending track, path 144, of Sentinel-1A/B satellites spanning  
247 2015/11/27-2022/12/20. We apply multi-looking factors of 32 and 6 in range and azimuth to obtain  
248 a pixel dimension of  $\sim 75\text{m}$  by  $\sim 75\text{m}$ . We use GAMMA software (Werner et al., 2000) to create a  
249 large set of interferograms. The interferograms are selected, so they form triplets, and the numbers  
250 of short, medium, and long temporal baseline pairs are comparable to minimize the phase closure  
251 error impact (Lee & Shirzaei, 2023). We apply the wavelet-based InSAR (WabInSAR) (Lee &  
252 Shirzaei, 2023; Shirzaei, 2013; Shirzaei et al., 2017) algorithm to perform a multitemporal  
253 interferometric analysis of the SAR dataset and create high-accuracy maps of surface deformation  
254 time series. A Shuttle Radar Topography Mission (SRTM) Digital Elevation Model (DEM) of 1-  
255 arcsecond ( $\sim 30\text{ m}$ ) spatial resolution (Farr et al., 2007) and precise satellite orbital information are  
256 used to estimate and remove the effect of topographic phase and flat earth correction (Franceschetti  
257 & Lanari, 1999). The absolute phase values are obtained by applying a 2D minimum cost flow  
258 algorithm (Costantini, 1998), then combined to create a Line-of-Sight (LOS) time series of surface  
259 deformation by using a reweighted least squares approach. The spatially correlated and temporally  
260 uncorrelated atmospheric delay are also estimated and removed (Shirzaei, 2013).

## 261 2. 4. Time-Frequency Analysis

262 To investigate the temporal variations in water storage components, GWLs, and  
263 deformation data, we perform a time-frequency analysis using a continuous wavelet transform,  
264 following Shirzaei et al. (2013). The wavelet transform allows decomposing signals into building  
265 blocks based on frequency contents. In contrast to the Fourier transforms, the wavelets can  
266 handle non-stationary signals and localize the signal energy in the time and frequency domain  
267 (Goswami & Chan, 1999). Wavelets have a key parameter scale (or dilation), which stretches or  
268 squishes the wavelet function and relates to the analyzed signal frequency. To perform wavelet  
269 analysis, we use the Matlab packages provided by Torrence and Compo (1998) and Erickson  
270 (2019) and apply the wavelet family of derivatives of gaussian (DOG, Fig. S6) at 200 levels of  
271 decomposition or scales. The temporal sampling of all time series is either daily or resampled at  
272 daily intervals.

273 Figures 3 and S7 illustrate our approach with an example of groundwater level time series  
274 at the DWR well 387793N1218123W004 (Fig. S7a). The wavelet power spectrum map (PSM,  
275 Fig. 3a and S7b) shows the signal's energy breakdown into several frequency components and  
276 their relative importance based on the amplitude of the PSM. A cone-of-influence overprinted on  
277 the spectrum indicates areas where edge effects play a role, and therefore, the PSM cannot be  
278 interpreted. Signal energy in areas inside the cone of influence is strongest at periods of about  
279 one year, with contour lines indicating their statistical significance with respect to white and red  
280 noise (with a lag-1 autocorrelation parameter of 0.85 for the latter) (Torrence & Compo, 1998).

281 Figure 3 also shows examples of wavelet PSM for selected GWL, VLM, and TWS component  
282 time series.

283 To isolate the annual component from the time series, we set the PSM to zero except for  
284 periods between 0.75-1.25 years and then apply an inverse wavelet transform of the new PSM  
285 (Fig. S7c). This approach considers that the annual components in climate-related processes do  
286 not have an exact one-year period. We further analyze the reconstructed annual signals to  
287 characterize the timing of annual maxima, minima, and the timing of fastest rate declines and  
288 increases (blue, red, and gray circles in Fig. S7c). We summarize the annual values for several  
289 years through temporal averaging using the median operator to retrieve the timing of maximum  
290 in the annual signal (e.g., as shown in Fig. 4). The same approach is applied to the time series of  
291 GWL, TWS components, GNSS and InSAR vertical deformation.

292 Probability density functions (PDFs) for spatiotemporal variation of timing of annual  
293 peaks were calculated using MATLAB's probability density estimator *kdensity()*, based on a  
294 normal kernel function for univariate distributions and applies a kernel smoothing window with  
295 an optimized bandwidth for normal densities.

## 296 2.5. Vertical Diffusion Model

297 In the high Sierra Nevada Mountains, a significant portion of snow melt water (Fig. S1,  
298 S2) infiltrates into the ground and recharges top aquifer layers (Peterson et al., 2003; Urióstegui  
299 et al., 2017), which are hydraulically connected to the CV aquifer system (Faunt, 2009). Here, to  
300 obtain the first-order approximation of the diffusion time, namely the time it takes for snow melt-  
301 related pore-fluid pressure increase in the Sierra to reach deep aquifer layers of the CV via MBR,  
302 we apply a first-order process-based 1D diffusion model following (Saar & Manga, 2003). The  
303 vertical propagation of hydrostatic pore-fluid pressure  $P'$  at depth  $z$  over time  $t$  is governed by  
304 the diffusion equation:

$$305 \quad \kappa \frac{\partial^2 P'}{\partial z^2} = \frac{dP'}{dt} . \quad (1)$$

306 with the hydraulic diffusivity  $\kappa = K/S_s$ , which controls how fast pressure will propagate to  
307 depth. It is given by the ratio of vertical hydraulic conductivity  $K$  to specific storage  $S_s$ . The  
308 diffusivity of unfractured granite bedrock has values of around  $\kappa = 10^{-4} \text{ m}^2/\text{s}$  (Wang, 2000).  
309 However, for fractured volcanic rock, values as high at  $0.3 \text{ m}^2/\text{s}$  (Saar & Manga, 2003), and  $1$   
310  $\text{m}^2/\text{s}$  (Gao et al., 2000), consistent with the range provided by Talwani and Acree (1985), or  
311 even up to  $7.9 \text{ m}^2/\text{s}$  (Montgomery-Brown et al., 2019) are suggested. Here, we consider  
312 diffusivity values of 0.1, 0.3 and  $0.5 \text{ m}^2/\text{s}$  for Sierra's crystalline fractured rocks.

313 We solve the parabolic differential Equation 1 using the function *pdepe()* from the  
314 Matlab software by setting the initial pressure conditions to zero and the boundary conditions of  
315 the pore-fluid pressure to a periodic variation with periodicity  $\psi$  of 1 year, annual amplitude  
316  $P_{max}$  and annual phase  $\varphi_0$ :

$$317 \quad P'_{z,t=0} = P_{max} \cdot \cos\left(\frac{2\pi}{\psi} t + \varphi_0\right), \quad (2)$$

318 where at depth  $z$ , pore-fluid pressure is  $P_{z,t} = P_{z,t-1} + P'_{z,t}$ . We are only interested in changes  
319  $P'_{z,t}$  of pore-fluid pressure.

320 Assuming saturated conditions and solving Equations 1 and 2 for  $t$  allows us to estimate  
 321 the time it takes to increase pore-fluid pressure annually due to groundwater recharge reaching  
 322 vertically from top groundwater layers to depth  $z$ . The duration of pressure propagation to deep  
 323 aquifer layers is independent of the amplitude of pressure change at the surface and a normalized  
 324 solution for  $P'_{z,t=0}/P_{max}$  is sufficient. The time delay estimate is most sensitive to the  
 325 magnitude of the hydraulic diffusivity  $\kappa$  (Eq. 1) as well as the phase  $\varphi_0$ , of the annual pressure  
 326 variation due to recharge (Eq. 2). We assume that the horizontal diffusivity of the aquifer is large  
 327 enough, so the lateral diffusion time is relatively negligible (Fetter & Kreamer, 2022).

328 The annual phase of pressure variations in upper groundwater layers in the high Sierra  
 329 Nevada Mountains  $\varphi_0$  may be derived from the annual variation in water available for recharge  
 330 in this region, which we quantify as follows. The top groundwater layers in the Sierra Nevada  
 331 receive inflow from snow melt water and liquid precipitation (i.e., rainfall). Urióstegui et al.  
 332 (2017) and Bales et al. (2011) found that only 10-20% of the snow melt water in the Sierras runs  
 333 off through streams, with the remainder being lost to drainage into deep layers and  
 334 evapotranspiration. We assume that all of the melt water initially increases pressure in the upper  
 335 groundwater layers of the Sierra Nevada Mountains, before evaporating or running off. Also, we  
 336 neglect the delay between the time that water for infiltration becomes available and its  
 337 percolation into the upper groundwater layers of the Sierra Nevada Mountains. We consider  
 338 these assumptions reasonable for wide areas of exposed fractured bedrock and given that we are  
 339 only interested in quantifying the phase, not the absolute value of maximum pressure variations.  
 340 For that, we retrieve the time series of SNODAS dataset variables ‘snowmelt runoff at the base  
 341 of the snowpack’  $M$  and ‘liquid precipitation’  $P_{liqu}$  (see Section 2.1, Fig. S1) averaged for the  
 342 drainage area of the Sierra Nevada toward the CV (rose-shaded area in Fig. 1a). We correct  
 343 liquid precipitation for canopy interception by a relative value of 20% (Vrugt et al., 2003), as this  
 344 intercept changes the relative amplitudes between  $M$  and  $P_{liqu}$ , and therefore, it can impact the  
 345 annual phase. Finally, we get a time series of total water available for recharge in the Sierra  
 346 Nevada drainage area from  $(P_{liqu} - 0.2 \cdot P_{liqu} + M)$  and quantify monthly mean values of this  
 347 time series during 2002-2020 (Fig. S2c). We also determine the mean timing of the annual peak  
 348 for each year and at each location in the drainage area, which we apply as the timing of the  
 349 annual maximum of the pressure variation to constrain  $\varphi_0$  for the boundary condition in  
 350 Equation (2).

## 351 4 Results

### 352 4.1. Year-to-Year Water Variability

353 The time series of TWS variations obtained from the GRACE satellites (Tapley et al.,  
 354 2004, 2019) and their components measured through in-situ observations (e.g., wells) (Alam et  
 355 al., 2021) or water balance models (Faunt, 2009; Li et al., 2018) are characterized by annual  
 356 variations attributed to overall dynamics in the terrestrial water cycle (Tang & Oki, 2016).  
 357 Several example time series are shown in Figure 1c. A less obvious pattern comprises the  
 358 interannual variations in the amplitude of the annual signal. Identifying the amplitude and timing  
 359 of the peak annual and interannual signal components allows for resolving the temporal scale at  
 360 which the connected systems interact.

361 To this end, we apply the wavelet-based time-frequency analysis to extract hidden  
 362 patterns in the datasets (see Section 2.2.1, Fig. S6). The results from the time-frequency analysis

363 are shown in the form of a PSM, distributing the signal's power into frequencies (or periods) and  
 364 time intervals (Fig. 3, S7). We find maximum amplitudes characterize the PSMs associated with  
 365 different time series at equivalent periods of 1 year and 3-8 years (Fig. 3). These frequency  
 366 components are associated with general variations in water availability associated with  
 367 atmosphere-ocean interactions, influencing water cycles in the Southwest USA (Quiring &  
 368 Goodrich, 2008). Significant drought periods, such as during 2007-2009 and 2012-2015 (Fig.  
 369 S3), correspond with cool phases of El Niño Southern Oscillation (ENSO) recurring every 3-7  
 370 years, the cool phase of the Pacific Decadal Oscillation (PDO), and the warm phase of the  
 371 Atlantic Multidecadal Oscillation (AMO) (McCabe et al., 2004; Quiring & Goodrich, 2008). The  
 372 length of our observation does not allow for resolving signal components over a decade or  
 373 longer, as indicated by the cone of influence, the shaded region in the PSM.

374 Some PSMs also show unique patterns. For instance, the PSMs of GWL changes (Fig.  
 375 3a) and GNSS VLM (Fig. 3b) exhibit components at periods of 0.5 and 3 years, albeit the  
 376 component of 0.5 years for VLM disappears following 2008. In contrast, the PSM of SnS (Fig.  
 377 3e) shows only a transient component over a period of 3 years. PSM of GWS variations (Fig. 3g)  
 378 shows a transient component of 1 year period. Notably, the location and amplitude of peak PSM  
 379 are not constant and change over time, especially for TWS, SnS, ReS, and GWS variations and  
 380 to a lesser extent in SoS due to water availability changes within wet and dry seasons and in  
 381 between them as well as due to human interventions. For instance, the amplitude of annual  
 382 components was reduced or diminished during the drought years 2007-2010 and 2012-2015.  
 383 During these periods, reservoirs were not refilled, and the Sierra Nevada received little  
 384 precipitation, reducing the amplitude of the corresponding annual components (Fig. 3e and 3f).  
 385 The amplitude of the annual component of GWS variations vanishes during the same years (Fig.  
 386 3g).

387 Figure 3h presents the isolated annual components for all the time series comprising PSM  
 388 components of 0.75 to 1.25 yr periods, which display non-stationary behaviors, i.e., the  
 389 amplitude changes over time. We find that year-to-year TWS is experiencing the most  
 390 pronounced changes and GWS the least. We also note that year-to-year peak extremes do not co-  
 391 occur for different time series. For instance, during the 2012-2015 drought, TWS, SoS, and ReS  
 392 variations experienced their lowest amplitudes in 2013 and 2014, while that of GWS occurred  
 393 two years later during 2016, following the snow-poor years in 2014 and 2015. Characterizing  
 394 such inter-annual variability in water cycle components improves understanding of hydroclimate  
 395 extremes and water storage capacity in the region (Yin & Roderick, 2020).

396

#### 397 4.2. Timing of the Seasonal Signal

398 We further investigate the spatial variability of the timing of the peak annual amplitude of  
 399 TWS and its components across the study region (Fig. 4). Note that spatial detail cannot be  
 400 resolved from the GRACE TWS with 300-400 km spatial resolution. To this end, we find the  
 401 day-of-year (DOY) corresponding with the peak of the timeseries of the annual components and  
 402 then obtain the median of DOY for each time series. Figure 4 plots the median peak DOY for  
 403 each dataset at their original spatial resolution, except for GWL and VLM, where the values are  
 404 interpolated with an inverse distance weighting scheme and a 25 km radius. The median peak  
 405 DOY for GWL is uniform across the Valley (Fig. 4a, S8) with negligible interannual variability  
 406 (Fig. S9). GWL peaks occur from February to March (Fig. 4a, S8a) and minima in August (Fig.

407 S8b). The fastest GWL rate increase (i.e., the mid-point between annual minima and maxima)  
408 occurs during November (Fig. S8c), and the fastest GWL rate decrease (i.e., the mid-point  
409 between annual maxima and minima) occurs during May (Fig. S8d). These observations are  
410 consistent with the timing of maximum pumping in the CV during April-June. A linear  
411 correlation of 0.3 was found between observation well depth and peak DOY, indicating GWL  
412 rises slightly later in the year at deeper wells (Fig. S8a, left inset). Compared with GWL, the  
413 median peak DOY of GNSS VLM in the CV is spatially more variable (Fig. 4b and S10), with  
414 negligible interannual variability (Fig. S11). We find a bimodal distribution for this peak DOY  
415 (inset in Fig. S10a), with about a third of the stations within the CV peaking from March to April  
416 and most of the remaining stations from September to October. A bimodal behavior is also  
417 observed in the median DOY of annual VLM minima. The median DOY of the fastest VLM rate  
418 increases and decreases are also obtained (Fig. S10), indicating a smaller interannual variability  
419 than that of peak DOY (Fig. S11). We further estimate the median peak DOY of TWS, SoS, SnS,  
420 ReS, and GWS within the GRACE region (Fig. 1b), all of which show spatially uniform patterns  
421 but are distinct from each other (Fig. 4c-g), with spatial DOY averages of 93, 70, 65, 102, and  
422 156 days, respectively.

423 We performed a similar analysis using InSAR LOS deformation observations. Figure 5a  
424 shows the LOS velocity field measuring up to 18.5 cm/yr subsidence in some parts of San  
425 Joaquin Valley. We obtained seasonal phase (peak DOY) and amplitude (Fig. 5b, c) for the  
426 southern CV covered by the Sentinel-1 frame. The spatial distribution of median peak DOY  
427 generally agrees with that of GNSS (Fig. 4b). The denser spatial sampling from the InSAR  
428 analysis, however, reveals an outward propagation of the median annual peak DOY from the  
429 center of CV. Although it varies yearly, the overall outward propagating pattern of peak DOY  
430 remains similar through wet and dry years (Fig. S15). We note that this result is opposite to what  
431 was found by Neely et al. (2021), who suggested an inward propagation of the annual peak  
432 towards the center. Figures 5c and S16 show the median and yearly seasonal amplitude of  
433 surface LOS deformation, reaching up to 4 cm, with the largest value during dry years.

434 Next, we investigate the empirical probability density function (PDF) of annual peak  
435 DOY associated with all components of TWS and deformation and several other relevant  
436 hydrological datasets (Fig. 6). Shown are normalized PDFs of annual peak DOY obtained for  
437 each year and each time series without temporal averaging, thus the interannual variabilities are  
438 preserved. Comparing different PDFs, we find for the Sierra Nevada that precipitation generally  
439 peaks in early January, with a mean DOY of 16 (Fig. 6a), meltwater in late February, DOY 55  
440 (Fig. 6c), and the total water availability (combination of precipitation, meltwater, and canopy  
441 interception) in late January, DOY 22 (Fig. 6b). We obtain a wide distribution for the influxes,  
442 and years with a later maximum melt typically have a larger peak, causing the right-skewed  
443 distribution of annual peak DOY of snowmelt (Fig. S2b). The annual SoS peak for the CV  
444 occurs in March, DOY 70 (Fig. 6d), ~2-3 months after precipitation peaks. SnS peaks in March,  
445 ReS and TWS ~1 month later in April, while GWS of the CV peaks in June (Fig. 6e-g). The  
446 VLM minima (i.e., subsidence) across California, outside of the CV, co-occur with TWS  
447 maxima around April, DOY 93 (Fig. 6i). In contrast, GNSS VLM inside the CV (Fig. 6j) peaks  
448 together with GWL (Fig. 6k) around March, DOY 65, and ~3 months before GWS based on  
449 GRACE and composite hydrology (Fig. 6g). Peak VLM inside the CV derived from high-  
450 resolution InSAR maps (Fig. 6k, dashed line) have a more complex distribution, with the first  
451 peak co-occurring with GNSS and well levels around beginning of March and a later peak  
452 ranging from beginning to end of April. We further observe a delay of 43 days between total

453 water available for recharge in the Sierra Nevada Drainage area (DOY 22, Fig. 6b) and GWL in  
454 the CV (DOY 65, Fig. 6k).

455 To investigate whether the mean values of the PDFs in Figure 6 were significantly  
456 different, we performed a two-sample mean difference hypothesis test using the t-distribution  
457 (Meyer, 1970). We formulated the null hypothesis so that the mean values were the same and  
458 tested the hypothesis at a significance level of 0.05. The test was rejected, hence, the mean  
459 values are statistically the same for all pairs of PDFs in Figure 6, except between GNSS uplift  
460 (CV) and GWL (CV), between TWS and GNSS Subsidence (CA), between SnS (Sierra Nevada)  
461 and GNSS uplift (CV), and between SnS (Sierra Nevada) and GWL (CV).

462 When estimating PDFs for the timing of annual peaks of SoS and GWS (Fig. 6e and 6g),  
463 the variability among the individual SoS models was considered (Fig. S12). SoS timing varies by  
464 about ~2 months from January to February (Fig. S12c). We propagate the variation of SoS  
465 timing toward that of GWS by estimating GWS for each individual soil model (Fig. S13a). The  
466 resulting annual GWS timing varies ~2 months from May to July (Fig. S13b,c). This variability  
467 was included when calculating mean, median, standard deviation, and PDFs of annual GWS  
468 timing (Fig. 6g). Although GWS also depends on the timing of TWS, SnS and ReS, annual  
469 amplitudes of SnS and ReS are only 10% of TWS (Fig. 1c). Therefore they will only marginally  
470 impact the calculation of annual timing of GWS. We assume a minimal measurement uncertainty  
471 for the timing of TWS.

#### 472 4.3. Pressure Diffusion From the High Mountains to Deep Valley Aquifers

473 Earlier studies (e.g., Gilbert and Maxwell (2017)) have suggested that a natural  
474 connection should exist between deep CV and High Sierra Nevada mountain aquifers through  
475 the fractured granite of the mountain block. We provide a first-order estimate for the diffusion  
476 time, the time it takes for a pressure front to vertically diffuse from the top aquifer layers in the  
477 Sierra Nevada Mountains down to elevations of the deep CV aquifers (Section 2.5, Eq. 1). If we  
478 quantify that using a hydraulic diffusivity  $\kappa = 0.3 \text{ m}^2/\text{s}$  for Sierra's crystalline fractured rocks, it  
479 takes 18-36 days for the pressure to travel vertically to depth of 600-1300 m (Fig. 7). We further  
480 consider a range for the vertical hydraulic conductivity and evaluate the diffusion time for  $\kappa =$   
481  $0.1 \text{ m}^2/\text{s}$  and  $\kappa = 0.5 \text{ m}^2/\text{s}$  to depth of 600-1300 m, corresponding with 34-73 days and 12-23  
482 days (Fig. S14), respectively.

## 483 5 Discussions and Conclusions

484 This study performs time-frequency analyses of large hydrologic and geodetic datasets across  
485 California with various spatiotemporal resolutions and uncertainties to characterize the annual  
486 peak DOY, interannual peak amplitude variations, and correlative behaviors across these  
487 observations. We observe relatively low seasonal peaks during droughts for all water storages  
488 (Fig. 3h). However, only for storages in snow and groundwater wavelet PSMs vanish completely  
489 at periods of around one year during droughts when snow cover was diminished to absent during  
490 2007 and 2012-2015 (Fig. 1c, 3e, 3g). We interpret this correlation as an indicator that the  
491 volume of the snowpack and the following snowmelt played a substantial role in groundwater  
492 recharge in the CV. Once corrected for SoS, SnS, and ReS, GRACE measures a combination of  
493 GWS change in shallow and deep aquifers. Hence, we consider snow to be relevant for both  
494 MFR and MBR, with the former mechanism being more relevant for replenishing the shallow

495 and the latter more relevant for (slow) flow to the deep aquifers, given the depth of their flow  
496 path.

497 We further observe that GNSS VLM and InSAR LOS peak DOY vary across California.  
498 The peaks for stations inside the CV co-occur with that of GWL (Fig. 6j, k), specifically at the  
499 sites near the center of the Valley, where aquifer confining layers are thick and observed annual  
500 amplitudes are large (Fig. 5). This indicates the presence of poroelastic aquifer deformation due  
501 to groundwater pumping (Ojha et al., 2018; Smith et al., 2017). In contrast, the VLM peak  
502 minima for stations outside the Valley co-occur with that of TWS peak maxima (Fig. 6h, i),  
503 attributed to the variations in elastic water loading (Argus et al., 2017; Carlson et al., 2022;  
504 Johnson et al., 2017). Interannual variability in the peak amplitudes impacts the hydroclimate  
505 trends, changing baselines used to assess the future risk of climate extremes and vulnerability of  
506 water resources (Stevenson et al., 2022). In summary, a similar peak DOY suggests that some  
507 components of the hydrological system act in concert with or respond elastically to similar  
508 forcing of the hydroclimate or to anthropogenic factors. In contrast, a different peak DOY may  
509 indicate a cascading nature of the response to forcing governed by a time-dependent process.

510 Here we propose that MBR is the fundamental process, allowing long-term recharge to  
511 deep aquifers in the CV. The feasibility of this mechanism is demonstrated in Fig. 7, where a  
512 first-order process-based pressure diffusion model quantifies the lag between peak pore pressure  
513 in the Sierra Nevada aquifers due to snowmelt and peak pore pressure within deep CV aquifer  
514 layers. We estimate the lag at about a month, ignoring the lateral diffusion time, which is often  
515 negligible for permeable aquifers such as CV (Fetter & Kremer, 2022). Given the uncertainty  
516 range of hydraulic diffusivity (Somers & McKenzie, 2020), the estimated diffusion time agrees  
517 well with the lag between peak water availability in the mountains and peak water level in deep  
518 aquifers (Fig. 6b and k). This agreement supports the hypothesis that high mountain aquifers are  
519 connected to deep valley aquifers through pressure propagation from MBR, and that it drives  
520 seasonal well level changes in the deep CV aquifers. The peak GWL in March likely occurs  
521 early due to anthropogenic influence since heavy groundwater pumping typically onsetting from  
522 April to May. A later GWL peak would suggest a longer vertical diffusion time, consistent with  
523 the considered range for tested hydraulic conductivities.

524 We further observed an outward migration of the InSAR LOS peak DOY from the center  
525 of CV (Figs. 5 and S15), which is at odds with the previously published works (e.g., Neely et al.,  
526 2021) that suggested an inward propagation of annual peak DOY from the Sierra Nevada  
527 Mountains toward the center of the CV. They suggested that MFR fed by surface water flowing  
528 off the Sierra Nevada may replenish aquifers (deep and shallow) seasonally across the southern  
529 CV (Neely et al., 2021). However, the MFR mechanism is implausible to recharge deep confined  
530 aquifers (Shirzaei et al., 2019) due to the presence of the impermeable Corcoran clay layer and  
531 other clay lenses (Faunt, 2009) and little evidence of widespread vertical cracks and deep  
532 extensional fissures in the Valley (Carlson, Shirzaei, Ojha, et al., 2020) to provide a potential  
533 pathway for water to percolate deep into the aquifers, though further research on tension  
534 cracking and fissure initiation in the Valley is needed (Carlson, Shirzaei, Ojha, et al., 2020). In  
535 contrast, our hypothesis of MBR linking Sierra groundwater to deep CV's aquifers is consistent  
536 with Darcy's fluid flow law, linking the fluid discharge rate to the hydraulic head gradient  
537 between two given points, scaled with the hydraulic conductivity. Under constant hydraulic  
538 conductivity, the largest discharge happens to the point of the lowest hydraulic head. In CV, it is  
539 logical to assume the zone of the fastest subsidence rate is where the heads are lowest, consistent

540 with groundwater level observation. Thus the recharge from Sierra should replenish aquifers near  
541 the center of Valley first and then propagate outward from the center to areas with smaller  
542 hydraulic gradients, as observed here. Hence, we interpret the InSAR LOS observation of annual  
543 peak DOY as additional support for the hypothesis of a direct pressure link between the Sierra  
544 Nevada aquifers and CV deep aquifers through mountain block conduits.

545 An unexpected finding is the phase difference between annual peaks of GWL in deep  
546 confined aquifers, and GWS in the entire CV aquifer system (including confined and unconfined  
547 units, Fig. 4a, 4g, 6g and 6k) is about three months. This indicates that different processes  
548 influence GWS and well levels. In confined units, the well level change is driven by changes in  
549 groundwater storage and pore fluid pressure, while the gravity-derived measurements only detect  
550 the change in mass, hence, storage changes. During the spring, pressure rises faster in the deep  
551 aquifers than storage is recovered in the entire aquifer system. A vertical hydraulic connection  
552 via MBR flow paths would allow pressure change propagation from the mountain to CV aquifers  
553 at seasonal time scales. However, direct water seepage along MBR flow paths takes centuries to  
554 millennia (Berghuijs et al., 2022). The proposed mechanism here does not require water  
555 percolation and is consistent with the tracer findings that deep groundwater in the CV is  
556 primarily old (McMahon et al., 2011). Our results further emphasize that vertical pressure  
557 propagation occurs faster than net recharge (i.e., detected as storage change) from the mountain  
558 aquifers to the valley aquifers. The later peak in GWS might be primarily driven by annual  
559 variations in top unconfined aquifer layers (Vasco et al., 2022), which would recharge faster than  
560 deep aquifers. This is also consistent with the relatively late mean annual peak in melt water  
561 occurring during early May (see Fig. S2), hence, a long lasting supply for recharge through  
562 surface-groundwater links along the mountain fronts until late spring. At annual time scales,  
563 MFR likely contributes a significant portion to storage changes in shallow aquifers, and the  
564 seasonal variation in GRACE GWS mainly comprises such shallow aquifers instead of deep  
565 aquifers. In this case, the seasonal well level rises in deep CV aquifer layers may be driven  
566 dominantly by pressure variability rather than storage variability. It should also be noted that the  
567 MBR estimate based on GNSS/GRACE combination from Argus et al. (2022) was derived as the  
568 difference between gravity and elastic loading-based annual GWS estimates to the output of a  
569 hydrological model not including MSR. The authors interpret this difference solely as MBR and  
570 neglect the contribution of MFR in the estimate, owing that the method they apply cannot  
571 discriminate between the two MSR processes. To reliably quantify MBR at the scale of the CV  
572 and discriminate it from MFR, we suggest the implementation of a fully fluid-solid media  
573 coupled 3D groundwater model for the CV that integrates the wealth of hydrologic and remote  
574 sensing observations sensitive to dynamics in the aquifers as demonstrated in this study. The  
575 results should also be crosschecked with observations of groundwater ages, e.g. based on isotope  
576 studies (Earman et al., 2006).

577 Our findings are subject to uncertainties, albeit statistical tests of significance help  
578 corroborate the main results. The wavelet time-frequency analysis is affected by data gaps and  
579 variable sampling rates, similar to other spectral methods (Goswami & Chan, 1999), although the  
580 ability of the continuous wavelet transforms to localize signal components in time and space  
581 minimizes error propagation. GNSS sites may be affected by other processes causing annual  
582 oscillations, such as non-tidal loading, tectonic processes, thermoelastic deformation, and  
583 draconitic errors (Chanard et al., 2020). Errors in the GWS component from GRACE  
584 observations are subject to any error in the correction terms, which directly maps into the GWS  
585 time series. However, the three months delay between the peak of GWS and GWL remains

586 robust against the uncertainty in the timing of GWS (see Section 4.2). Hence, the measure that  
587 pressure propagates faster to deep aquifer layers than the groundwater volume change in the  
588 entire aquifer remains unaffected.

589         Recent studies (Ajami et al., 2011; Markovich et al., 2019; Meixner et al., 2016; Somers  
590 & McKenzie, 2020; Wahi et al., 2008; Welch & Allen, 2014) have recognized mountains'  
591 critical role in freshwater supply to lowland dry basins, debunking the outdated notion that  
592 mountain groundwater storage and supply is negligible. In the Sierra Nevada aquifers,  
593 cosmogenic isotope studies linking snowmelt and annual aquifer recharge indicate a strong link  
594 between snowmelt and aquifer recharge and discharge in the mountains (Urióstegui et al., 2017).  
595 Additional evidence is provided by the increased age of groundwater contributing to the spring  
596 stream flow over the Sierra Nevada, consistent with increased temperature and reduced  
597 precipitation at high elevations (Manning et al., 2012). Thus, the high Sierra Nevada snowpack is  
598 essential for recharging mountain aquifers, which, in turn, contributes to the long-term recharge  
599 of deep, confined CV aquifers. Sierra Nevada runoff and MFR's role in freshwater supply in the  
600 CV is well-understood (Faunt, 2009; Meixner et al., 2016). However, the mountain block  
601 recharge process proposed here to replenish deep aquifers is not considered in the current  
602 hydrological models for the Valley, for example, by Faunt et al. (2009). Annual, interannual, and  
603 long-term changes in snowpack directly impact the MFR and MBR from the Sierra Nevada  
604 Mountains to the CV. Thus, the reliance on hydroclimate models that currently do not account  
605 for MBR limits the ability to accurately forecast the risk of climate extremes to California's  
606 groundwater supply and presents challenges for developing appropriate adaptation and resiliency  
607 strategies. The observation and analysis presented here have implications for the CV's recharge  
608 mechanism to deep aquifers. We call for new models that more comprehensively account for the  
609 Sierra Nevada Mountains' role in California's water cycle, which may also require a revision of  
610 current management and resiliency plans. Finally, we suggest the integration of pressure physics  
611 into methods quantifying seasonal storage changes in CV aquifers that apply well data and  
612 storage coefficients, or deformation data, given that well level and deformation changes at  
613 seasonal time scales are also driven by a change in pressure, not only in storage.

614

## 615 **Acknowledgments**

616         We thank anonymous reviewers and the editor for constructive comments and  
617 suggestions. This research was partly funded by the National Aeronautics and Space  
618 Administration grants NNX17AD98G (SW, MS, GC), 80NSSC21K0419 (SW, MS, GC) and  
619 80NSSC21K0061 (SW), as well as the Department of Energy grant DE-SC0019307 (MS).  
620

## 621 **Open Research**

622         All data used for this study are publicly available from the following sources. GRACE data were  
623 accessed from JPL PO.DAAC at [https://podaac.jpl.nasa.gov/dataset/TELLUS\\_GRAC-GRFO\\_MASCON\\_CRI\\_GRID\\_RL06\\_V2](https://podaac.jpl.nasa.gov/dataset/TELLUS_GRAC-GRFO_MASCON_CRI_GRID_RL06_V2). SNODAS data were downloaded from the National  
624 Snow & Ice Data Center (<https://nsidc.org/data/g02158>), GLDAS Noah, CLSM and VIC model  
625 outputs from the Goddard Earth Sciences Data and Information Services Center via  
626 [https://disc.gsfc.nasa.gov/datasets/GLDAS\\_NOAH025\\_M\\_2.1/summary?keywords=GLDAS](https://disc.gsfc.nasa.gov/datasets/GLDAS_NOAH025_M_2.1/summary?keywords=GLDAS),

628 [https://disc.gsfc.nasa.gov/datasets/GLDAS\\_CLSM10\\_M\\_2.1/summary?keywords=GLDAS](https://disc.gsfc.nasa.gov/datasets/GLDAS_CLSM10_M_2.1/summary?keywords=GLDAS), and  
 629 [https://disc.gsfc.nasa.gov/datasets/GLDAS\\_VIC10\\_M\\_2.1/summary?keywords=GLDAS](https://disc.gsfc.nasa.gov/datasets/GLDAS_VIC10_M_2.1/summary?keywords=GLDAS),  
 630 respectively. We kindly thank Hannes Müller Schmied (hannes.mueller.schmied@em.uni-  
 631 frankfurt.de) at the University of Frankfurt for providing WGHM version 2.2d outputs. GNSS  
 632 time series were downloaded from the Nevada Geodetic Laboratory  
 633 ([http://geodesy.unr.edu/gps\\_timeseries/tenv3/IGS14/](http://geodesy.unr.edu/gps_timeseries/tenv3/IGS14/)). The California Department of Water  
 634 Resources provided reservoir data ([https://cdec.water.ca.gov/dynamicapp/getAll?sens\\_num=15](https://cdec.water.ca.gov/dynamicapp/getAll?sens_num=15))  
 635 and groundwater level data, which we retrieved as bulk download from the California Natural  
 636 Resources Agency via the California Open Data Portal for “Periodic Groundwater Level  
 637 Measurements” (<https://data.ca.gov/dataset/periodic-groundwater-level-measurements>) and for  
 638 “Continuous Groundwater Level Measurements” ([https://data.ca.gov/dataset/continuous-](https://data.ca.gov/dataset/continuous-groundwater-level-measurements)  
 639 [groundwater-level-measurements](https://data.ca.gov/dataset/continuous-groundwater-level-measurements)). Further groundwater level data were retrieved from the  
 640 USGS archives for “Daily Data” ([https://waterdata.usgs.gov/ca/nwis/dv/?referred\\_module=gw](https://waterdata.usgs.gov/ca/nwis/dv/?referred_module=gw))  
 641 and “Field Measurements” (<https://nwis.waterdata.usgs.gov/ca/nwis/gwlevels>). Wavelet software  
 642 packages are provided by C. Torrence and G. Compo at URL:  
 643 <http://atoc.colorado.edu/research/wavelets>, as well as by Jon Erickson at URL:  
 644 [https://www.mathworks.com/matlabcentral/fileexchange/20821-continuous-wavelet-transform-](https://www.mathworks.com/matlabcentral/fileexchange/20821-continuous-wavelet-transform-and-inverse)  
 645 [and-inverse](https://www.mathworks.com/matlabcentral/fileexchange/20821-continuous-wavelet-transform-and-inverse). InSAR results, assembled groundwater records as well as all data analysis results  
 646 presented in the supporting information or figures will be made available upon acceptance  
 647 through a repository with the Virginia Tech Data Repository (<https://data.lib.vt.edu/>). During  
 648 peer review, all data analysis results are available in the supporting information, and/or figures.  
 649  
 650

## 651 References

- 652 Adusumilli, S., Borsa, A. A., Fish, M. A., McMillan, H. K., & Silverii, F. (2019). A decade of terrestrial water  
 653 storage changes across the contiguous United States from GPS and GRACE. *Geophysical Research Letters*,  
 654 2019GL085370. <https://doi.org/10.1029/2019GL085370>
- 655 Ajami, H., Troch, P. A., Maddock, T., Meixner, T., & Eastoe, C. (2011). Quantifying mountain block recharge by  
 656 means of catchment-scale storage-discharge relationships. *Water Resources Research*, 47(4).  
 657 <https://doi.org/10.1029/2010WR009598>
- 658 Alam, S., Gebremichael, M., Ban, Z., Scanlon, B. R., Senay, G., & Lettenmaier, D. P. (2021). Post-Drought  
 659 Groundwater Storage Recovery in California’s Central Valley. *Water Resources Research*, 57(10).  
 660 <https://doi.org/10.1029/2021WR030352>
- 661 Alley, W. M. (2002). Flow and Storage in Groundwater Systems. *Science*, 296(5575), 1985–1990.  
 662 <https://doi.org/10.1126/science.1067123>
- 663 Argus, D. F., Landerer, F. W., Wiese, D. N., Martens, H. R., Fu, Y., Famiglietti, J. S., Thomas, B. F., Farr, T. G.,  
 664 Moore, A. W., & Watkins, M. M. (2017). Sustained water loss in California’s mountain ranges during severe  
 665 drought from 2012 to 2015 inferred from GPS. *Journal of Geophysical Research: Solid Earth*, 122(12),  
 666 10,510–559,585. <https://doi.org/10.1002/2017JB014424>
- 667 Argus, D. F., Martens, H. R., Borsa, A. A., Knappe, E., Wiese, D. N., Alam, S., Anderson, M., Khatiwada, A., Lau,  
 668 N., Peidou, A., Swarr, M., White, A., Bos, M. S., Landerer, F. W., & Gardner, P. (2022). Subsurface water  
 669 flux in California’s Central Valley and its source watershed from space geodesy. *Geophysical Research*  
 670 *Letters*. <https://doi.org/10.1029/2022GL099583>
- 671 Ayres, A., Hanak, E., Gray, B., Sencan, G., Bruno, E., Bou, A. E., & Collins, J. (2021). *Improving California’s*  
 672 *Water Market*.
- 673 Bales, R. C., Hopmans, J. W., O’Geen, A. T., Meadows, M., Hartsough, P. C., Kirchner, P., Hunsaker, C. T., &  
 674 Beaudette, D. (2011). Soil Moisture Response to Snowmelt and Rainfall in a Sierra Nevada Mixed-Conifer  
 675 Forest. *Vadose Zone Journal*, 10(3), 786–799. <https://doi.org/10.2136/vzj2011.0001>

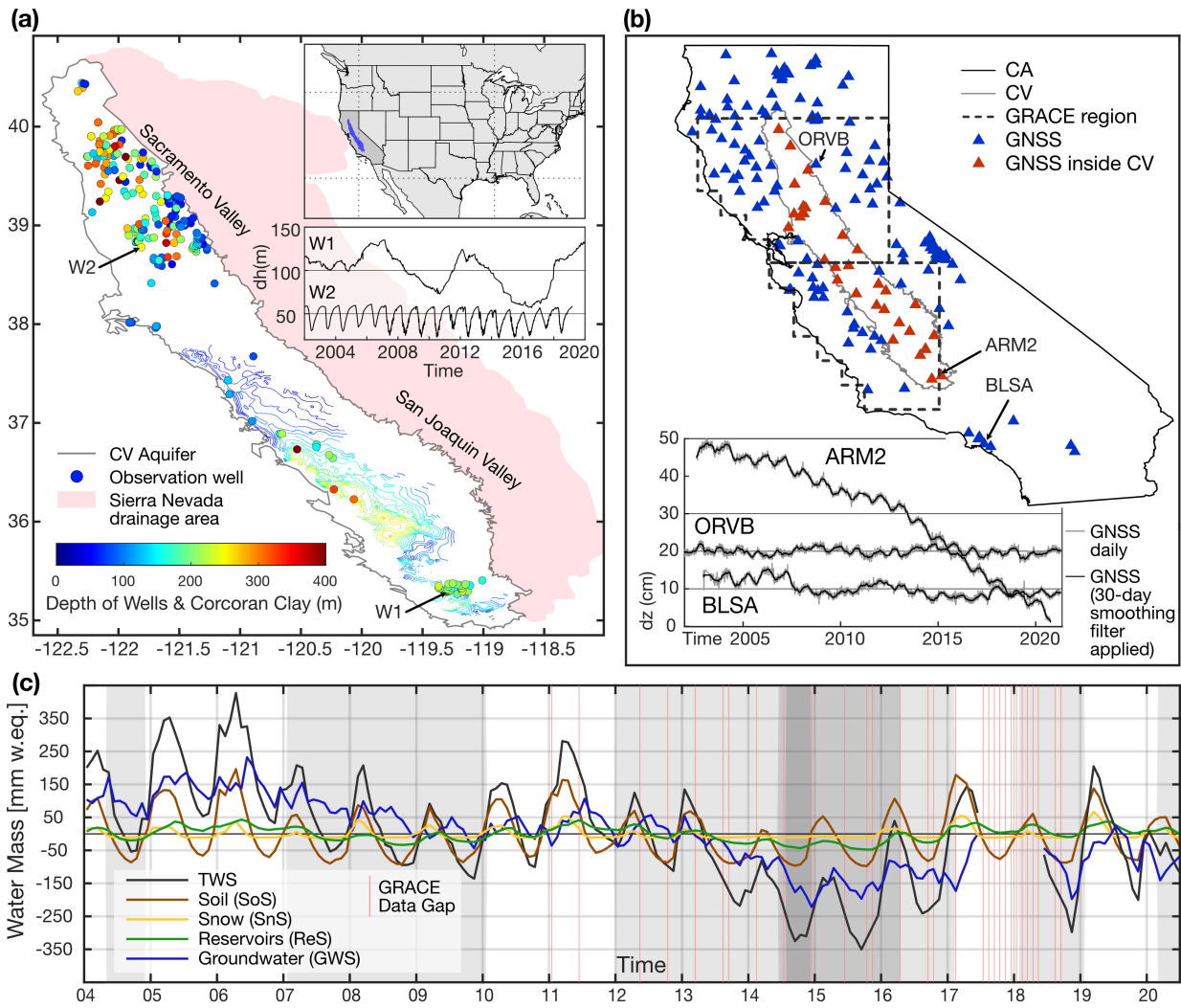
- 676 Beaudoin, H., & Rodell, M. (2016). GLDAS Noah Land Surface Model L4 monthly 0.25 x 0.25 degree V2.1,  
 677 NASA/GSFC/HSL: Greenbelt, Maryland, USA,. *Goddard Earth Sciences Data and Information Services*  
 678 *Center (GES DISC)*. <https://doi.org/10.5067/SXAVCZFAQLNO>
- 679 Berghuijs, W. R., Luijendijk, E., Moeck, C., van der Velde, Y., & Allen, S. T. (2022). Global Recharge Data Set  
 680 Indicates Strengthened Groundwater Connection to Surface Fluxes. *Geophysical Research Letters*, *49*(23).  
 681 <https://doi.org/10.1029/2022GL099010>
- 682 Borsa, A. A., Agnew, D. C., & Cayan, D. R. (2014). Ongoing drought-induced uplift in the western United States.  
 683 *Science*, *345*(6204), 1587–1590. <https://doi.org/10.1126/science.1260279>
- 684 Burow, K. R., Dubrovsky, N. M., & Shelton, J. L. (2007). Temporal trends in concentrations of DBCP and nitrate in  
 685 groundwater in the eastern San Joaquin Valley, California, USA. *Hydrogeology Journal*, *15*(5), 991–1007.  
 686 <https://doi.org/10.1007/s10040-006-0148-7>
- 687 Carlson, G., Shirzaei, M., Ojha, C., & Werth, S. (2020). Subsidence-Derived Volumetric Strain Models for Mapping  
 688 Extensional Fissures and Constraining Rock Mechanical Properties in the San Joaquin Valley, California.  
 689 *Journal of Geophysical Research: Solid Earth*. <https://doi.org/10.1029/2020JB019980>
- 690 Carlson, G., Shirzaei, M., Werth, S., Zhai, G., & Ojha, C. (2020). Seasonal and Long-Term Groundwater Unloading  
 691 in the Central Valley Modifies Crustal Stress. *Journal of Geophysical Research: Solid Earth*, *125*(1), 1–17.  
 692 <https://doi.org/10.1029/2019JB018490>
- 693 Carlson, G., Werth, S., & Shirzaei, M. (2022). Joint Inversion of GNSS and GRACE for Terrestrial Water Storage  
 694 Change in California. *Journal of Geophysical Research: Solid Earth*, *127*(3).  
 695 <https://doi.org/10.1029/2021JB023135>
- 696 CDWR. (2017). *California Department of Water Resources, California Data Exchange Center, Active Monthly*  
 697 *Reservoirs*. [http://cdec.water.ca.gov/misc/monthly\\_res.html](http://cdec.water.ca.gov/misc/monthly_res.html)
- 698 CDWR. (2019). *Continuous Groundwater Level Measurements*. <http://wdl.water.ca.gov/waterdatalibrary/>
- 699 Chanard, K., Métois, M., Rebischung, P., & Avouac, J. P. (2020). A warning against over-interpretation of seasonal  
 700 signals measured by the Global Navigation Satellite System. *Nature Communications*, *11*(1), 1–4.  
 701 <https://doi.org/10.1038/s41467-020-15100-7>
- 702 Costantini, M. (1998). A novel phase unwrapping method based on network programming. *IEEE Transactions on*  
 703 *Geoscience and Remote Sensing*, *36*(3), 813–821. <https://doi.org/10.1109/36.673674>
- 704 Earman, S., Campbell, A. R., Phillips, F. M., & Newman, B. D. (2006). Isotopic exchange between snow and  
 705 atmospheric water vapor: Estimation of the snowmelt component of groundwater recharge in the southwestern  
 706 United States. *Journal of Geophysical Research Atmospheres*, *111*(9). <https://doi.org/10.1029/2005JD006470>
- 707 Erickson, J. (2019). *Continuous wavelet transform and inverse* (Retrieved August 30, 2019.). MATLAB Central File  
 708 Exchange.
- 709 Escriva-Bou, A., Hui, R., Maples, S., Medellín-Azuara, J., Harter, T., & Lund, J. R. (2020). Planning for  
 710 groundwater sustainability accounting for uncertainty and costs: An application to California's Central Valley.  
 711 *Journal of Environmental Management*, *264*, 110426.
- 712 Escriva-Bou, A., Sencan, G., & Hanak, E. (2021). *Groundwater Recharge, Fact Sheet August 2021*.
- 713 Famiglietti, J. S., Lo, M., Ho, S. L., Bethune, J., Anderson, K. J., Syed, T. H., Swenson, S. C., de Linage, C. R., &  
 714 Rodell, M. (2011). Satellites measure recent rates of groundwater depletion in California's Central Valley.  
 715 *Geophysical Research Letters*, *38*(3). <https://doi.org/10.1029/2010GL046442>
- 716 Farr, T. G., Rosen, P. A., Caro, E., Crippen, R., Duren, R., Hensley, S., Kobrick, M., Paller, M., Rodriguez, E.,  
 717 Roth, L., Seal, D., Shaffer, S., Shimada, J., Umland, J., Werner, M., Oskin, M., Burbank, D., & Alsdorf, D.  
 718 (2007). The Shuttle Radar Topography Mission. *Reviews of Geophysics*, *45*(2), RG2004.  
 719 <https://doi.org/10.1029/2005RG000183>
- 720 Faunt, C. C. (2009). *Groundwater Availability of the Central Valley Aquifer, California* (C. C. Faunt, Ed.). U.S.  
 721 Geological Survey Professional Paper 1766. <https://pubs.usgs.gov/pp/1766/>
- 722 Faunt, C. C., Sneed, M., Traum, J., & Brandt, J. T. (2016). Water availability and land subsidence in the Central  
 723 Valley, California, USA. *Hydrogeology Journal*, *24*(3), 675–684. <https://doi.org/10.1007/s10040-015-1339-x>
- 724 Feth, J. H. (1964). Hidden Recharge. *Groundwater*, *2*(4), 14–17. [https://doi.org/10.1111/j.1745-](https://doi.org/10.1111/j.1745-6584.1964.tb01780.x)  
 725 [6584.1964.tb01780.x](https://doi.org/10.1111/j.1745-6584.1964.tb01780.x)
- 726 Fetter, C. W., & Kremer, D. (2022). *Applied Hydrogeology* (5th ed.). Waveland Press.
- 727 Fox-Kemper, B., Hewitt, H. T., Xiao, C., Aðalgeirsdóttir, G., Drijfhout, S. S., Edwards, T. L., Golledge, N. R.,  
 728 Hemer, M., Kopp, R. E., Krinner, G., Mix, A., Notz, D., Nowicki, S., Nurhati, I. S., Ruiz, L., Sallée, J.-B.,  
 729 Slangen, A. B. A., & Yu, Y. (2021). Ocean, Cryosphere and Sea Level Change. In *Climate Change 2021: The*  
 730 *Physical Science Basis. Contribution of Working Group I to the Sixth Assessment Report of the*  
 731 *Intergovernmental Panel on Climate Change [MassonDelmotte, V., P. Zhai, A. Pirani, S. L. Connors, C.*

- 732 Péan, S. Berger, N. Caud, Y. Chen., Cambridge University Press, Cambridge, United Kingdom and New  
 733 York, NY, USA, 2391 pp. doi:10.1017/9781009157896.  
 734 [https://report.ipcc.ch/ar6/wg1/IPCC\\_AR6\\_WGI\\_FullReport.pdf](https://report.ipcc.ch/ar6/wg1/IPCC_AR6_WGI_FullReport.pdf).
- 735 Franceschetti, G., & Lanari, R. (1999). *Synthetic aperture radar processing*. CRC Press.
- 736 Galloway, D. L., Jones, D. R., & Ingebritsen, S. E. (1999). *Land subsidence in the United States*. U.S. Geological  
 737 Survey Circular 1182. <https://doi.org/10.3133/cir1182>
- 738 Gao, S. S., Silver, P. G., Linde, A. T., & Sacks, I. S. (2000). Annual modulation of triggered seismicity following  
 739 the 1992 Landers earthquake in California. *Nature*, 406(6795), 500–504. <https://doi.org/10.1038/35020045>
- 740 Ghasemzade, M., Asante, K. O., Petersen, C., Kocis, T., Dahlke, H. E., & Harter, T. (2019). An Integrated  
 741 Approach Toward Sustainability via Groundwater Banking in the Southern Central Valley, California. *Water*  
 742 *Resources Research*, 55(4), 2742–2759. <https://doi.org/10.1029/2018WR024069>
- 743 Gilbert, J. M., & Maxwell, R. M. (2017). Examining regional groundwater-surface water dynamics using an  
 744 integrated hydrologic model of the San Joaquin River basin. *Hydrology and Earth System Sciences*, 21(2),  
 745 923–947. <https://doi.org/10.5194/hess-21-923-2017>
- 746 Goswami, J. C., & Chan, A. K. (1999). *Fundamentals of Wavelets: Theory, Algorithms, and Applications*. Wiley-  
 747 Interscience.
- 748 Hanak, E., Lund, J., Arnold, B., Escriva-Bou, A., Gray, B., Green, S., Harter, T., Howitt, R., MacEwan, D., &  
 749 Medellín-Azuara, J. (2017). *Water Stress and a Changing San Joaquin Valley*. Public Policy Institute of  
 750 California.
- 751 Hanson, R. T., Flint, L. E., Flint, A. L., Dettinger, M. D., Faunt, C. C., Cayan, D., & Schmid, W. (2012). A method  
 752 for physically based model analysis of conjunctive use in response to potential climate changes. *Water*  
 753 *Resources Research*, 48(2). <https://doi.org/10.1029/2011WR010774>
- 754 Harpold, A., Dettinger, M., & Rajagopal, S. (2017). Defining Snow Drought and Why It Matters. *Eos*.  
 755 <https://doi.org/10.1029/2017EO068775>
- 756 Hatchett, B. J., & McEvoy, D. J. (2018). Exploring the origins of snow drought in the northern sierra nevada,  
 757 california. *Earth Interactions*, 22(2), 1–13. <https://doi.org/10.1175/EI-D-17-0027.1>
- 758 Healy, R. W., & Scanlon, B. R. (2010). *Estimating Groundwater Recharge*. Cambridge University Press.
- 759 Huth, A. K., Leydecker, A., Sickman, J. O., & Bales, R. C. (2004). A two-component hydrograph separation for  
 760 three high-elevation catchments in the Sierra Nevada, California. *Hydrological Processes*, 18(9), 1721–1733.  
 761 <https://doi.org/10.1002/hyp.1414>
- 762 Jódar, J., Cabrera, J. A., Martos-Rosillo, S., Ruiz-Constán, A., González-Ramón, A., Lambán, L. J., Herrera, C., &  
 763 Custodio, E. (2017). Groundwater discharge in high-mountain watersheds: A valuable resource for  
 764 downstream semi-arid zones. The case of the Bérchules River in Sierra Nevada (Southern Spain). *Science of*  
 765 *The Total Environment*, 593–594, 760–772. <https://doi.org/10.1016/j.scitotenv.2017.03.190>
- 766 Johnson, C. W., Fu, Y., & Bürgmann, R. (2017). Seasonal water storage, stress modulation, and California  
 767 seismicity. *Science*, 356(6343), 1161–1164. <https://doi.org/10.1126/science.aak9547>
- 768 Konikow, L. F. (2015). Long-Term Groundwater Depletion in the United States. *Groundwater*, 53(1), 2–9.  
 769 <https://doi.org/10.1111/gwat.12306>
- 770 Lee, J. C., & Shirzaei, M. (2023). Novel algorithms for pair and pixel selection and atmospheric error correction in  
 771 multitemporal InSAR. *Remote Sensing of Environment*, 286. <https://doi.org/10.1016/j.rse.2022.113447>
- 772 Li, R., Ou, G., Pun, M., & Larson, L. (2018). Evaluation of Groundwater Resources in Response to Agricultural  
 773 Management Scenarios in the Central Valley, California. *Journal of Water Resources Planning and*  
 774 *Management*, 144(12), 04018078. [https://doi.org/10.1061/\(asce\)wr.1943-5452.0001014](https://doi.org/10.1061/(asce)wr.1943-5452.0001014)
- 775 Liu, F., Conklin, M. H., & Shaw, G. D. (2017). Insights into hydrologic and hydrochemical processes based on  
 776 concentration-discharge and end-member mixing analyses in the mid-Merced River Basin, Sierra Nevada,  
 777 California. *Water Resources Research*, 53(1), 832–850. <https://doi.org/10.1002/2016WR019437>
- 778 Manning, A. H., Clark, J. F., Diaz, S. H., Rademacher, L. K., Earman, S., & Niel Plummer, L. (2012). Evolution of  
 779 groundwater age in a mountain watershed over a period of thirteen years. *Journal of Hydrology*, 460–461, 13–  
 780 28. <https://doi.org/10.1016/j.jhydrol.2012.06.030>
- 781 Markovich, K. H., Manning, A. H., Condon, L. E., & McIntosh, J. C. (2019). Mountain-Block Recharge: A Review  
 782 of Current Understanding. *Water Resources Research*, 55(11), 8278–8304.  
 783 <https://doi.org/10.1029/2019WR025676>
- 784 Massoud, E. C., Purdy, A. J., Miro, M. E., & Famiglietti, J. S. (2018). Projecting groundwater storage changes in  
 785 California's Central Valley. *Scientific Reports*, 8(1), 12917. <https://doi.org/10.1038/s41598-018-31210-1>

- 786 McCabe, G. J., Palecki, M. A., & Betancourt, J. L. (2004). Pacific and Atlantic Ocean influences on multidecadal  
787 drought frequency in the United States. *Proceedings of the National Academy of Sciences*, *101*(12), 4136–  
788 4141. <https://doi.org/10.1073/pnas.0306738101>
- 789 McMahon, P. B., Plummer, L. N., Böhlke, J. K., Shapiro, S. D., & Hinkle, S. R. (2011). A comparison of recharge  
790 rates in aquifers of the United States based on groundwater-age data. *Hydrogeology Journal*, *19*(4), 779–800.  
791 <https://doi.org/10.1007/s10040-011-0722-5>
- 792 Meixner, T., Manning, A. H., Stonestrom, D. A., Allen, D. M., Ajami, H., Blasch, K. W., Brookfield, A. E., Castro,  
793 C. L., Clark, J. F., & Gochis, D. J. (2016). Implications of projected climate change for groundwater recharge  
794 in the western United States. *Journal of Hydrology*, *534*, 124–138.
- 795 Meyer, P. L. (1970). *Introductory Probability and Statistical Applications* (2nd ed.). Oxford & IBH Publishing Co.
- 796 Montgomery-Brown, E. K., Shelly, D. R., & Hsieh, P. A. (2019). Snowmelt-Triggered Earthquake Swarms at the  
797 Margin of Long Valley Caldera, California. *Geophysical Research Letters*, *46*(7), 3698–3705.  
798 <https://doi.org/10.1029/2019GL082254>
- 799 Mote, P. W., Li, S., Lettenmaier, D. P., Xiao, M., & Engel, R. (2018). Dramatic declines in snowpack in the western  
800 US. *Npj Climate and Atmospheric Science*, *1*(1). <https://doi.org/10.1038/s41612-018-0012-1>
- 801 Murray, K. D., & Lohman, R. B. (2018). Short-lived pause in Central California subsidence after heavy winter  
802 precipitation of 2017. *Science Advances*, *4*(8), eaar8144. <https://doi.org/10.1126/sciadv.aar8144>
- 803 Neely, W. R., Borsa, A. A., Burney, J. A., Levy, M. C., Silverii, F., & Sneed, M. (2021). Characterization of  
804 Groundwater Recharge and Flow in California's San Joaquin Valley From InSAR-Observed Surface  
805 Deformation. *Water Resources Research*, *57*(4), 1–20. <https://doi.org/10.1029/2020wr028451>
- 806 NOHRSC. (2004). *National Operational Hydrologic Remote Sensing Center, Snow Data Assimilation System*  
807 *(SNODAS) data products at NSIDC, Version 1*. National Snow and Ice Data Center, Boulder, CO, USA.  
808 <https://doi.org/10.7265/N5TB14TC>
- 809 Ojha, C., Shirzaei, M., Werth, S., Argus, D. F., & Farr, T. G. (2018). Sustained Groundwater Loss in California's  
810 Central Valley Exacerbated by Intense Drought Periods. *Water Resources Research*, *54*(7), 4449–4460.  
811 <https://doi.org/10.1029/2017WR022250>
- 812 Ojha, C., Werth, S., & Shirzaei, M. (2019). Groundwater Loss and Aquifer System Compaction in San Joaquin  
813 Valley During 2012–2015 Drought. *Journal of Geophysical Research: Solid Earth*, *124*(3), 3127–3143.  
814 <https://doi.org/10.1029/2018JB016083>
- 815 Pepin, N., Bradley, R. S., Diaz, H. F., Baraer, M., Caceres, E. B., Forsythe, N., Fowler, H., Greenwood, G., Hashmi,  
816 M. Z., Liu, X. D., Miller, J. R., Ning, L., Ohmura, A., Palazzi, E., Rangwala, I., Schöner, W., Severskiy, I.,  
817 Shahgedanova, M., Wang, M. B., ... Yang, D. Q. (2015). Elevation-dependent warming in mountain regions  
818 of the world. *Nature Climate Change*, *5*(5), 424–430. <https://doi.org/10.1038/nclimate2563>
- 819 Peterson, D., Smith, R., Stewart, I., Knowles, N., Soulard, C., Hager, S., & Norton, G. A. (2003). *Snowmelt*  
820 *Discharge Characteristics, Sierra Nevada, California*. (Series Name SIR - 2005-5056). U.S. Geological  
821 Survey.
- 822 Quiring, S. M., & Goodrich, G. B. (2008). Nature and causes of the 2002 to 2004 drought in the southwestern  
823 United States compared with the historic 1953 to 1957 drought. *Climate Research*, *36*(1), 41–52.  
824 <https://doi.org/10.3354/cr00735>
- 825 Rodell, M., Houser, P. R., Jambor, U., Gottschalk, J., Mitchell, K., Meng, C.-J., Arsenault, K., Cosgrove, B.,  
826 Radakovich, J., Bosilovich, M., Entin\*, J. K., Walker, J. P., Lohmann, D., & Toll, D. (2004). The Global Land  
827 Data Assimilation System. *Bulletin of the American Meteorological Society*, *85*(3), 381–394.  
828 <https://doi.org/10.1175/BAMS-85-3-381>
- 829 Saar, M. O., & Manga, M. (2003). Seismicity induced by seasonal groundwater recharge at Mt. Hood, Oregon.  
830 *Earth and Planetary Science Letters*, *214*(3–4), 605–618. [https://doi.org/10.1016/S0012-821X\(03\)00418-7](https://doi.org/10.1016/S0012-821X(03)00418-7)
- 831 Scanlon, B. R., Longuevergne, L., & Long, D. (2012). Ground referencing GRACE satellite estimates of  
832 groundwater storage changes in the California Central Valley, USA. *Water Resources Research*, *48*(4),  
833 W04520. <https://doi.org/10.1029/2011WR011312>
- 834 Schmidt, R., Flechtner, F., Meyer, U., Neumayer, K.-H., Dahle, C., König, R., & Kusche, J. (2008). Hydrological  
835 Signals Observed by the GRACE Satellites. *Surveys in Geophysics*, *29*(4–5), 319–334.  
836 <https://doi.org/10.1007/s10712-008-9033-3>
- 837 Schreiner-McGraw, A. P., & Ajami, H. (2022). Combined impacts of uncertainty in precipitation and air  
838 temperature on simulated mountain system recharge from an integrated hydrologic model. *Hydrology and*  
839 *Earth System Sciences*, *26*(4), 1145–1164. <https://doi.org/10.5194/hess-26-1145-2022>
- 840 Shirzaei, M. (2013). A Wavelet-Based Multitemporal DInSAR Algorithm for Monitoring Ground Surface Motion.  
841 *Ieee Geoscience and Remote Sensing Letters*, *10*(3), 456–460. <https://doi.org/10.1109/Lgrs.2012.2208935>

- 842 Shirzaei, M., Bürgmann, R., & Fielding, E. J. (2017). Applicability of Sentinel-1 Terrain Observation by Progressive  
843 Scans multitemporal interferometry for monitoring slow ground motions in the San Francisco Bay Area.  
844 *Geophysical Research Letters*, 44(6), 2733–2742. <https://doi.org/10.1002/2017GL072663>.
- 845 Shirzaei, M., Bürgmann, R., Foster, J., Walter, T. R., & Brooks, B. A. (2013). Aseismic deformation across the  
846 Hilina fault system, Hawaii, revealed by wavelet analysis of InSAR and GPS time series. *Earth and Planetary  
847 Science Letters*, 376, 12–19. <https://doi.org/10.1016/j.epsl.2013.06.011>
- 848 Shirzaei, M., Ojha, C., Werth, S., Carlson, G., & Vivoni, E. R. (2019). Comment on “Short-lived pause in Central  
849 California subsidence after heavy winter precipitation of 2017” by K. D. Murray and R. B. Lohman. *Science  
850 Advances*, 5(eaav8038). <https://doi.org/10.1126/sciadv.aav8038>
- 851 Siebert, S., Burke, J., Faures, J. M., Frenken, K., Hoogeveen, J., Döll, P., & Portmann, F. T. (2010). Groundwater  
852 use for irrigation - A global inventory. *Hydrology and Earth System Sciences*, 14(10), 1863–1880.  
853 <https://doi.org/10.5194/hess-14-1863-2010>
- 854 Smith, R. G., Knight, R., Chen, J., Reeves, J. A., Zebker, H. A., Farr, T., & Liu, Z. (2017). Estimating the permanent  
855 loss of groundwater storage in the southern San Joaquin Valley, California. *Water Resources Research*, 53(3),  
856 2133–2148. <https://doi.org/10.1002/2016WR019861>
- 857 Somers, L. D., & McKenzie, J. M. (2020). A review of groundwater in high mountain environments. *Wiley  
858 Interdisciplinary Reviews: Water*, 7(6), 1–27. <https://doi.org/10.1002/wat2.1475>
- 859 Stevenson, S., Coats, S., Touma, D., Cole, J., Lehner, F., Fasullo, J., & Otto-Bliesner, B. (2022). Twenty-first  
860 century hydroclimate: A continually changing baseline, with more frequent extremes. *Proceedings of the  
861 National Academy of Sciences*, 119(12). <https://doi.org/10.1073/pnas.2108124119>
- 862 Tague, C., & Grant, G. E. (2009). Groundwater dynamics mediate low-flow response to global warming in snow-  
863 dominated alpine regions. *Water Resources Research*, 45(7). <https://doi.org/10.1029/2008WR007179>
- 864 Tague, C., Grant, G., Farrell, M., Choate, J., & Jefferson, A. (2008). Deep groundwater mediates streamflow  
865 response to climate warming in the Oregon Cascades. *Climatic Change*, 86(1–2), 189–210.  
866 <https://doi.org/10.1007/s10584-007-9294-8>
- 867 Talwani, P., & Acree, S. (1985). Pore pressure diffusion and the mechanism of reservoir-induced seismicity. In  
868 *Earthquake prediction* (pp. 947–965). Springer.
- 869 Tang, Q., & Oki, T. (Eds.). (2016). *Terrestrial Water Cycle and Climate Change*. John Wiley & Sons, Inc.  
870 <https://doi.org/10.1002/9781118971772>
- 871 Tapley, B. D., Bettadpur, S., Ries, J. C., Thompson, P. F., & Watkins, M. M. (2004). GRACE measurements of  
872 mass variability in the Earth system. *Science*, 305(5683), 503–505. <https://doi.org/10.1126/science.1099192>
- 873 Tapley, B. D., Watkins, M. M., Flechtner, F., Reigber, C., Bettadpur, S., Rodell, M., Sasgen, I., Famiglietti, J. S.,  
874 Landerer, F. W., Chambers, D. P., Reager, J. T., Gardner, A. S., Save, H., Ivins, E. R., Swenson, S. C.,  
875 Boening, C., Dahle, C., Wiese, D. N., Dobslaw, H., ... Velicogna, I. (2019). Contributions of GRACE to  
876 understanding climate change. *Nature Climate Change*, 9(5), 358–369. [https://doi.org/10.1038/s41558-019-  
0456-2](https://doi.org/10.1038/s41558-019-<br/>877 0456-2)
- 878 Torrence, C., & Compo, G. P. (1998). A practical guide to wavelet analysis. In *Bulletin of the American  
879 Meteorological Society* (Retrieved December 5, 2018.; Vol. 79, Issue 1, pp. 61–78).  
880 [https://doi.org/10.1175/1520-0477\(1998\)079<0061:APGTWA>2.0.CO;2](https://doi.org/10.1175/1520-0477(1998)079<0061:APGTWA>2.0.CO;2)
- 881 Urióstegui, S. H., Bibby, R. K., Esser, B. K., & Clark, J. F. (2017). Quantifying annual groundwater recharge and  
882 storage in the central Sierra Nevada using naturally occurring <sup>35</sup>S. *Hydrological Processes*, 31(6), 1382–  
883 1397. <https://doi.org/10.1002/hyp.11112>
- 884 USGS. (2021). *USGS Groundwater Data for the Nation*. <https://waterdata.usgs.gov/nwis/gw>
- 885 Vasco, D. W., Kim, K., Farr, T. G., Reager, J. T., Bekaert, D., Singh, S., & Beaudoin, H. K. (2022). Using  
886 Sentinel-1 and GRACE satellite data to monitor the long- and short-term hydrological variations within the  
887 Tulare Basin, California. *Scientific Reports*, 1–14. <https://doi.org/10.1038/s41598-022-07650-1>
- 888 Vrugt, J. A., Dekker, S. C., & Bouten, W. (2003). Identification of rainfall interception model parameters from  
889 measurements of throughfall and forest canopy storage. *Water Resources Research*, 39(9).  
890 <https://doi.org/10.1029/2003WR002013>
- 891 Wahi, A. K., Hogan, J. F., Ekwurzel, B., Baillie, M. N., & Eastoe, C. J. (2008). Geochemical Quantification of  
892 Semiarid Mountain Recharge. *Ground Water*, 46(3), 414–425. [https://doi.org/10.1111/j.1745-  
6584.2007.00413.x](https://doi.org/10.1111/j.1745-<br/>893 6584.2007.00413.x)
- 894 Wang, H. F. (2000). *Theory of Linear Poroelasticity with Applications to Geomechanics and Hydrogeology*.  
895 Princeton Univ. Press.

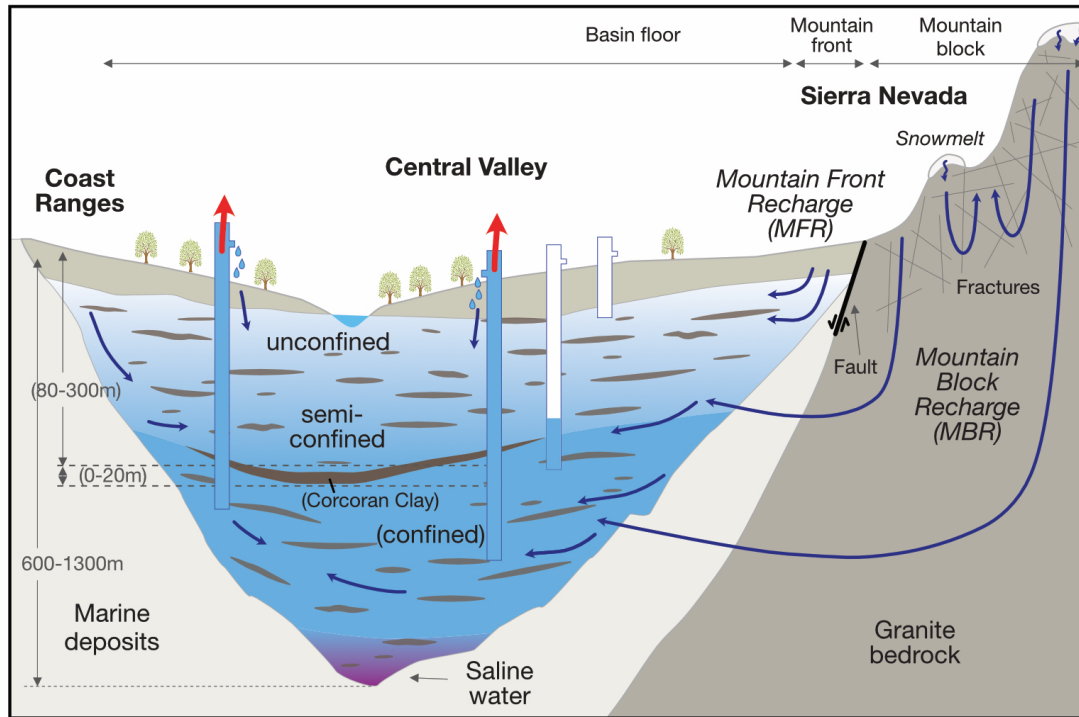
- 896 Welch, L. A., & Allen, D. M. (2014). Hydraulic conductivity characteristics in mountains and implications for  
897 conceptualizing bedrock groundwater flow. *Hydrogeology Journal*, 22(5), 1003–1026.  
898 <https://doi.org/10.1007/s10040-014-1121-5>
- 899 Werner, C., U. Wegmüller, T. Strozzi, & A. Wiesmann. (2000). Gamma SAR and interferometric processing  
900 software. *Proceedings of the Ers-Envisat Symposium, Gothenburg, Sweden.*
- 901 White, A. M., Gardner, W. P., Borsa, A. A., Argus, D. F., & Martens, H. R. (2022). A review of GNSS/GPS in  
902 hydrogeodesy: Hydrologic loading applications and their implications for water resource research. *Water*  
903 *Resources Research*. <https://doi.org/10.1029/2022WR032078>
- 904 Yin, D., & Roderick, M. L. (2020). Inter-annual variability of the global terrestrial water cycle. *Hydrology and*  
905 *Earth System Sciences*, 24(1), 381–396. <https://doi.org/10.5194/hess-24-381-2020>
- 906 Zektser, I. S., & Everett, L. G. (2004). *Groundwater Resources of the World and Their Use* (IHP-VI Series on  
907 Groundwater No. 6). United Nations Educational, Scientific and Cultural Organization (UNESCO).
- 908
- 909



910

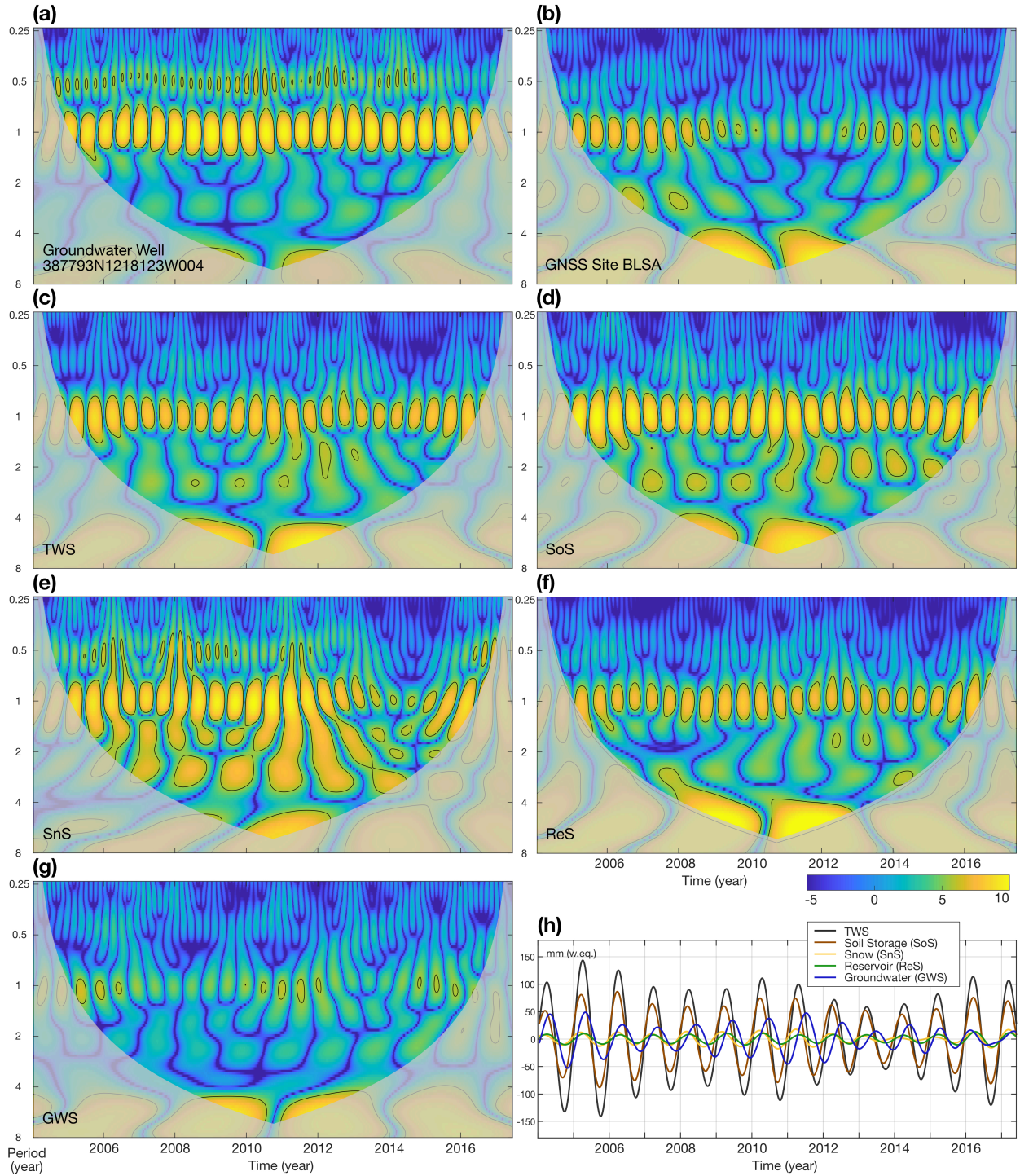
911 **Figure 1.** Overview of study area and data sets applied in this study. **(a)** Study area and  
 912 hydrogeological datasets: Outline of the Central Valley aquifer system (grey line,  $A_{CV} = 53,672$   
 913 km<sup>2</sup>), Sierra Nevada drainage area (red shade,  $A_{SN} = 63,780$  km<sup>2</sup>), location and depth of  
 914 observation wells that provide measurements at depth of 50 m and deeper, and lateral coverage  
 915 and depth of the confining Corcoran clay layer (source USGS:  
 916 [https://water.usgs.gov/GIS/metadata/usgswrd/XML/pp1766\\_corcoran\\_clay\\_depth\\_feet.xml](https://water.usgs.gov/GIS/metadata/usgswrd/XML/pp1766_corcoran_clay_depth_feet.xml)). See  
 917 Figure S4e and S4f for histograms of well depths. Top inset indicates location of the study area  
 918 over contiguous US. Bottom inset shows time series of two selected well sites W1  
 919 (#352958N1193011W001) and W2 (#387793N1218123W004). **(b)** Geodetic data sets: Mass  
 920 change regions of JPL GRACE mascon solutions (black dashed line) and location of GNSS sites  
 921 from the University of Reno, Nevada (red and blue triangles). Red triangles mark stations located  
 922 inside the Central Valley (CV), and blue triangles those outside the CV aquifer boundary. **(c)**  
 923 Time series of TWS from GRACE, composite hydrological storages and estimated GW storage  
 924 are averaged for the GRACE region shown in panel a, after Ojha et al. [2019]. Gray shaded  
 925 background areas (light, medium, dark gray) indicate that the USDM identifies >30% (>30%,  
 926 >60%) of California's area to be in moderate (exceptional, exceptional) dry condition (compare  
 927 Fig. S3).

928



929

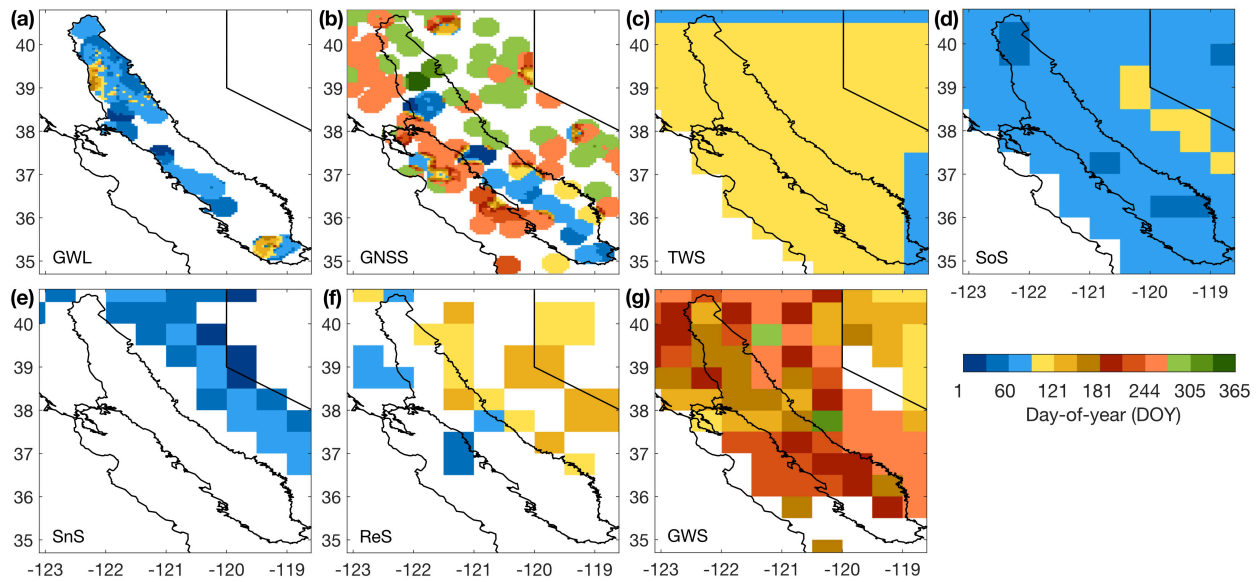
930 **Figure 2.** Conceptual and process-based model of pressure propagation and recharge in the  
 931 Sierra Nevada to deep aquifer layers of the Central Valley. **(a)** Hydrogeological setting in the  
 932 Central Valley (~400 m a.s.l.) and Sierra Nevada Mountains (up to ~4000 m a.s.l.). Indicated are  
 933 major groundwater fluxes in and out from deep aquifer layers, including mountain front and  
 934 mountain block recharge (MFR and MBR). Confining unit of the Corcoran clay is only present  
 935 in the southern San Joaquin Valley, where pumping is more intense compared to the northern  
 936 Sacramento Valley (Fig. 1a). This graph is inspired by Faunt et al. (2009) (Fig. A9 therein),  
 937 Smith et al. (2017) (Fig. 2 therein) as well as Somers and McKenzie (2020) (Fig. 5 therein).  
 938



939

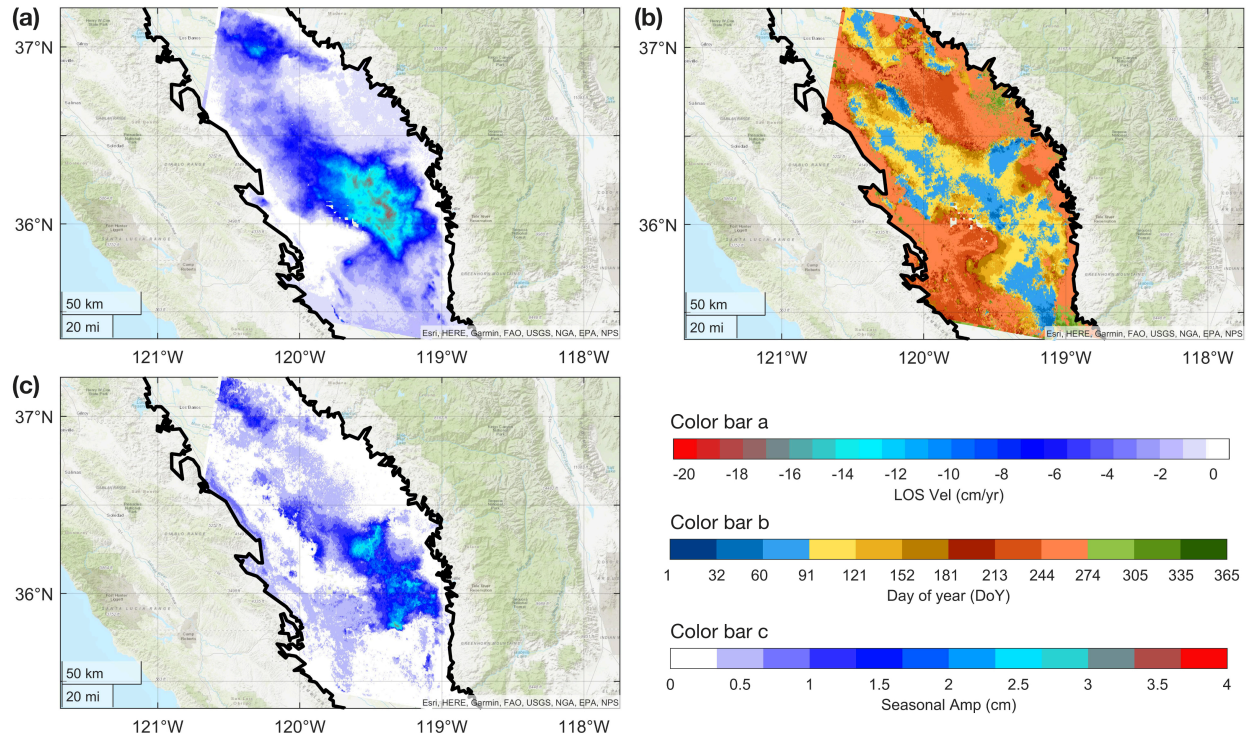
940 **Figure 3.** Wavelet time-frequency analysis. A wavelet analysis was performed for time series of  
 941 all available datasets to isolate the annual signal component. Wavelet spectrum of time series of  
 942 (a) groundwater level at well 387793N1218123W004 and (b) vertical land motion at GNSS site  
 943 BLSA (see Fig. 1 for their location), and of average water storage variations in the GRACE  
 944 region: (c) total water storage (TWS) from GRACE, (d) soil storage (SoS) from GLDAS and  
 945 WGFM, (e) snow storage (SnS) from SNODAS, (f) reservoir storage (ReS) from CDWR and (g)

946 groundwater storage (GWS) in CV. **(h)** Reconstructed annual signal component for periods  
 947 within range of 0.75-0.25 years from water storage wavelet spectra shown in panel c-g.



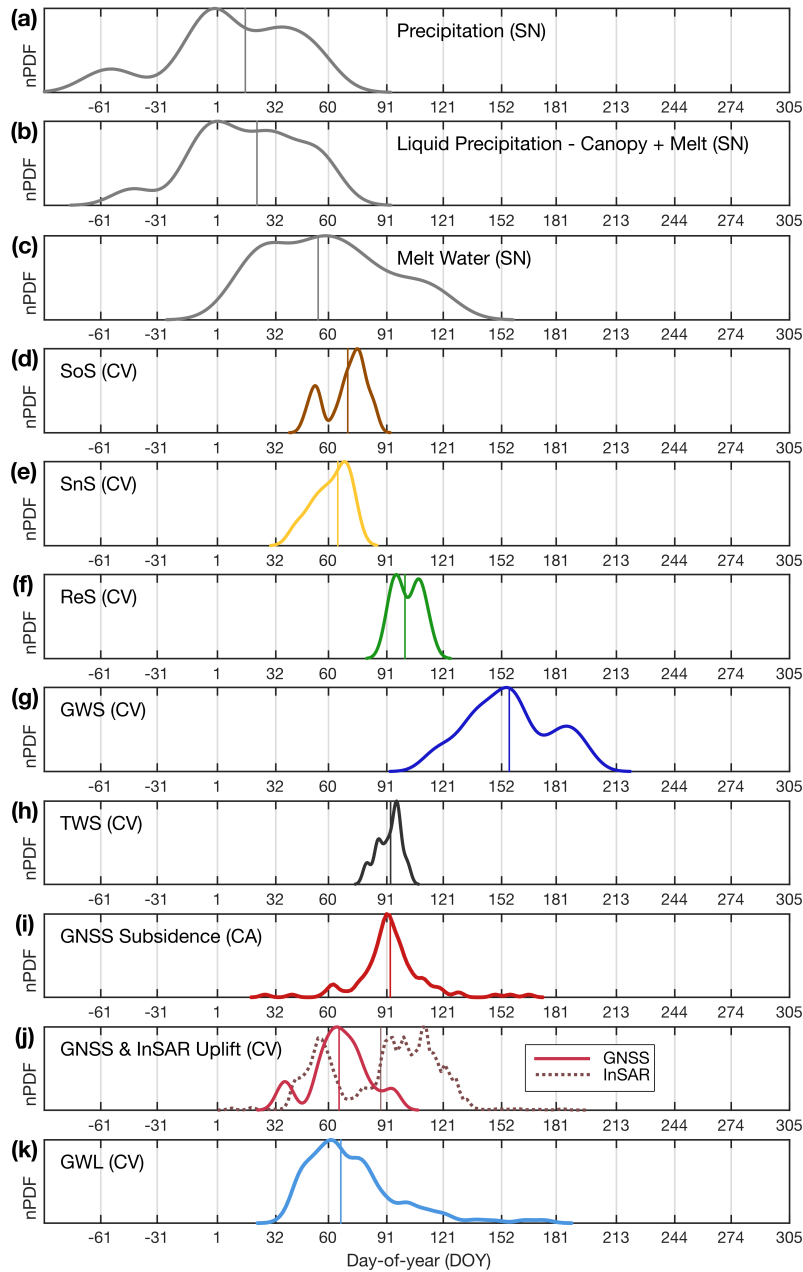
948

949 **Figure 4.** Timing of annual maximum of groundwater related signals. Timings are given in day-  
 950 of-year (DOY). (a) Groundwater levels (GWL) at 250 observation sites throughout the Central  
 951 Valley providing at least three years of data during 2002-2020 at depths below 50 m. (b) Vertical  
 952 land motion (maximum uplift) at 170 GNSS sites throughout entire California with a seasonal  
 953 amplitude larger than the median of the time series error standard deviation. Timing for  
 954 groundwater and GNSS were inversely interpolated using a 25 km correlation radius. Remaining  
 955 panels show timing of annual maximum water storage at 0.5-degree sampling resolution: (c) total  
 956 water storage (TWS) from GRACE, (d) soil storage (SoS) from GLDAS-Noah, (e) snow storage  
 957 (SnS) from SNODAS, (f) reservoir storage (ReS) from CDWR and (g) resulting groundwater  
 958 storage (GWS). White areas have either no data or amplitude of annual variation is near zero.  
 959 Annual oscillations of vertical land motion inside the CV are temporally aligned with those of  
 960 groundwater level variations. In contrast, oscillations of vertical land motion outside the Central  
 961 Valley are in resonance with annual oscillations of total water storage changes detected by  
 962 GRACE (compare panel b with c, and Fig. 6), because maximum VLM outside the Valley is  
 963 driven by minimum elastic load of the water masses. Individual values for groundwater well and  
 964 GNSS sites, timing of minima, related histograms, and standard deviations of annual timing  
 965 during observation periods are shown in Figures S8, S9, S10, and S11.



966

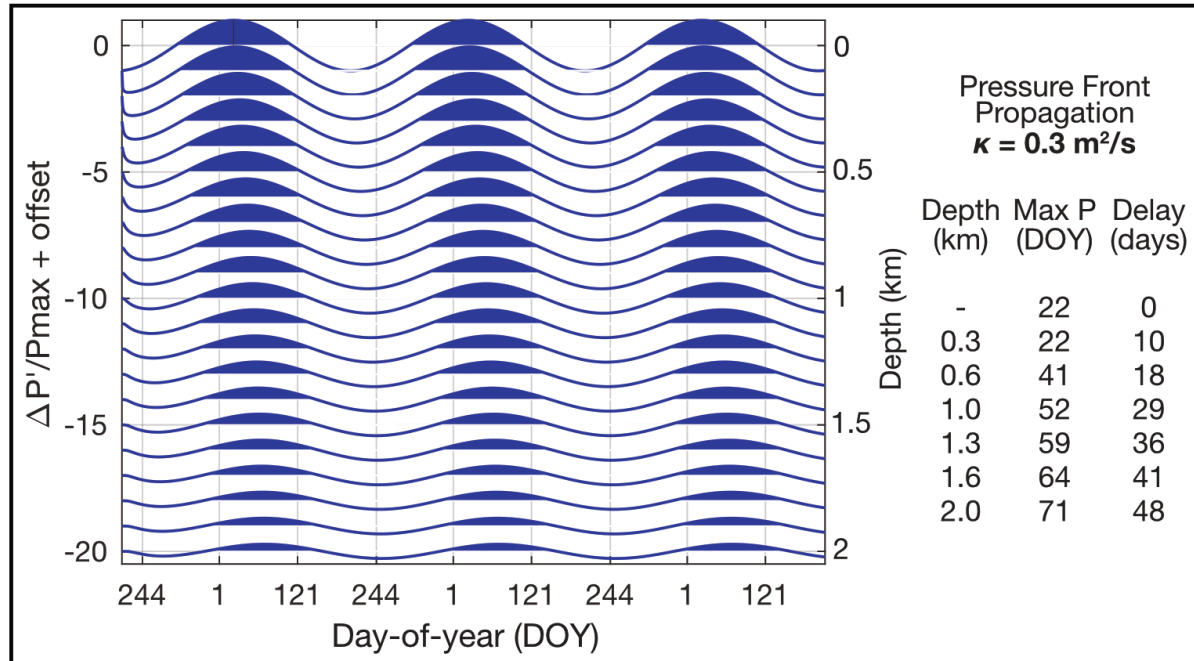
967 **Figure 5.** a) LOS velocity map for period 2015/11/27-2022/12/20. b) Median seasonal phase  
 968 (peak DOY), and (c) amplitude of InSAR deformation time series for water years 2016-2022.  
 969 See Figs. S15 and S16 for yearly phase and amplitude maps, respectively.  
 970



971

972 **Figure 6.** Normalized probability density functions for timing of annual extremes in  
 973 groundwater-related signals across California. Row and line color indicate signal type: **(a)** total  
 974 precipitation in the recharge area of the Sierra Nevada (SN, see Fig. 1a) from SNODAS, **(b)** Sum  
 975 of liquid precipitation and melt water corrected for canopy interception in SN from SNODAS,  
 976 **(c)** Melt water in SN from SNODAS, **(d)** soil storage from hydrological models for GRACE  
 977 region corresponding with the Central Valley (CV, Fig. 1b), **(e)** snow storage from SNODAS for  
 978 CV, **(f)** surface reservoir storage from CDWR for CV, **(g)** GRACE-based estimate of  
 979 groundwater storage for CV, **(h)** total water storage from GRACE for CV, **(i)** vertical land  
 980 motion from GNSS for all available sites in California (CA), and **(j)** for GNSS sites (red) in the  
 981 CV only, and for InSAR pixels in the southern CV from Fig. 5 with a seasonal amplitude larger  
 982 than 3 mm, and lastly, **(k)** groundwater levels from observation wells in CV. See Figure 1 for

983 location of subregions. Each function indicates maximum probability for timing of annual  
984 maximum (a-i, k) or minimum (j) amplitude of the annual signal based on wavelet analysis (Fig.  
985 3 and Fig. S7). Vertical lines represent the mean value for timing of annual maximum.  
986 Distribution is normalized by maximum probability density value and results from year-to-year  
987 variation of the regionally averaged gridded datasets (a-h) and from spatial variation of well and  
988 GNSS data sets (i-k).  
989



990

991 **Figure 7.** Vertical pressure propagation for elevation difference between the Sierra Nevada  
 992 Mountains and the Central Valley aquifers. Normalized pressure change ( $\Delta P'/P_{max}$ ) at different  
 993 depth due to standard 1D calculation of pressure front propagation along mountain block  
 994 recharge conduits in the fractured bedrock of the Sierra Nevada Mountains. Graphs are  
 995 incrementally offset by -1 for each depth. In top groundwater layers, maximum pressure occurs  
 996 on January 22<sup>nd</sup> (DOY 22), which is driven by mean annual water availability in the recharge  
 997 area (Fig. 6b). Table to the right indicates DOY and time delay of the pressure propagation to  
 998 depth of 300-2000 m. Given a hydraulic diffusivity  $\kappa = 0.3 \text{ m}^2/\text{s}$  (reasonable for fractured  
 999 granite bedrocks), the pressure front needs  $\sim 0.6$  (1.2, 1.6) months to propagate to depth of 600  
 1000 (1300, 2000) m. A smaller hydraulic diffusivity would lead to a slower propagation to depth and  
 1001 vice versa, examples for  $\kappa = 0.5, 0.1 \text{ m}^2/\text{s}$  are shown in Figure S14.

1 **Linking Central Valley Deep Aquifer Recharge and High Sierra Nevada Snowpack**

2 **S. Werth<sup>1</sup>, M. Shirzaei<sup>1</sup>, G. Carlson<sup>1</sup>, and Roland Bürgmann<sup>2</sup>**

3  
4 <sup>1</sup>Department of Geosciences, Virginia Polytechnic Institute and State University, Blacksburg,  
5 VA, USA.

6 <sup>2</sup>Dept of Earth and Planetary Science, University of California, Berkeley, CA, USA.

7 Corresponding author: Susanna Werth ([swerth@vt.edu](mailto:swerth@vt.edu))

8  
9  
10 **Key Points:**

- 11 • High Sierra snowpack link to deep Central Valley aquifers via mountain block recharge  
12 is consistent with satellite & in-situ observations.
- 13 • Peak groundwater levels lag Sierra's water peak by one month, consistent with fluid  
14 diffusion time in Sierra's fractured crystalline body
- 15 • New hydroclimate models should account for the role of the Sierra Nevada in  
16 California's water cycle  
17

## 18 **Abstract**

19 California's arid Central Valley relies on groundwater pumped from deep aquifers and  
20 surface water transported from the Sierra Nevada to produce a quarter of the United States' food  
21 demand. The natural recharge to deep aquifers is thought to be regulated by the adjacent high  
22 Sierra Nevada mountains, but the underlying mechanisms remain elusive. We investigate large  
23 sets of geodetic remote sensing, hydrologic, and climate data and employ process-based models  
24 at annual time scales to investigate possible recharge mechanism. Peak annual groundwater  
25 storage in the Central Valley lags several months behind that of groundwater levels, which  
26 suggests a longer transmission time for water flow than pressure propagation. We further find  
27 that peak groundwater levels lag the Sierra Nevada snowmelt by about one month, consistent  
28 with an ideal fluid pressure diffusion time in the Sierra's fractured crystalline body. This  
29 suggests that Sierra Nevada snowpack changes likely impact freshwater availability in the  
30 Central Valley aquifers. Our datasets, analysis and process-based models link the current  
31 precipitation and meltwater in the high mountain Sierra to deep Central Valley aquifers through  
32 the mountain block recharge process. We call for new hydroclimate models to account for the  
33 role of the Sierra in California's water cycle and for revision of the current management and  
34 drought resiliency plans.

35

## 36 **Plain Language Summary**

37 Current trends in hydrology and climate indicate a future in which extreme droughts will likely  
38 become the norm for drier regions. To sustain food production in the Central Valley, California,  
39 a major agricultural producer in the United States with a semiarid climate, groundwater supply  
40 and recharge are crucial to management solutions. We report the first remote-sensing  
41 observations directly linking Sierra Nevada's snowpack and groundwater storage to Central  
42 Valley's deep aquifer system recharge. We highlight the importance of high mountain  
43 groundwater systems in the water cycle, significantly contributing to recharging valley aquifers.  
44 We suggest that Sierra Nevada snowmelt and mountain recharge processes should be included in  
45 Central Valley aquifer models for accurate forecasting of the impact of climate extremes on  
46 groundwater supply and for developing effective drought adaptation and resiliency plans.

47

## 48 **1 Introduction**

49 Understanding key natural and artificial processes in recharging aquifer systems is  
50 essential for sustainable water management to store water for future use (Escriva-Bou et al.,  
51 2020, 2021; Ghasemizade et al., 2019). In arid and semiarid regions, such as the lowland Central  
52 Valley (CV) of California adjacent to the Sierra Nevada Mountains (Fig. 1a), artificial (or  
53 intentional) recharge through basins, unlined canals, and injection contributes to the net recharge,  
54 however, due to the natural disconnect between groundwater overdraft in dry areas and surface  
55 water surplus in wet areas, these contributions are likely small (Alley, 2002; Ayres et al., 2021;  
56 Escriva-Bou et al., 2021; Siebert et al., 2010; Zektser & Everett, 2004). Thus, large-scale natural  
57 recharge to deep aquifers is essential for replenishing dryland groundwater resources. In contrast  
58 to artificial recharge, the mechanism of natural recharge to deep aquifers remains elusive in the  
59 CV.

60 California's wet and dry seasons occur during November-April and May-October,  
61 respectively, with a large portion of the Sierra Nevada's precipitation falling as snow during the  
62 winter that supplies snow melt in spring (Fig. S1, S2). The Sierra Nevada's snowpack is thought  
63 to regulate surface water availability in the CV during the summer (Faunt, 2009; Peterson et al.,  
64 2003; Urióstegui et al., 2017). Isotope studies and streamflow analysis of snow-dominated  
65 mountainous watersheds of the western USA suggest that snowpacks via snowmelt significantly  
66 contribute to groundwater recharge, depending on present geology (Earman et al., 2006; Tague et  
67 al., 2008; Tague & Grant, 2009). But the mechanism linking the Central Valley's deep aquifer  
68 recharge to precipitation, underground storage, and water transport in the Sierra Nevada  
69 Mountains is not well-understood (Huth et al., 2004; Jódar et al., 2017; Liu et al., 2017).

70 Deep valley aquifers adjacent to high mountains, such as the CV, are thought to be  
71 recharged by lateral flows from higher elevations (Feth, 1964). The two main processes  
72 considered are Mountain Front Recharge (MFR) and Mountain Block Recharge (MBR, Fig. 2)  
73 (Somers & McKenzie, 2020). MFR often directly recharges shallow unconfined aquifers and  
74 causes a rise in the water table near streambeds from the mountain front to the basin aquifer.  
75 MBR replenishes deeper, often confined, and semi-confined aquifers laterally connected to high  
76 mountain aquifers (Somers & McKenzie, 2020). MBR occurs through fractures in the mountain  
77 block hydraulically connected to deep valley aquifers. Despite their proximity, there is no  
78 consensus on the role of especially MBR from the Sierra Nevada's granitic bedrock block into  
79 the CV aquifers; thus, it is not considered in current large-scale hydrological models used in  
80 water management assessments (Faunt, 2009; Hanson et al., 2012; Markovich et al., 2019).  
81 Meixner et al. (2016) lumped both processes to mountain system recharge (MSR) and estimated  
82 that it accounts for ~20% of GW recharge in the CV. Recent modeling experiments indicate that  
83 MFR drives almost all of the MSR to the CV aquifers (Schreiner-McGraw & Ajami, 2022).  
84 However, another study based on hydrological modeling concludes that MBR is more important  
85 and contributes up to 23% of the total GW recharge to the CV (Gilbert & Maxwell, 2017). These  
86 hydrogeological studies generally agree on the role of MSR components. However, they disagree  
87 on the importance of MBR for recharging deep valley aquifers of the CV, while the spatial extent  
88 of their investigations remains at scales of smaller watersheds that do not cover the entire CV.

89 An observation of groundwater volume change at the scale of the CV is available from  
90 remote sensing techniques, e.g., via their impact on the gravity field observed by the Gravity  
91 Recovery And Climate Experiment (GRACE) or on surface deformation observations with  
92 Global Navigation Satellite System (GNSS) or Interferometric Synthetic Aperture Radar  
93 (InSAR). Some studies, e.g., Murray & Lohmann (2018), Neely et al. (2021) analyzing high-  
94 resolution deformation maps, suggest direct recharge of deep aquifers from the surface of the CV  
95 following heavy precipitation events and surface water supply surplus during wet years, ignoring  
96 the impermeable clay layers separating shallow and deep aquifers (Faunt, 2009; Shirzaei et al.,  
97 2019) and that there is no evidence of vertical fractures (Carlson, Shirzaei, Ojha, et al., 2020) in  
98 the Valley to provide a direct pathway for the downward flow of surface water. Argus et al.  
99 (2022) use remote sensing data and hydrological models to quantify MBR from the Sierra  
100 Nevada to the CV at about 5 km<sup>3</sup>/yr, though they fail to provide a feasible conceptual or physical  
101 model describing the deep aquifer recharge mechanisms.

102 Quantifying the spatiotemporal relationship between California's high mountains and  
103 deep valley aquifers is essential for developing appropriate plans supporting sustainable  
104 groundwater use. In the climate change era, when drought frequency and intensity have

105 increased globally (Fox-Kemper et al., 2021), including in California (Fig. S3), elevation-  
106 dependent warming (Pepin et al., 2015) disproportionately impacts the water availability and  
107 storage in high mountains. During the last decades specifically, increased evapotranspiration,  
108 decreased or delayed precipitation, and snowfall have caused severe snow droughts in the  
109 western USA, including the Sierra Nevada (Harpold et al., 2017; Hatchett & McEvoy, 2018;  
110 Mote et al., 2018). These droughts also reduce supply for the MBR. Hence, ignoring the MBR  
111 contribution may cause an overestimation of the lowland aquifer resilience to climate change and  
112 excess freshwater demand.

113 During a dry year, up to 70% of the groundwater used in CV is pumped within the  
114 growing season, mainly between April to June (Faunt, 2009), causing a long-term decline in  
115 groundwater levels, with the fastest rates observed in the southern San Joaquin basin (Fig. 1a,  
116 including the Tulare basin) (Faunt, 2009; Faunt et al., 2016; Konikow, 2015; Massoud et al.,  
117 2018; Ojha et al., 2018). Given the poor quality of shallow water in the southern CV (Hanak et  
118 al., 2017), most groundwater demand is addressed by tapping into deep aquifers at ~50 m to  
119 ~500 m depth below the surface, overlain by the confining layer of the Corcoran Clay or other  
120 clay lenses (Fig. 1a). Thus, direct percolation of surface water into deep aquifers is implausible  
121 (Shirzaei et al., 2019), at least at the time scale of a month to a year, corroborated by  
122 groundwater-age data (McMahon et al., 2011). For instance, Burow et al., (2007) reported a  
123 recharge rate of less than 600 mm/yr for unconfined aquifers in San Joaquin Valley. Thus,  
124 ancient groundwater supports California's water supply today (Healy & Scanlon, 2010).

125 Here, we investigate several big time-dependent datasets, including groundwater level  
126 (GWL, Fig. 1a, S4), surface deformation from Interferometric Synthetic Aperture Radar (InSAR)  
127 and Global Navigation Satellite System (GNSS) (Fig. 1b, S5), Gravity Recovery and Climate  
128 Experiment (GRACE) satellite-derived total water storage (TWS), as well as soil storage (SoS),  
129 snow storage (SnS) and reservoir storage (ReS, Fig. 1c) from hydrological data sources. We  
130 further apply sophisticated time-frequency and correlation analysis to identify hidden and non-  
131 stationary patterns in time series, quantifying their relationships. We specifically focus on  
132 investigating seasonal (i.e., annual) variations in hydrologic and geodetic observation time series  
133 that are sensitive to groundwater dynamics and their inter-annual differences. Based on the  
134 analysis, we build a conceptual model for CV deep aquifer recharge that supports the importance  
135 of MBR and agrees with geodetic remote sensing data over the CV.

136

## 137 **2 Materials and Methods**

138 Our study leverages various hydrologic and geodetic datasets, signal processing,  
139 statistical methods and physical models to quantify groundwater dynamics in the CV and Sierra  
140 Nevada Mountains (Fig. 1a).

### 141 **2.1. Water Storage Components, Precipitation, and Snow Melt**

142 GRACE and GRACE Follow-on missions (hereafter referred to as simply GRACE)  
143 monitor monthly changes in the Earth's gravity field at a spatial resolution of ~300-400 km,  
144 which are converted to equivalent total water storage (TWS) changes close to the surface  
145 (Schmidt et al., 2008; Tapley et al., 2004). In California, associated mass variations can be  
146 attributed to the terrestrial water cycle dynamics at sub-seasonal to interdecadal time scales.  
147 Water flow and storage processes on and below the surface change the region's total amount of

148 water stored in the soil, snowcap, surface- (including reservoirs and rivers), and groundwater.  
149 With that, GRACE total water storage variations reflect water loss, e.g., due to drought or human  
150 activities like intense groundwater pumping, as a mass deficit. Vice versa, for wetter periods, the  
151 surplus of water is detected. This allows for predicting groundwater storage in large aquifers if  
152 storage changes in all other components can be quantified and removed from GRACE TWS  
153 (Famiglietti et al., 2011; Scanlon et al., 2012).

154 Here, we derive groundwater storage (GWS) changes from GRACE observations using  
155 an approach similar to Ojha et al. (2019). We retrieve GRACE TWS variations from the RL06  
156 Level-3 product from NASA's Jet Propulsion Laboratory (JPL) that solves regional mass  
157 variations at a resolution of 3-degree. We do not apply JPL-mascon scale factors, as we calculate  
158 groundwater changes at this native resolution, and we assume leakage between the mascon tiles  
159 to be neglectable. To separate GWS changes from GRACE TWS, we retrieve mass variations in  
160 other storage compartments from multiple data sets. We acquire soil moisture variations from all  
161 available soil layers in the NOAH, CLSM and VIC models of the Global Land Data Assimilation  
162 System (GLDAS) Version 2.1 (Beaudoin & Rodell, 2016; Rodell et al., 2004) at 0.25 (Noah)  
163 and 1-degree (CLSM and VIC) resolution, respectively, for the entire GRACE period. We  
164 average the three models to one ensemble dataset for further analyses after resampling them to a  
165 uniform 0.5-degree resolution (Fig. 1c). For comparison, we also retrieve soil storage changes  
166 from the WaterGAP Global Hydrological Model (WGHM, version 2.2d) at 0.5-degree  
167 resolution, which is available until 2016 (Fig. S12a). We integrate reservoir storage (ReS)  
168 changes from 18 reservoirs with capacities larger than or equal to 0.9 km<sup>3</sup>, inside the margins of  
169 the two mascon cells covering the CV (GRACE region, Fig. 1b), which are retrieved from the  
170 California Department of Water Resources (CDWR, 2017). Snow storage (SoS) changes are  
171 acquired in the form of snow water equivalent from the Snow Data Assimilation System  
172 (SNODAS) (NOHRSC, 2004) over the contiguous United States since the end of 2003. Monthly  
173 water mass variations for each storage compartment are summed across the GRACE region and  
174 the regionally aggregated SoS, SnS and ReS variations are removed from GRACE TWS  
175 variations for this area, after Ojha et al. (2019). The resulting time series for each storage  
176 compartment, including groundwater storage changes during both GRACE mission periods, are  
177 shown in Figure 1c. We assume the GRACE based estimate of GWS to be dominated by  
178 groundwater variations in the CV, where porosity of the aquifers is much larger than that in the  
179 SN Mountains.

180 From the SNODAS dataset we further retrieve driving and output variables related to  
181 snow cover, including 'solid'- and 'liquid precipitation', and 'snowmelt runoff at the base of the  
182 snowpack', to investigate these fluxes in the Sierra Nevada Mountains (Fig. S1, S2) and their  
183 correlation to groundwater dynamics.

## 184 2.2. Groundwater Levels

185 Groundwater availability in the CV is conventionally monitored as water level change in  
186 observation and irrigation wells. The data archives from the United States Geological Survey  
187 (USGS) and the California Department for Water Resources (CDWR) provide more than 40,000  
188 records from wells within the CV. The records have varying start dates, not all are continuously  
189 monitored until today, and only some records provide sufficient temporal sampling rates to study  
190 seasonal variations in GWLs. For this study we have screened 'daily data' and 'field data'  
191 archives from the USGS (USGS, 2021) as well as 'continuous data' and 'periodic data' archives

192 from CDWR (CDWR, 2019) in California and selected records that cover the GRACE mission  
193 period from 2002 to 2020. We have excluded records labeled as ‘irrigation well’ and only  
194 selected sites labeled ‘observation well’. Water levels in irrigation wells are potentially affected  
195 by the localized reduction in pressure during and after pumping from the well. Levels in  
196 observation wells are more likely to represent a regional state of pressure and storage changes in  
197 the entire aquifer. In addition, we categorized data entries that are larger than 3.5 times the  
198 standard deviation of the detrended time series as outliers and excluded them. Moreover, about  
199 half of the records have daily sampling rates and we excluded entire records from the  
200 field/periodic datasets that have less than six entries per year on average. From the initial dataset,  
201 2128 time series (371 from USGS and 1727 from CDWR) provide observation records during  
202 2002-2020 inside the CV. Only 682 records cover at least three years with less than 3 months of  
203 gap (Fig. S4); of those, we select 457 records gathered at depths deeper than 50 m since we want  
204 to focus on time series measured in semi-confined and confined aquifers. About half of the 457  
205 available records are longer than 10 years (Fig. S4a-c). We note that these records were taken at  
206 only 250 unique well locations (circles in Fig. 1a), with some sites containing up to five nested  
207 level meters (Fig. S4d). Most deep sensors at each site are located 50 m to 300 m below the  
208 surface, with about half of the sensors reaching not more than 200 m deep and only a few are 450  
209 m deep or deeper (Fig. 1a, S4e, f). Most usable wells are in the northern Sacramento Valley and  
210 only two dozen sites are in the southern San Joaquin Valley, where only 22 wells measure water  
211 level variations at depths below the Corcoran clay. Examples of GWL time series are shown in  
212 Figure 1a.

### 213 2.3. Surface deformation

214 Surface deformation due to TWS change, including GWS, occurs through two different  
215 processes. Total water mass deforms Earth’s elastic crust, resulting in subsidence for an increase  
216 and uplift for a decrease in water mass. This deformation process has been described and  
217 inverted to quantify TWS in California (Adusumilli et al., 2019; Argus et al., 2022; Borsa et al.,  
218 2014; Carlson et al., 2022; Carlson, Shirzaei, Werth, et al., 2020; White et al., 2022). A second  
219 poroelastic deformation process is due to only groundwater changes occurring in semi-confined  
220 or confined aquifers, where pore spaces and granular matrix of rocks compact and groundwater  
221 levels fall under reduced water pressure. The opposite happens for increasing water pressure.  
222 Changes in water pressure in an aquifer can either be caused by net recharge or discharge, i.e.  
223 GWS change, in the aquifer itself, or initiated by water pressure propagating between the aquifer  
224 and a hydraulically connected outside region (Fetter & Kreamer, 2022). Decades of falling  
225 groundwater levels in the CV deep aquifers have caused continuous land subsidence at the  
226 surface and have been observed to be most severe during droughts (Galloway et al., 1999; Ojha  
227 et al., 2018; Smith et al., 2017; Vasco et al., 2022). It has been shown that elastic loading  
228 deformation in California is of the opposite sign and up to two magnitudes smaller than the  
229 poroelastic deformation occurring at the surface of the CV (Carlson, Shirzaei, Werth, et al.,  
230 2020).

231 To study seasonal variations in vertical land motion (VLM) since the early 2000s, we use  
232 vertical deformation time series from the daily tenv3 GNSS solutions from the Nevada Geodetic  
233 Laboratory (NGL). The solutions are processed at NGL using GipsyX software and are  
234 transformed into the IGS14 reference frame. Additional processing information can be found on  
235 the NGL website (<http://geodesy.unr.edu/gps/ngl.acn.txt>). We do not apply any further  
236 corrections to the GNSS time series for the rest of the analysis. From 1184 stations in California,

237 we selected 170 with a minimum record of 5 years between 2002-2020 and exhibiting a seasonal  
238 amplitude larger than the time series median standard deviation. Most stations began  
239 observations around 2008, with a length of 15 years (Fig. S5b). Of these stations, 37 are located  
240 within the CV boundaries (red triangles, Fig. 1b). Example time series at three sites throughout  
241 the study area are shown in the inset of Figure 1b. We determine the seasonal component of  
242 GNSS vertical land motion and the timing of maximum uplift and maximum subsidence using a  
243 time-frequency analysis (see Section 2.4).

244 We further measure the surface deformation in terms of line-of-sight (LOS) over the  
245 southern CV using Interferometric Synthetic Aperture Radar (InSAR). The SAR dataset includes  
246 238 C-band images from descending track, path 144, of Sentinel-1A/B satellites spanning  
247 2015/11/27-2022/12/20. We apply multi-looking factors of 32 and 6 in range and azimuth to obtain  
248 a pixel dimension of  $\sim 75\text{m}$  by  $\sim 75\text{m}$ . We use GAMMA software (Werner et al., 2000) to create a  
249 large set of interferograms. The interferograms are selected, so they form triplets, and the numbers  
250 of short, medium, and long temporal baseline pairs are comparable to minimize the phase closure  
251 error impact (Lee & Shirzaei, 2023). We apply the wavelet-based InSAR (WabInSAR) (Lee &  
252 Shirzaei, 2023; Shirzaei, 2013; Shirzaei et al., 2017) algorithm to perform a multitemporal  
253 interferometric analysis of the SAR dataset and create high-accuracy maps of surface deformation  
254 time series. A Shuttle Radar Topography Mission (SRTM) Digital Elevation Model (DEM) of 1-  
255 arcsecond ( $\sim 30\text{ m}$ ) spatial resolution (Farr et al., 2007) and precise satellite orbital information are  
256 used to estimate and remove the effect of topographic phase and flat earth correction (Franceschetti  
257 & Lanari, 1999). The absolute phase values are obtained by applying a 2D minimum cost flow  
258 algorithm (Costantini, 1998), then combined to create a Line-of-Sight (LOS) time series of surface  
259 deformation by using a reweighted least squares approach. The spatially correlated and temporally  
260 uncorrelated atmospheric delay are also estimated and removed (Shirzaei, 2013).

## 261 2. 4. Time-Frequency Analysis

262 To investigate the temporal variations in water storage components, GWLs, and  
263 deformation data, we perform a time-frequency analysis using a continuous wavelet transform,  
264 following Shirzaei et al. (2013). The wavelet transform allows decomposing signals into building  
265 blocks based on frequency contents. In contrast to the Fourier transforms, the wavelets can  
266 handle non-stationary signals and localize the signal energy in the time and frequency domain  
267 (Goswami & Chan, 1999). Wavelets have a key parameter scale (or dilation), which stretches or  
268 squishes the wavelet function and relates to the analyzed signal frequency. To perform wavelet  
269 analysis, we use the Matlab packages provided by Torrence and Compo (1998) and Erickson  
270 (2019) and apply the wavelet family of derivatives of gaussian (DOG, Fig. S6) at 200 levels of  
271 decomposition or scales. The temporal sampling of all time series is either daily or resampled at  
272 daily intervals.

273 Figures 3 and S7 illustrate our approach with an example of groundwater level time series  
274 at the DWR well 387793N1218123W004 (Fig. S7a). The wavelet power spectrum map (PSM,  
275 Fig. 3a and S7b) shows the signal's energy breakdown into several frequency components and  
276 their relative importance based on the amplitude of the PSM. A cone-of-influence overprinted on  
277 the spectrum indicates areas where edge effects play a role, and therefore, the PSM cannot be  
278 interpreted. Signal energy in areas inside the cone of influence is strongest at periods of about  
279 one year, with contour lines indicating their statistical significance with respect to white and red  
280 noise (with a lag-1 autocorrelation parameter of 0.85 for the latter) (Torrence & Compo, 1998).

281 Figure 3 also shows examples of wavelet PSM for selected GWL, VLM, and TWS component  
282 time series.

283 To isolate the annual component from the time series, we set the PSM to zero except for  
284 periods between 0.75-1.25 years and then apply an inverse wavelet transform of the new PSM  
285 (Fig. S7c). This approach considers that the annual components in climate-related processes do  
286 not have an exact one-year period. We further analyze the reconstructed annual signals to  
287 characterize the timing of annual maxima, minima, and the timing of fastest rate declines and  
288 increases (blue, red, and gray circles in Fig. S7c). We summarize the annual values for several  
289 years through temporal averaging using the median operator to retrieve the timing of maximum  
290 in the annual signal (e.g., as shown in Fig. 4). The same approach is applied to the time series of  
291 GWL, TWS components, GNSS and InSAR vertical deformation.

292 Probability density functions (PDFs) for spatiotemporal variation of timing of annual  
293 peaks were calculated using MATLAB's probability density estimator *kdensity()*, based on a  
294 normal kernel function for univariate distributions and applies a kernel smoothing window with  
295 an optimized bandwidth for normal densities.

## 296 2.5. Vertical Diffusion Model

297 In the high Sierra Nevada Mountains, a significant portion of snow melt water (Fig. S1,  
298 S2) infiltrates into the ground and recharges top aquifer layers (Peterson et al., 2003; Urióstegui  
299 et al., 2017), which are hydraulically connected to the CV aquifer system (Faunt, 2009). Here, to  
300 obtain the first-order approximation of the diffusion time, namely the time it takes for snow melt-  
301 related pore-fluid pressure increase in the Sierra to reach deep aquifer layers of the CV via MBR,  
302 we apply a first-order process-based 1D diffusion model following (Saar & Manga, 2003). The  
303 vertical propagation of hydrostatic pore-fluid pressure  $P'$  at depth  $z$  over time  $t$  is governed by  
304 the diffusion equation:

$$305 \quad \kappa \frac{\partial^2 P'}{\partial z^2} = \frac{dP'}{dt} . \quad (1)$$

306 with the hydraulic diffusivity  $\kappa = K/S_s$ , which controls how fast pressure will propagate to  
307 depth. It is given by the ratio of vertical hydraulic conductivity  $K$  to specific storage  $S_s$ . The  
308 diffusivity of unfractured granite bedrock has values of around  $\kappa = 10^{-4} \text{ m}^2/\text{s}$  (Wang, 2000).  
309 However, for fractured volcanic rock, values as high at  $0.3 \text{ m}^2/\text{s}$  (Saar & Manga, 2003), and  $1$   
310  $\text{m}^2/\text{s}$  (Gao et al., 2000), consistent with the range provided by Talwani and Acree (1985), or  
311 even up to  $7.9 \text{ m}^2/\text{s}$  (Montgomery-Brown et al., 2019) are suggested. Here, we consider  
312 diffusivity values of 0.1, 0.3 and  $0.5 \text{ m}^2/\text{s}$  for Sierra's crystalline fractured rocks.

313 We solve the parabolic differential Equation 1 using the function *pdepe()* from the  
314 Matlab software by setting the initial pressure conditions to zero and the boundary conditions of  
315 the pore-fluid pressure to a periodic variation with periodicity  $\psi$  of 1 year, annual amplitude  
316  $P_{max}$  and annual phase  $\varphi_0$ :

$$317 \quad P'_{z,t=0} = P_{max} \cdot \cos\left(\frac{2\pi}{\psi} t + \varphi_0\right), \quad (2)$$

318 where at depth  $z$ , pore-fluid pressure is  $P_{z,t} = P_{z,t-1} + P'_{z,t}$ . We are only interested in changes  
319  $P'_{z,t}$  of pore-fluid pressure.

320 Assuming saturated conditions and solving Equations 1 and 2 for  $t$  allows us to estimate  
 321 the time it takes to increase pore-fluid pressure annually due to groundwater recharge reaching  
 322 vertically from top groundwater layers to depth  $z$ . The duration of pressure propagation to deep  
 323 aquifer layers is independent of the amplitude of pressure change at the surface and a normalized  
 324 solution for  $P'_{z,t=0}/P_{max}$  is sufficient. The time delay estimate is most sensitive to the  
 325 magnitude of the hydraulic diffusivity  $\kappa$  (Eq. 1) as well as the phase  $\varphi_0$ , of the annual pressure  
 326 variation due to recharge (Eq. 2). We assume that the horizontal diffusivity of the aquifer is large  
 327 enough, so the lateral diffusion time is relatively negligible (Fetter & Kreamer, 2022).

328 The annual phase of pressure variations in upper groundwater layers in the high Sierra  
 329 Nevada Mountains  $\varphi_0$  may be derived from the annual variation in water available for recharge  
 330 in this region, which we quantify as follows. The top groundwater layers in the Sierra Nevada  
 331 receive inflow from snow melt water and liquid precipitation (i.e., rainfall). Urióstegui et al.  
 332 (2017) and Bales et al. (2011) found that only 10-20% of the snow melt water in the Sierras runs  
 333 off through streams, with the remainder being lost to drainage into deep layers and  
 334 evapotranspiration. We assume that all of the melt water initially increases pressure in the upper  
 335 groundwater layers of the Sierra Nevada Mountains, before evaporating or running off. Also, we  
 336 neglect the delay between the time that water for infiltration becomes available and its  
 337 percolation into the upper groundwater layers of the Sierra Nevada Mountains. We consider  
 338 these assumptions reasonable for wide areas of exposed fractured bedrock and given that we are  
 339 only interested in quantifying the phase, not the absolute value of maximum pressure variations.  
 340 For that, we retrieve the time series of SNODAS dataset variables ‘snowmelt runoff at the base  
 341 of the snowpack’  $M$  and ‘liquid precipitation’  $P_{liqu}$  (see Section 2.1, Fig. S1) averaged for the  
 342 drainage area of the Sierra Nevada toward the CV (rose-shaded area in Fig. 1a). We correct  
 343 liquid precipitation for canopy interception by a relative value of 20% (Vrugt et al., 2003), as this  
 344 intercept changes the relative amplitudes between  $M$  and  $P_{liqu}$ , and therefore, it can impact the  
 345 annual phase. Finally, we get a time series of total water available for recharge in the Sierra  
 346 Nevada drainage area from  $(P_{liqu} - 0.2 \cdot P_{liqu} + M)$  and quantify monthly mean values of this  
 347 time series during 2002-2020 (Fig. S2c). We also determine the mean timing of the annual peak  
 348 for each year and at each location in the drainage area, which we apply as the timing of the  
 349 annual maximum of the pressure variation to constrain  $\varphi_0$  for the boundary condition in  
 350 Equation (2).

## 351 4 Results

### 352 4.1. Year-to-Year Water Variability

353 The time series of TWS variations obtained from the GRACE satellites (Tapley et al.,  
 354 2004, 2019) and their components measured through in-situ observations (e.g., wells) (Alam et  
 355 al., 2021) or water balance models (Faunt, 2009; Li et al., 2018) are characterized by annual  
 356 variations attributed to overall dynamics in the terrestrial water cycle (Tang & Oki, 2016).  
 357 Several example time series are shown in Figure 1c. A less obvious pattern comprises the  
 358 interannual variations in the amplitude of the annual signal. Identifying the amplitude and timing  
 359 of the peak annual and interannual signal components allows for resolving the temporal scale at  
 360 which the connected systems interact.

361 To this end, we apply the wavelet-based time-frequency analysis to extract hidden  
 362 patterns in the datasets (see Section 2.2.1, Fig. S6). The results from the time-frequency analysis

363 are shown in the form of a PSM, distributing the signal's power into frequencies (or periods) and  
 364 time intervals (Fig. 3, S7). We find maximum amplitudes characterize the PSMs associated with  
 365 different time series at equivalent periods of 1 year and 3-8 years (Fig. 3). These frequency  
 366 components are associated with general variations in water availability associated with  
 367 atmosphere-ocean interactions, influencing water cycles in the Southwest USA (Quiring &  
 368 Goodrich, 2008). Significant drought periods, such as during 2007-2009 and 2012-2015 (Fig.  
 369 S3), correspond with cool phases of El Niño Southern Oscillation (ENSO) recurring every 3-7  
 370 years, the cool phase of the Pacific Decadal Oscillation (PDO), and the warm phase of the  
 371 Atlantic Multidecadal Oscillation (AMO) (McCabe et al., 2004; Quiring & Goodrich, 2008). The  
 372 length of our observation does not allow for resolving signal components over a decade or  
 373 longer, as indicated by the cone of influence, the shaded region in the PSM.

374 Some PSMs also show unique patterns. For instance, the PSMs of GWL changes (Fig.  
 375 3a) and GNSS VLM (Fig. 3b) exhibit components at periods of 0.5 and 3 years, albeit the  
 376 component of 0.5 years for VLM disappears following 2008. In contrast, the PSM of SnS (Fig.  
 377 3e) shows only a transient component over a period of 3 years. PSM of GWS variations (Fig. 3g)  
 378 shows a transient component of 1 year period. Notably, the location and amplitude of peak PSM  
 379 are not constant and change over time, especially for TWS, SnS, ReS, and GWS variations and  
 380 to a lesser extent in SoS due to water availability changes within wet and dry seasons and in  
 381 between them as well as due to human interventions. For instance, the amplitude of annual  
 382 components was reduced or diminished during the drought years 2007-2010 and 2012-2015.  
 383 During these periods, reservoirs were not refilled, and the Sierra Nevada received little  
 384 precipitation, reducing the amplitude of the corresponding annual components (Fig. 3e and 3f).  
 385 The amplitude of the annual component of GWS variations vanishes during the same years (Fig.  
 386 3g).

387 Figure 3h presents the isolated annual components for all the time series comprising PSM  
 388 components of 0.75 to 1.25 yr periods, which display non-stationary behaviors, i.e., the  
 389 amplitude changes over time. We find that year-to-year TWS is experiencing the most  
 390 pronounced changes and GWS the least. We also note that year-to-year peak extremes do not co-  
 391 occur for different time series. For instance, during the 2012-2015 drought, TWS, SoS, and ReS  
 392 variations experienced their lowest amplitudes in 2013 and 2014, while that of GWS occurred  
 393 two years later during 2016, following the snow-poor years in 2014 and 2015. Characterizing  
 394 such inter-annual variability in water cycle components improves understanding of hydroclimate  
 395 extremes and water storage capacity in the region (Yin & Roderick, 2020).

396

#### 397 4.2. Timing of the Seasonal Signal

398 We further investigate the spatial variability of the timing of the peak annual amplitude of  
 399 TWS and its components across the study region (Fig. 4). Note that spatial detail cannot be  
 400 resolved from the GRACE TWS with 300-400 km spatial resolution. To this end, we find the  
 401 day-of-year (DOY) corresponding with the peak of the timeseries of the annual components and  
 402 then obtain the median of DOY for each time series. Figure 4 plots the median peak DOY for  
 403 each dataset at their original spatial resolution, except for GWL and VLM, where the values are  
 404 interpolated with an inverse distance weighting scheme and a 25 km radius. The median peak  
 405 DOY for GWL is uniform across the Valley (Fig. 4a, S8) with negligible interannual variability  
 406 (Fig. S9). GWL peaks occur from February to March (Fig. 4a, S8a) and minima in August (Fig.

407 S8b). The fastest GWL rate increase (i.e., the mid-point between annual minima and maxima)  
408 occurs during November (Fig. S8c), and the fastest GWL rate decrease (i.e., the mid-point  
409 between annual maxima and minima) occurs during May (Fig. S8d). These observations are  
410 consistent with the timing of maximum pumping in the CV during April-June. A linear  
411 correlation of 0.3 was found between observation well depth and peak DOY, indicating GWL  
412 rises slightly later in the year at deeper wells (Fig. S8a, left inset). Compared with GWL, the  
413 median peak DOY of GNSS VLM in the CV is spatially more variable (Fig. 4b and S10), with  
414 negligible interannual variability (Fig. S11). We find a bimodal distribution for this peak DOY  
415 (inset in Fig. S10a), with about a third of the stations within the CV peaking from March to April  
416 and most of the remaining stations from September to October. A bimodal behavior is also  
417 observed in the median DOY of annual VLM minima. The median DOY of the fastest VLM rate  
418 increases and decreases are also obtained (Fig. S10), indicating a smaller interannual variability  
419 than that of peak DOY (Fig. S11). We further estimate the median peak DOY of TWS, SoS, SnS,  
420 ReS, and GWS within the GRACE region (Fig. 1b), all of which show spatially uniform patterns  
421 but are distinct from each other (Fig. 4c-g), with spatial DOY averages of 93, 70, 65, 102, and  
422 156 days, respectively.

423 We performed a similar analysis using InSAR LOS deformation observations. Figure 5a  
424 shows the LOS velocity field measuring up to 18.5 cm/yr subsidence in some parts of San  
425 Joaquin Valley. We obtained seasonal phase (peak DOY) and amplitude (Fig. 5b, c) for the  
426 southern CV covered by the Sentinel-1 frame. The spatial distribution of median peak DOY  
427 generally agrees with that of GNSS (Fig. 4b). The denser spatial sampling from the InSAR  
428 analysis, however, reveals an outward propagation of the median annual peak DOY from the  
429 center of CV. Although it varies yearly, the overall outward propagating pattern of peak DOY  
430 remains similar through wet and dry years (Fig. S15). We note that this result is opposite to what  
431 was found by Neely et al. (2021), who suggested an inward propagation of the annual peak  
432 towards the center. Figures 5c and S16 show the median and yearly seasonal amplitude of  
433 surface LOS deformation, reaching up to 4 cm, with the largest value during dry years.

434 Next, we investigate the empirical probability density function (PDF) of annual peak  
435 DOY associated with all components of TWS and deformation and several other relevant  
436 hydrological datasets (Fig. 6). Shown are normalized PDFs of annual peak DOY obtained for  
437 each year and each time series without temporal averaging, thus the interannual variabilities are  
438 preserved. Comparing different PDFs, we find for the Sierra Nevada that precipitation generally  
439 peaks in early January, with a mean DOY of 16 (Fig. 6a), meltwater in late February, DOY 55  
440 (Fig. 6c), and the total water availability (combination of precipitation, meltwater, and canopy  
441 interception) in late January, DOY 22 (Fig. 6b). We obtain a wide distribution for the influxes,  
442 and years with a later maximum melt typically have a larger peak, causing the right-skewed  
443 distribution of annual peak DOY of snowmelt (Fig. S2b). The annual SoS peak for the CV  
444 occurs in March, DOY 70 (Fig. 6d), ~2-3 months after precipitation peaks. SnS peaks in March,  
445 ReS and TWS ~1 month later in April, while GWS of the CV peaks in June (Fig. 6e-g). The  
446 VLM minima (i.e., subsidence) across California, outside of the CV, co-occur with TWS  
447 maxima around April, DOY 93 (Fig. 6i). In contrast, GNSS VLM inside the CV (Fig. 6j) peaks  
448 together with GWL (Fig. 6k) around March, DOY 65, and ~3 months before GWS based on  
449 GRACE and composite hydrology (Fig. 6g). Peak VLM inside the CV derived from high-  
450 resolution InSAR maps (Fig. 6k, dashed line) have a more complex distribution, with the first  
451 peak co-occurring with GNSS and well levels around beginning of March and a later peak  
452 ranging from beginning to end of April. We further observe a delay of 43 days between total

453 water available for recharge in the Sierra Nevada Drainage area (DOY 22, Fig. 6b) and GWL in  
454 the CV (DOY 65, Fig. 6k).

455 To investigate whether the mean values of the PDFs in Figure 6 were significantly  
456 different, we performed a two-sample mean difference hypothesis test using the t-distribution  
457 (Meyer, 1970). We formulated the null hypothesis so that the mean values were the same and  
458 tested the hypothesis at a significance level of 0.05. The test was rejected, hence, the mean  
459 values are statistically the same for all pairs of PDFs in Figure 6, except between GNSS uplift  
460 (CV) and GWL (CV), between TWS and GNSS Subsidence (CA), between SnS (Sierra Nevada)  
461 and GNSS uplift (CV), and between SnS (Sierra Nevada) and GWL (CV).

462 When estimating PDFs for the timing of annual peaks of SoS and GWS (Fig. 6e and 6g),  
463 the variability among the individual SoS models was considered (Fig. S12). SoS timing varies by  
464 about ~2 months from January to February (Fig. S12c). We propagate the variation of SoS  
465 timing toward that of GWS by estimating GWS for each individual soil model (Fig. S13a). The  
466 resulting annual GWS timing varies ~2 months from May to July (Fig. S13b,c). This variability  
467 was included when calculating mean, median, standard deviation, and PDFs of annual GWS  
468 timing (Fig. 6g). Although GWS also depends on the timing of TWS, SnS and ReS, annual  
469 amplitudes of SnS and ReS are only 10% of TWS (Fig. 1c). Therefore they will only marginally  
470 impact the calculation of annual timing of GWS. We assume a minimal measurement uncertainty  
471 for the timing of TWS.

#### 472 4.3. Pressure Diffusion From the High Mountains to Deep Valley Aquifers

473 Earlier studies (e.g., Gilbert and Maxwell (2017)) have suggested that a natural  
474 connection should exist between deep CV and High Sierra Nevada mountain aquifers through  
475 the fractured granite of the mountain block. We provide a first-order estimate for the diffusion  
476 time, the time it takes for a pressure front to vertically diffuse from the top aquifer layers in the  
477 Sierra Nevada Mountains down to elevations of the deep CV aquifers (Section 2.5, Eq. 1). If we  
478 quantify that using a hydraulic diffusivity  $\kappa = 0.3 \text{ m}^2/\text{s}$  for Sierra's crystalline fractured rocks, it  
479 takes 18-36 days for the pressure to travel vertically to depth of 600-1300 m (Fig. 7). We further  
480 consider a range for the vertical hydraulic conductivity and evaluate the diffusion time for  $\kappa =$   
481  $0.1 \text{ m}^2/\text{s}$  and  $\kappa = 0.5 \text{ m}^2/\text{s}$  to depth of 600-1300 m, corresponding with 34-73 days and 12-23  
482 days (Fig. S14), respectively.

## 483 5 Discussions and Conclusions

484 This study performs time-frequency analyses of large hydrologic and geodetic datasets across  
485 California with various spatiotemporal resolutions and uncertainties to characterize the annual  
486 peak DOY, interannual peak amplitude variations, and correlative behaviors across these  
487 observations. We observe relatively low seasonal peaks during droughts for all water storages  
488 (Fig. 3h). However, only for storages in snow and groundwater wavelet PSMs vanish completely  
489 at periods of around one year during droughts when snow cover was diminished to absent during  
490 2007 and 2012-2015 (Fig. 1c, 3e, 3g). We interpret this correlation as an indicator that the  
491 volume of the snowpack and the following snowmelt played a substantial role in groundwater  
492 recharge in the CV. Once corrected for SoS, SnS, and ReS, GRACE measures a combination of  
493 GWS change in shallow and deep aquifers. Hence, we consider snow to be relevant for both  
494 MFR and MBR, with the former mechanism being more relevant for replenishing the shallow

495 and the latter more relevant for (slow) flow to the deep aquifers, given the depth of their flow  
496 path.

497 We further observe that GNSS VLM and InSAR LOS peak DOY vary across California.  
498 The peaks for stations inside the CV co-occur with that of GWL (Fig. 6j, k), specifically at the  
499 sites near the center of the Valley, where aquifer confining layers are thick and observed annual  
500 amplitudes are large (Fig. 5). This indicates the presence of poroelastic aquifer deformation due  
501 to groundwater pumping (Ojha et al., 2018; Smith et al., 2017). In contrast, the VLM peak  
502 minima for stations outside the Valley co-occur with that of TWS peak maxima (Fig. 6h, i),  
503 attributed to the variations in elastic water loading (Argus et al., 2017; Carlson et al., 2022;  
504 Johnson et al., 2017). Interannual variability in the peak amplitudes impacts the hydroclimate  
505 trends, changing baselines used to assess the future risk of climate extremes and vulnerability of  
506 water resources (Stevenson et al., 2022). In summary, a similar peak DOY suggests that some  
507 components of the hydrological system act in concert with or respond elastically to similar  
508 forcing of the hydroclimate or to anthropogenic factors. In contrast, a different peak DOY may  
509 indicate a cascading nature of the response to forcing governed by a time-dependent process.

510 Here we propose that MBR is the fundamental process, allowing long-term recharge to  
511 deep aquifers in the CV. The feasibility of this mechanism is demonstrated in Fig. 7, where a  
512 first-order process-based pressure diffusion model quantifies the lag between peak pore pressure  
513 in the Sierra Nevada aquifers due to snowmelt and peak pore pressure within deep CV aquifer  
514 layers. We estimate the lag at about a month, ignoring the lateral diffusion time, which is often  
515 negligible for permeable aquifers such as CV (Fetter & Kremer, 2022). Given the uncertainty  
516 range of hydraulic diffusivity (Somers & McKenzie, 2020), the estimated diffusion time agrees  
517 well with the lag between peak water availability in the mountains and peak water level in deep  
518 aquifers (Fig. 6b and k). This agreement supports the hypothesis that high mountain aquifers are  
519 connected to deep valley aquifers through pressure propagation from MBR, and that it drives  
520 seasonal well level changes in the deep CV aquifers. The peak GWL in March likely occurs  
521 early due to anthropogenic influence since heavy groundwater pumping typically onsetting from  
522 April to May. A later GWL peak would suggest a longer vertical diffusion time, consistent with  
523 the considered range for tested hydraulic conductivities.

524 We further observed an outward migration of the InSAR LOS peak DOY from the center  
525 of CV (Figs. 5 and S15), which is at odds with the previously published works (e.g., Neely et al.,  
526 2021) that suggested an inward propagation of annual peak DOY from the Sierra Nevada  
527 Mountains toward the center of the CV. They suggested that MFR fed by surface water flowing  
528 off the Sierra Nevada may replenish aquifers (deep and shallow) seasonally across the southern  
529 CV (Neely et al., 2021). However, the MFR mechanism is implausible to recharge deep confined  
530 aquifers (Shirzaei et al., 2019) due to the presence of the impermeable Corcoran clay layer and  
531 other clay lenses (Faunt, 2009) and little evidence of widespread vertical cracks and deep  
532 extensional fissures in the Valley (Carlson, Shirzaei, Ojha, et al., 2020) to provide a potential  
533 pathway for water to percolate deep into the aquifers, though further research on tension  
534 cracking and fissure initiation in the Valley is needed (Carlson, Shirzaei, Ojha, et al., 2020). In  
535 contrast, our hypothesis of MBR linking Sierra groundwater to deep CV's aquifers is consistent  
536 with Darcy's fluid flow law, linking the fluid discharge rate to the hydraulic head gradient  
537 between two given points, scaled with the hydraulic conductivity. Under constant hydraulic  
538 conductivity, the largest discharge happens to the point of the lowest hydraulic head. In CV, it is  
539 logical to assume the zone of the fastest subsidence rate is where the heads are lowest, consistent

540 with groundwater level observation. Thus the recharge from Sierra should replenish aquifers near  
541 the center of Valley first and then propagate outward from the center to areas with smaller  
542 hydraulic gradients, as observed here. Hence, we interpret the InSAR LOS observation of annual  
543 peak DOY as additional support for the hypothesis of a direct pressure link between the Sierra  
544 Nevada aquifers and CV deep aquifers through mountain block conduits.

545 An unexpected finding is the phase difference between annual peaks of GWL in deep  
546 confined aquifers, and GWS in the entire CV aquifer system (including confined and unconfined  
547 units, Fig. 4a, 4g, 6g and 6k) is about three months. This indicates that different processes  
548 influence GWS and well levels. In confined units, the well level change is driven by changes in  
549 groundwater storage and pore fluid pressure, while the gravity-derived measurements only detect  
550 the change in mass, hence, storage changes. During the spring, pressure rises faster in the deep  
551 aquifers than storage is recovered in the entire aquifer system. A vertical hydraulic connection  
552 via MBR flow paths would allow pressure change propagation from the mountain to CV aquifers  
553 at seasonal time scales. However, direct water seepage along MBR flow paths takes centuries to  
554 millennia (Berghuijs et al., 2022). The proposed mechanism here does not require water  
555 percolation and is consistent with the tracer findings that deep groundwater in the CV is  
556 primarily old (McMahon et al., 2011). Our results further emphasize that vertical pressure  
557 propagation occurs faster than net recharge (i.e., detected as storage change) from the mountain  
558 aquifers to the valley aquifers. The later peak in GWS might be primarily driven by annual  
559 variations in top unconfined aquifer layers (Vasco et al., 2022), which would recharge faster than  
560 deep aquifers. This is also consistent with the relatively late mean annual peak in melt water  
561 occurring during early May (see Fig. S2), hence, a long lasting supply for recharge through  
562 surface-groundwater links along the mountain fronts until late spring. At annual time scales,  
563 MFR likely contributes a significant portion to storage changes in shallow aquifers, and the  
564 seasonal variation in GRACE GWS mainly comprises such shallow aquifers instead of deep  
565 aquifers. In this case, the seasonal well level rises in deep CV aquifer layers may be driven  
566 dominantly by pressure variability rather than storage variability. It should also be noted that the  
567 MBR estimate based on GNSS/GRACE combination from Argus et al. (2022) was derived as the  
568 difference between gravity and elastic loading-based annual GWS estimates to the output of a  
569 hydrological model not including MSR. The authors interpret this difference solely as MBR and  
570 neglect the contribution of MFR in the estimate, owing that the method they apply cannot  
571 discriminate between the two MSR processes. To reliably quantify MBR at the scale of the CV  
572 and discriminate it from MFR, we suggest the implementation of a fully fluid-solid media  
573 coupled 3D groundwater model for the CV that integrates the wealth of hydrologic and remote  
574 sensing observations sensitive to dynamics in the aquifers as demonstrated in this study. The  
575 results should also be crosschecked with observations of groundwater ages, e.g. based on isotope  
576 studies (Earman et al., 2006).

577 Our findings are subject to uncertainties, albeit statistical tests of significance help  
578 corroborate the main results. The wavelet time-frequency analysis is affected by data gaps and  
579 variable sampling rates, similar to other spectral methods (Goswami & Chan, 1999), although the  
580 ability of the continuous wavelet transforms to localize signal components in time and space  
581 minimizes error propagation. GNSS sites may be affected by other processes causing annual  
582 oscillations, such as non-tidal loading, tectonic processes, thermoelastic deformation, and  
583 draconitic errors (Chanard et al., 2020). Errors in the GWS component from GRACE  
584 observations are subject to any error in the correction terms, which directly maps into the GWS  
585 time series. However, the three months delay between the peak of GWS and GWL remains

586 robust against the uncertainty in the timing of GWS (see Section 4.2). Hence, the measure that  
587 pressure propagates faster to deep aquifer layers than the groundwater volume change in the  
588 entire aquifer remains unaffected.

589         Recent studies (Ajami et al., 2011; Markovich et al., 2019; Meixner et al., 2016; Somers  
590 & McKenzie, 2020; Wahi et al., 2008; Welch & Allen, 2014) have recognized mountains'  
591 critical role in freshwater supply to lowland dry basins, debunking the outdated notion that  
592 mountain groundwater storage and supply is negligible. In the Sierra Nevada aquifers,  
593 cosmogenic isotope studies linking snowmelt and annual aquifer recharge indicate a strong link  
594 between snowmelt and aquifer recharge and discharge in the mountains (Urióstegui et al., 2017).  
595 Additional evidence is provided by the increased age of groundwater contributing to the spring  
596 stream flow over the Sierra Nevada, consistent with increased temperature and reduced  
597 precipitation at high elevations (Manning et al., 2012). Thus, the high Sierra Nevada snowpack is  
598 essential for recharging mountain aquifers, which, in turn, contributes to the long-term recharge  
599 of deep, confined CV aquifers. Sierra Nevada runoff and MFR's role in freshwater supply in the  
600 CV is well-understood (Faunt, 2009; Meixner et al., 2016). However, the mountain block  
601 recharge process proposed here to replenish deep aquifers is not considered in the current  
602 hydrological models for the Valley, for example, by Faunt et al. (2009). Annual, interannual, and  
603 long-term changes in snowpack directly impact the MFR and MBR from the Sierra Nevada  
604 Mountains to the CV. Thus, the reliance on hydroclimate models that currently do not account  
605 for MBR limits the ability to accurately forecast the risk of climate extremes to California's  
606 groundwater supply and presents challenges for developing appropriate adaptation and resiliency  
607 strategies. The observation and analysis presented here have implications for the CV's recharge  
608 mechanism to deep aquifers. We call for new models that more comprehensively account for the  
609 Sierra Nevada Mountains' role in California's water cycle, which may also require a revision of  
610 current management and resiliency plans. Finally, we suggest the integration of pressure physics  
611 into methods quantifying seasonal storage changes in CV aquifers that apply well data and  
612 storage coefficients, or deformation data, given that well level and deformation changes at  
613 seasonal time scales are also driven by a change in pressure, not only in storage.

614

## 615 **Acknowledgments**

616         We thank anonymous reviewers and the editor for constructive comments and  
617 suggestions. This research was partly funded by the National Aeronautics and Space  
618 Administration grants NNX17AD98G (SW, MS, GC), 80NSSC21K0419 (SW, MS, GC) and  
619 80NSSC21K0061 (SW), as well as the Department of Energy grant DE-SC0019307 (MS).  
620

## 621 **Open Research**

622         All data used for this study are publicly available from the following sources. GRACE data were  
623 accessed from JPL PO.DAAC at [https://podaac.jpl.nasa.gov/dataset/TELLUS\\_GRAC-GRFO\\_MASCON\\_CRI\\_GRID\\_RL06\\_V2](https://podaac.jpl.nasa.gov/dataset/TELLUS_GRAC-GRFO_MASCON_CRI_GRID_RL06_V2). SNODAS data were downloaded from the National  
624 Snow & Ice Data Center (<https://nsidc.org/data/g02158>), GLDAS Noah, CLSM and VIC model  
625 outputs from the Goddard Earth Sciences Data and Information Services Center via  
626 [https://disc.gsfc.nasa.gov/datasets/GLDAS\\_NOAH025\\_M\\_2.1/summary?keywords=GLDAS](https://disc.gsfc.nasa.gov/datasets/GLDAS_NOAH025_M_2.1/summary?keywords=GLDAS),

628 [https://disc.gsfc.nasa.gov/datasets/GLDAS\\_CLSM10\\_M\\_2.1/summary?keywords=GLDAS](https://disc.gsfc.nasa.gov/datasets/GLDAS_CLSM10_M_2.1/summary?keywords=GLDAS), and  
 629 [https://disc.gsfc.nasa.gov/datasets/GLDAS\\_VIC10\\_M\\_2.1/summary?keywords=GLDAS](https://disc.gsfc.nasa.gov/datasets/GLDAS_VIC10_M_2.1/summary?keywords=GLDAS),  
 630 respectively. We kindly thank Hannes Müller Schmied (hannes.mueller.schmied@em.uni-  
 631 frankfurt.de) at the University of Frankfurt for providing WGHM version 2.2d outputs. GNSS  
 632 time series were downloaded from the Nevada Geodetic Laboratory  
 633 ([http://geodesy.unr.edu/gps\\_timeseries/tenv3/IGS14/](http://geodesy.unr.edu/gps_timeseries/tenv3/IGS14/)). The California Department of Water  
 634 Resources provided reservoir data ([https://cdec.water.ca.gov/dynamicapp/getAll?sens\\_num=15](https://cdec.water.ca.gov/dynamicapp/getAll?sens_num=15))  
 635 and groundwater level data, which we retrieved as bulk download from the California Natural  
 636 Resources Agency via the California Open Data Portal for “Periodic Groundwater Level  
 637 Measurements” (<https://data.ca.gov/dataset/periodic-groundwater-level-measurements>) and for  
 638 “Continuous Groundwater Level Measurements” ([https://data.ca.gov/dataset/continuous-](https://data.ca.gov/dataset/continuous-groundwater-level-measurements)  
 639 [groundwater-level-measurements](https://data.ca.gov/dataset/continuous-groundwater-level-measurements)). Further groundwater level data were retrieved from the  
 640 USGS archives for “Daily Data” ([https://waterdata.usgs.gov/ca/nwis/dv/?referred\\_module=gw](https://waterdata.usgs.gov/ca/nwis/dv/?referred_module=gw))  
 641 and “Field Measurements” (<https://nwis.waterdata.usgs.gov/ca/nwis/gwlevels>). Wavelet software  
 642 packages are provided by C. Torrence and G. Compo at URL:  
 643 <http://atoc.colorado.edu/research/wavelets>, as well as by Jon Erickson at URL:  
 644 [https://www.mathworks.com/matlabcentral/fileexchange/20821-continuous-wavelet-transform-](https://www.mathworks.com/matlabcentral/fileexchange/20821-continuous-wavelet-transform-and-inverse)  
 645 [and-inverse](https://www.mathworks.com/matlabcentral/fileexchange/20821-continuous-wavelet-transform-and-inverse). InSAR results, assembled groundwater records as well as all data analysis results  
 646 presented in the supporting information or figures will be made available upon acceptance  
 647 through a repository with the Virginia Tech Data Repository (<https://data.lib.vt.edu/>). During  
 648 peer review, all data analysis results are available in the supporting information, and/or figures.  
 649  
 650

## 651 References

- 652 Adusumilli, S., Borsa, A. A., Fish, M. A., McMillan, H. K., & Silverii, F. (2019). A decade of terrestrial water  
 653 storage changes across the contiguous United States from GPS and GRACE. *Geophysical Research Letters*,  
 654 2019GL085370. <https://doi.org/10.1029/2019GL085370>
- 655 Ajami, H., Troch, P. A., Maddock, T., Meixner, T., & Eastoe, C. (2011). Quantifying mountain block recharge by  
 656 means of catchment-scale storage-discharge relationships. *Water Resources Research*, 47(4).  
 657 <https://doi.org/10.1029/2010WR009598>
- 658 Alam, S., Gebremichael, M., Ban, Z., Scanlon, B. R., Senay, G., & Lettenmaier, D. P. (2021). Post-Drought  
 659 Groundwater Storage Recovery in California’s Central Valley. *Water Resources Research*, 57(10).  
 660 <https://doi.org/10.1029/2021WR030352>
- 661 Alley, W. M. (2002). Flow and Storage in Groundwater Systems. *Science*, 296(5575), 1985–1990.  
 662 <https://doi.org/10.1126/science.1067123>
- 663 Argus, D. F., Landerer, F. W., Wiese, D. N., Martens, H. R., Fu, Y., Famiglietti, J. S., Thomas, B. F., Farr, T. G.,  
 664 Moore, A. W., & Watkins, M. M. (2017). Sustained water loss in California’s mountain ranges during severe  
 665 drought from 2012 to 2015 inferred from GPS. *Journal of Geophysical Research: Solid Earth*, 122(12),  
 666 10,510–559,585. <https://doi.org/10.1002/2017JB014424>
- 667 Argus, D. F., Martens, H. R., Borsa, A. A., Knappe, E., Wiese, D. N., Alam, S., Anderson, M., Khatiwada, A., Lau,  
 668 N., Peidou, A., Swarr, M., White, A., Bos, M. S., Landerer, F. W., & Gardner, P. (2022). Subsurface water  
 669 flux in California’s Central Valley and its source watershed from space geodesy. *Geophysical Research*  
 670 *Letters*. <https://doi.org/10.1029/2022GL099583>
- 671 Ayres, A., Hanak, E., Gray, B., Sencan, G., Bruno, E., Bou, A. E., & Collins, J. (2021). *Improving California’s*  
 672 *Water Market*.
- 673 Bales, R. C., Hopmans, J. W., O’Geen, A. T., Meadows, M., Hartsough, P. C., Kirchner, P., Hunsaker, C. T., &  
 674 Beaudette, D. (2011). Soil Moisture Response to Snowmelt and Rainfall in a Sierra Nevada Mixed-Conifer  
 675 Forest. *Vadose Zone Journal*, 10(3), 786–799. <https://doi.org/10.2136/vzj2011.0001>

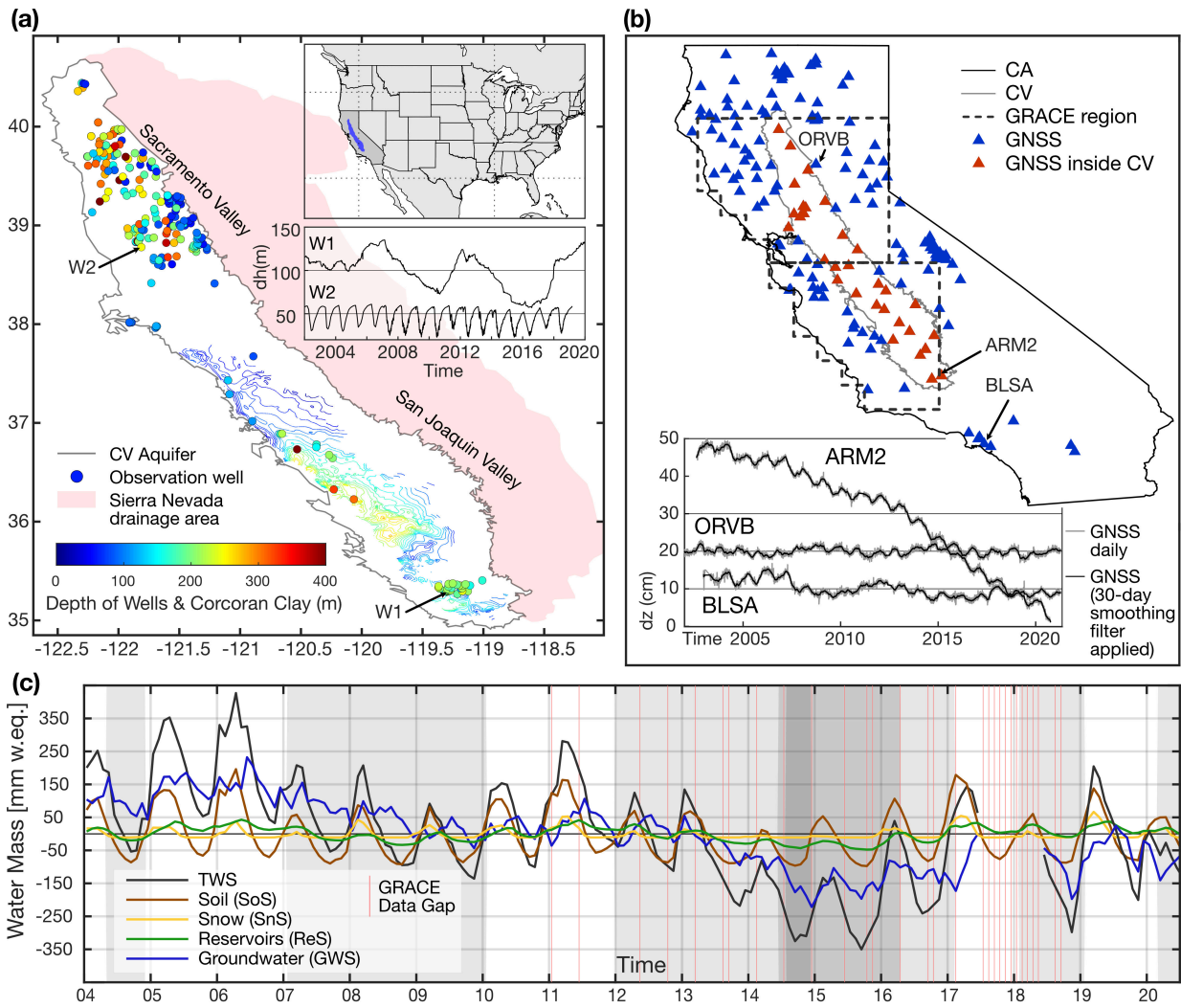
- 676 Beaudoin, H., & Rodell, M. (2016). GLDAS Noah Land Surface Model L4 monthly 0.25 x 0.25 degree V2.1,  
 677 NASA/GSFC/HSL: Greenbelt, Maryland, USA,. *Goddard Earth Sciences Data and Information Services*  
 678 *Center (GES DISC)*. <https://doi.org/10.5067/SXAVCZFAQLNO>
- 679 Berghuijs, W. R., Luijendijk, E., Moeck, C., van der Velde, Y., & Allen, S. T. (2022). Global Recharge Data Set  
 680 Indicates Strengthened Groundwater Connection to Surface Fluxes. *Geophysical Research Letters*, *49*(23).  
 681 <https://doi.org/10.1029/2022GL099010>
- 682 Borsa, A. A., Agnew, D. C., & Cayan, D. R. (2014). Ongoing drought-induced uplift in the western United States.  
 683 *Science*, *345*(6204), 1587–1590. <https://doi.org/10.1126/science.1260279>
- 684 Burow, K. R., Dubrovsky, N. M., & Shelton, J. L. (2007). Temporal trends in concentrations of DBCP and nitrate in  
 685 groundwater in the eastern San Joaquin Valley, California, USA. *Hydrogeology Journal*, *15*(5), 991–1007.  
 686 <https://doi.org/10.1007/s10040-006-0148-7>
- 687 Carlson, G., Shirzaei, M., Ojha, C., & Werth, S. (2020). Subsidence-Derived Volumetric Strain Models for Mapping  
 688 Extensional Fissures and Constraining Rock Mechanical Properties in the San Joaquin Valley, California.  
 689 *Journal of Geophysical Research: Solid Earth*. <https://doi.org/10.1029/2020JB019980>
- 690 Carlson, G., Shirzaei, M., Werth, S., Zhai, G., & Ojha, C. (2020). Seasonal and Long-Term Groundwater Unloading  
 691 in the Central Valley Modifies Crustal Stress. *Journal of Geophysical Research: Solid Earth*, *125*(1), 1–17.  
 692 <https://doi.org/10.1029/2019JB018490>
- 693 Carlson, G., Werth, S., & Shirzaei, M. (2022). Joint Inversion of GNSS and GRACE for Terrestrial Water Storage  
 694 Change in California. *Journal of Geophysical Research: Solid Earth*, *127*(3).  
 695 <https://doi.org/10.1029/2021JB023135>
- 696 CDWR. (2017). *California Department of Water Resources, California Data Exchange Center, Active Monthly*  
 697 *Reservoirs*. [http://cdec.water.ca.gov/misc/monthly\\_res.html](http://cdec.water.ca.gov/misc/monthly_res.html)
- 698 CDWR. (2019). *Continuous Groundwater Level Measurements*. <http://wdl.water.ca.gov/waterdatalibrary/>
- 699 Chanard, K., Métois, M., Rebischung, P., & Avouac, J. P. (2020). A warning against over-interpretation of seasonal  
 700 signals measured by the Global Navigation Satellite System. *Nature Communications*, *11*(1), 1–4.  
 701 <https://doi.org/10.1038/s41467-020-15100-7>
- 702 Costantini, M. (1998). A novel phase unwrapping method based on network programming. *IEEE Transactions on*  
 703 *Geoscience and Remote Sensing*, *36*(3), 813–821. <https://doi.org/10.1109/36.673674>
- 704 Earman, S., Campbell, A. R., Phillips, F. M., & Newman, B. D. (2006). Isotopic exchange between snow and  
 705 atmospheric water vapor: Estimation of the snowmelt component of groundwater recharge in the southwestern  
 706 United States. *Journal of Geophysical Research Atmospheres*, *111*(9). <https://doi.org/10.1029/2005JD006470>
- 707 Erickson, J. (2019). *Continuous wavelet transform and inverse* (Retrieved August 30, 2019.). MATLAB Central File  
 708 Exchange.
- 709 Escriva-Bou, A., Hui, R., Maples, S., Medellín-Azuara, J., Harter, T., & Lund, J. R. (2020). Planning for  
 710 groundwater sustainability accounting for uncertainty and costs: An application to California's Central Valley.  
 711 *Journal of Environmental Management*, *264*, 110426.
- 712 Escriva-Bou, A., Sencan, G., & Hanak, E. (2021). *Groundwater Recharge, Fact Sheet August 2021*.
- 713 Famiglietti, J. S., Lo, M., Ho, S. L., Bethune, J., Anderson, K. J., Syed, T. H., Swenson, S. C., de Linage, C. R., &  
 714 Rodell, M. (2011). Satellites measure recent rates of groundwater depletion in California's Central Valley.  
 715 *Geophysical Research Letters*, *38*(3). <https://doi.org/10.1029/2010GL046442>
- 716 Farr, T. G., Rosen, P. A., Caro, E., Crippen, R., Duren, R., Hensley, S., Kobrick, M., Paller, M., Rodriguez, E.,  
 717 Roth, L., Seal, D., Shaffer, S., Shimada, J., Umland, J., Werner, M., Oskin, M., Burbank, D., & Alsdorf, D.  
 718 (2007). The Shuttle Radar Topography Mission. *Reviews of Geophysics*, *45*(2), RG2004.  
 719 <https://doi.org/10.1029/2005RG000183>
- 720 Faunt, C. C. (2009). *Groundwater Availability of the Central Valley Aquifer, California* (C. C. Faunt, Ed.). U.S.  
 721 Geological Survey Professional Paper 1766. <https://pubs.usgs.gov/pp/1766/>
- 722 Faunt, C. C., Sneed, M., Traum, J., & Brandt, J. T. (2016). Water availability and land subsidence in the Central  
 723 Valley, California, USA. *Hydrogeology Journal*, *24*(3), 675–684. <https://doi.org/10.1007/s10040-015-1339-x>
- 724 Feth, J. H. (1964). Hidden Recharge. *Groundwater*, *2*(4), 14–17. [https://doi.org/10.1111/j.1745-](https://doi.org/10.1111/j.1745-6584.1964.tb01780.x)  
 725 [6584.1964.tb01780.x](https://doi.org/10.1111/j.1745-6584.1964.tb01780.x)
- 726 Fetter, C. W., & Kremer, D. (2022). *Applied Hydrogeology* (5th ed.). Waveland Press.
- 727 Fox-Kemper, B., Hewitt, H. T., Xiao, C., Aðalgeirsdóttir, G., Drijfhout, S. S., Edwards, T. L., Golledge, N. R.,  
 728 Hemer, M., Kopp, R. E., Krinner, G., Mix, A., Notz, D., Nowicki, S., Nurhati, I. S., Ruiz, L., Sallée, J.-B.,  
 729 Slangen, A. B. A., & Yu, Y. (2021). Ocean, Cryosphere and Sea Level Change. In *Climate Change 2021: The*  
 730 *Physical Science Basis. Contribution of Working Group I to the Sixth Assessment Report of the*  
 731 *Intergovernmental Panel on Climate Change [MassonDelmotte, V., P. Zhai, A. Pirani, S. L. Connors, C.*

- 732 Péan, S. Berger, N. Caud, Y. Chen., Cambridge University Press, Cambridge, United Kingdom and New  
 733 York, NY, USA, 2391 pp. doi:10.1017/9781009157896.  
 734 [https://report.ipcc.ch/ar6/wg1/IPCC\\_AR6\\_WGI\\_FullReport.pdf](https://report.ipcc.ch/ar6/wg1/IPCC_AR6_WGI_FullReport.pdf).
- 735 Franceschetti, G., & Lanari, R. (1999). *Synthetic aperture radar processing*. CRC Press.
- 736 Galloway, D. L., Jones, D. R., & Ingebritsen, S. E. (1999). *Land subsidence in the United States*. U.S. Geological  
 737 Survey Circular 1182. <https://doi.org/10.3133/cir1182>
- 738 Gao, S. S., Silver, P. G., Linde, A. T., & Sacks, I. S. (2000). Annual modulation of triggered seismicity following  
 739 the 1992 Landers earthquake in California. *Nature*, 406(6795), 500–504. <https://doi.org/10.1038/35020045>
- 740 Ghasemzade, M., Asante, K. O., Petersen, C., Kocis, T., Dahlke, H. E., & Harter, T. (2019). An Integrated  
 741 Approach Toward Sustainability via Groundwater Banking in the Southern Central Valley, California. *Water*  
 742 *Resources Research*, 55(4), 2742–2759. <https://doi.org/10.1029/2018WR024069>
- 743 Gilbert, J. M., & Maxwell, R. M. (2017). Examining regional groundwater-surface water dynamics using an  
 744 integrated hydrologic model of the San Joaquin River basin. *Hydrology and Earth System Sciences*, 21(2),  
 745 923–947. <https://doi.org/10.5194/hess-21-923-2017>
- 746 Goswami, J. C., & Chan, A. K. (1999). *Fundamentals of Wavelets: Theory, Algorithms, and Applications*. Wiley-  
 747 Interscience.
- 748 Hanak, E., Lund, J., Arnold, B., Escriva-Bou, A., Gray, B., Green, S., Harter, T., Howitt, R., MacEwan, D., &  
 749 Medellín-Azuara, J. (2017). *Water Stress and a Changing San Joaquin Valley*. Public Policy Institute of  
 750 California.
- 751 Hanson, R. T., Flint, L. E., Flint, A. L., Dettinger, M. D., Faunt, C. C., Cayan, D., & Schmid, W. (2012). A method  
 752 for physically based model analysis of conjunctive use in response to potential climate changes. *Water*  
 753 *Resources Research*, 48(2). <https://doi.org/10.1029/2011WR010774>
- 754 Harpold, A., Dettinger, M., & Rajagopal, S. (2017). Defining Snow Drought and Why It Matters. *Eos*.  
 755 <https://doi.org/10.1029/2017EO068775>
- 756 Hatchett, B. J., & McEvoy, D. J. (2018). Exploring the origins of snow drought in the northern sierra nevada,  
 757 california. *Earth Interactions*, 22(2), 1–13. <https://doi.org/10.1175/EI-D-17-0027.1>
- 758 Healy, R. W., & Scanlon, B. R. (2010). *Estimating Groundwater Recharge*. Cambridge University Press.
- 759 Huth, A. K., Leydecker, A., Sickman, J. O., & Bales, R. C. (2004). A two-component hydrograph separation for  
 760 three high-elevation catchments in the Sierra Nevada, California. *Hydrological Processes*, 18(9), 1721–1733.  
 761 <https://doi.org/10.1002/hyp.1414>
- 762 Jódar, J., Cabrera, J. A., Martos-Rosillo, S., Ruiz-Constán, A., González-Ramón, A., Lambán, L. J., Herrera, C., &  
 763 Custodio, E. (2017). Groundwater discharge in high-mountain watersheds: A valuable resource for  
 764 downstream semi-arid zones. The case of the Bérchules River in Sierra Nevada (Southern Spain). *Science of*  
 765 *The Total Environment*, 593–594, 760–772. <https://doi.org/10.1016/j.scitotenv.2017.03.190>
- 766 Johnson, C. W., Fu, Y., & Bürgmann, R. (2017). Seasonal water storage, stress modulation, and California  
 767 seismicity. *Science*, 356(6343), 1161–1164. <https://doi.org/10.1126/science.aak9547>
- 768 Konikow, L. F. (2015). Long-Term Groundwater Depletion in the United States. *Groundwater*, 53(1), 2–9.  
 769 <https://doi.org/10.1111/gwat.12306>
- 770 Lee, J. C., & Shirzaei, M. (2023). Novel algorithms for pair and pixel selection and atmospheric error correction in  
 771 multitemporal InSAR. *Remote Sensing of Environment*, 286. <https://doi.org/10.1016/j.rse.2022.113447>
- 772 Li, R., Ou, G., Pun, M., & Larson, L. (2018). Evaluation of Groundwater Resources in Response to Agricultural  
 773 Management Scenarios in the Central Valley, California. *Journal of Water Resources Planning and*  
 774 *Management*, 144(12), 04018078. [https://doi.org/10.1061/\(asce\)wr.1943-5452.0001014](https://doi.org/10.1061/(asce)wr.1943-5452.0001014)
- 775 Liu, F., Conklin, M. H., & Shaw, G. D. (2017). Insights into hydrologic and hydrochemical processes based on  
 776 concentration-discharge and end-member mixing analyses in the mid-Merced River Basin, Sierra Nevada,  
 777 California. *Water Resources Research*, 53(1), 832–850. <https://doi.org/10.1002/2016WR019437>
- 778 Manning, A. H., Clark, J. F., Diaz, S. H., Rademacher, L. K., Earman, S., & Niel Plummer, L. (2012). Evolution of  
 779 groundwater age in a mountain watershed over a period of thirteen years. *Journal of Hydrology*, 460–461, 13–  
 780 28. <https://doi.org/10.1016/j.jhydrol.2012.06.030>
- 781 Markovich, K. H., Manning, A. H., Condon, L. E., & McIntosh, J. C. (2019). Mountain-Block Recharge: A Review  
 782 of Current Understanding. *Water Resources Research*, 55(11), 8278–8304.  
 783 <https://doi.org/10.1029/2019WR025676>
- 784 Massoud, E. C., Purdy, A. J., Miro, M. E., & Famiglietti, J. S. (2018). Projecting groundwater storage changes in  
 785 California's Central Valley. *Scientific Reports*, 8(1), 12917. <https://doi.org/10.1038/s41598-018-31210-1>

- 786 McCabe, G. J., Palecki, M. A., & Betancourt, J. L. (2004). Pacific and Atlantic Ocean influences on multidecadal  
787 drought frequency in the United States. *Proceedings of the National Academy of Sciences*, *101*(12), 4136–  
788 4141. <https://doi.org/10.1073/pnas.0306738101>
- 789 McMahon, P. B., Plummer, L. N., Böhlke, J. K., Shapiro, S. D., & Hinkle, S. R. (2011). A comparison of recharge  
790 rates in aquifers of the United States based on groundwater-age data. *Hydrogeology Journal*, *19*(4), 779–800.  
791 <https://doi.org/10.1007/s10040-011-0722-5>
- 792 Meixner, T., Manning, A. H., Stonestrom, D. A., Allen, D. M., Ajami, H., Blasch, K. W., Brookfield, A. E., Castro,  
793 C. L., Clark, J. F., & Gochis, D. J. (2016). Implications of projected climate change for groundwater recharge  
794 in the western United States. *Journal of Hydrology*, *534*, 124–138.
- 795 Meyer, P. L. (1970). *Introductory Probability and Statistical Applications* (2nd ed.). Oxford & IBH Publishing Co.
- 796 Montgomery-Brown, E. K., Shelly, D. R., & Hsieh, P. A. (2019). Snowmelt-Triggered Earthquake Swarms at the  
797 Margin of Long Valley Caldera, California. *Geophysical Research Letters*, *46*(7), 3698–3705.  
798 <https://doi.org/10.1029/2019GL082254>
- 799 Mote, P. W., Li, S., Lettenmaier, D. P., Xiao, M., & Engel, R. (2018). Dramatic declines in snowpack in the western  
800 US. *Npj Climate and Atmospheric Science*, *1*(1). <https://doi.org/10.1038/s41612-018-0012-1>
- 801 Murray, K. D., & Lohman, R. B. (2018). Short-lived pause in Central California subsidence after heavy winter  
802 precipitation of 2017. *Science Advances*, *4*(8), eaar8144. <https://doi.org/10.1126/sciadv.aar8144>
- 803 Neely, W. R., Borsa, A. A., Burney, J. A., Levy, M. C., Silverii, F., & Sneed, M. (2021). Characterization of  
804 Groundwater Recharge and Flow in California's San Joaquin Valley From InSAR-Observed Surface  
805 Deformation. *Water Resources Research*, *57*(4), 1–20. <https://doi.org/10.1029/2020wr028451>
- 806 NOHRSC. (2004). *National Operational Hydrologic Remote Sensing Center, Snow Data Assimilation System*  
807 *(SNODAS) data products at NSIDC, Version 1*. National Snow and Ice Data Center, Boulder, CO, USA.  
808 <https://doi.org/10.7265/N5TB14TC>
- 809 Ojha, C., Shirzaei, M., Werth, S., Argus, D. F., & Farr, T. G. (2018). Sustained Groundwater Loss in California's  
810 Central Valley Exacerbated by Intense Drought Periods. *Water Resources Research*, *54*(7), 4449–4460.  
811 <https://doi.org/10.1029/2017WR022250>
- 812 Ojha, C., Werth, S., & Shirzaei, M. (2019). Groundwater Loss and Aquifer System Compaction in San Joaquin  
813 Valley During 2012–2015 Drought. *Journal of Geophysical Research: Solid Earth*, *124*(3), 3127–3143.  
814 <https://doi.org/10.1029/2018JB016083>
- 815 Pepin, N., Bradley, R. S., Diaz, H. F., Baraer, M., Caceres, E. B., Forsythe, N., Fowler, H., Greenwood, G., Hashmi,  
816 M. Z., Liu, X. D., Miller, J. R., Ning, L., Ohmura, A., Palazzi, E., Rangwala, I., Schöner, W., Severskiy, I.,  
817 Shahgedanova, M., Wang, M. B., ... Yang, D. Q. (2015). Elevation-dependent warming in mountain regions  
818 of the world. *Nature Climate Change*, *5*(5), 424–430. <https://doi.org/10.1038/nclimate2563>
- 819 Peterson, D., Smith, R., Stewart, I., Knowles, N., Soulard, C., Hager, S., & Norton, G. A. (2003). *Snowmelt*  
820 *Discharge Characteristics, Sierra Nevada, California*. (Series Name SIR - 2005-5056). U.S. Geological  
821 Survey.
- 822 Quiring, S. M., & Goodrich, G. B. (2008). Nature and causes of the 2002 to 2004 drought in the southwestern  
823 United States compared with the historic 1953 to 1957 drought. *Climate Research*, *36*(1), 41–52.  
824 <https://doi.org/10.3354/cr00735>
- 825 Rodell, M., Houser, P. R., Jambor, U., Gottschalk, J., Mitchell, K., Meng, C.-J., Arsenault, K., Cosgrove, B.,  
826 Radakovich, J., Bosilovich, M., Entin\*, J. K., Walker, J. P., Lohmann, D., & Toll, D. (2004). The Global Land  
827 Data Assimilation System. *Bulletin of the American Meteorological Society*, *85*(3), 381–394.  
828 <https://doi.org/10.1175/BAMS-85-3-381>
- 829 Saar, M. O., & Manga, M. (2003). Seismicity induced by seasonal groundwater recharge at Mt. Hood, Oregon.  
830 *Earth and Planetary Science Letters*, *214*(3–4), 605–618. [https://doi.org/10.1016/S0012-821X\(03\)00418-7](https://doi.org/10.1016/S0012-821X(03)00418-7)
- 831 Scanlon, B. R., Longuevergne, L., & Long, D. (2012). Ground referencing GRACE satellite estimates of  
832 groundwater storage changes in the California Central Valley, USA. *Water Resources Research*, *48*(4),  
833 W04520. <https://doi.org/10.1029/2011WR011312>
- 834 Schmidt, R., Flechtner, F., Meyer, U., Neumayer, K.-H., Dahle, C., König, R., & Kusche, J. (2008). Hydrological  
835 Signals Observed by the GRACE Satellites. *Surveys in Geophysics*, *29*(4–5), 319–334.  
836 <https://doi.org/10.1007/s10712-008-9033-3>
- 837 Schreiner-McGraw, A. P., & Ajami, H. (2022). Combined impacts of uncertainty in precipitation and air  
838 temperature on simulated mountain system recharge from an integrated hydrologic model. *Hydrology and*  
839 *Earth System Sciences*, *26*(4), 1145–1164. <https://doi.org/10.5194/hess-26-1145-2022>
- 840 Shirzaei, M. (2013). A Wavelet-Based Multitemporal DInSAR Algorithm for Monitoring Ground Surface Motion.  
841 *Ieee Geoscience and Remote Sensing Letters*, *10*(3), 456–460. <https://doi.org/10.1109/Lgrs.2012.2208935>

- 842 Shirzaei, M., Bürgmann, R., & Fielding, E. J. (2017). Applicability of Sentinel-1 Terrain Observation by Progressive  
843 Scans multitemporal interferometry for monitoring slow ground motions in the San Francisco Bay Area.  
844 *Geophysical Research Letters*, *44*(6), 2733–2742. <https://doi.org/10.1002/2017GL072663>.
- 845 Shirzaei, M., Bürgmann, R., Foster, J., Walter, T. R., & Brooks, B. A. (2013). Aseismic deformation across the  
846 Hilina fault system, Hawaii, revealed by wavelet analysis of InSAR and GPS time series. *Earth and Planetary  
847 Science Letters*, *376*, 12–19. <https://doi.org/10.1016/j.epsl.2013.06.011>
- 848 Shirzaei, M., Ojha, C., Werth, S., Carlson, G., & Vivoni, E. R. (2019). Comment on “Short-lived pause in Central  
849 California subsidence after heavy winter precipitation of 2017” by K. D. Murray and R. B. Lohman. *Science  
850 Advances*, *5*(eaav8038). <https://doi.org/10.1126/sciadv.aav8038>
- 851 Siebert, S., Burke, J., Faures, J. M., Frenken, K., Hoogeveen, J., Döll, P., & Portmann, F. T. (2010). Groundwater  
852 use for irrigation - A global inventory. *Hydrology and Earth System Sciences*, *14*(10), 1863–1880.  
853 <https://doi.org/10.5194/hess-14-1863-2010>
- 854 Smith, R. G., Knight, R., Chen, J., Reeves, J. A., Zebker, H. A., Farr, T., & Liu, Z. (2017). Estimating the permanent  
855 loss of groundwater storage in the southern San Joaquin Valley, California. *Water Resources Research*, *53*(3),  
856 2133–2148. <https://doi.org/10.1002/2016WR019861>
- 857 Somers, L. D., & McKenzie, J. M. (2020). A review of groundwater in high mountain environments. *Wiley  
858 Interdisciplinary Reviews: Water*, *7*(6), 1–27. <https://doi.org/10.1002/wat2.1475>
- 859 Stevenson, S., Coats, S., Touma, D., Cole, J., Lehner, F., Fasullo, J., & Otto-Bliesner, B. (2022). Twenty-first  
860 century hydroclimate: A continually changing baseline, with more frequent extremes. *Proceedings of the  
861 National Academy of Sciences*, *119*(12). <https://doi.org/10.1073/pnas.2108124119>
- 862 Tague, C., & Grant, G. E. (2009). Groundwater dynamics mediate low-flow response to global warming in snow-  
863 dominated alpine regions. *Water Resources Research*, *45*(7). <https://doi.org/10.1029/2008WR007179>
- 864 Tague, C., Grant, G., Farrell, M., Choate, J., & Jefferson, A. (2008). Deep groundwater mediates streamflow  
865 response to climate warming in the Oregon Cascades. *Climatic Change*, *86*(1–2), 189–210.  
866 <https://doi.org/10.1007/s10584-007-9294-8>
- 867 Talwani, P., & Acree, S. (1985). Pore pressure diffusion and the mechanism of reservoir-induced seismicity. In  
868 *Earthquake prediction* (pp. 947–965). Springer.
- 869 Tang, Q., & Oki, T. (Eds.). (2016). *Terrestrial Water Cycle and Climate Change*. John Wiley & Sons, Inc.  
870 <https://doi.org/10.1002/9781118971772>
- 871 Tapley, B. D., Bettadpur, S., Ries, J. C., Thompson, P. F., & Watkins, M. M. (2004). GRACE measurements of  
872 mass variability in the Earth system. *Science*, *305*(5683), 503–505. <https://doi.org/10.1126/science.1099192>
- 873 Tapley, B. D., Watkins, M. M., Flechtner, F., Reigber, C., Bettadpur, S., Rodell, M., Sasgen, I., Famiglietti, J. S.,  
874 Landerer, F. W., Chambers, D. P., Reager, J. T., Gardner, A. S., Save, H., Ivins, E. R., Swenson, S. C.,  
875 Boening, C., Dahle, C., Wiese, D. N., Dobslaw, H., ... Velicogna, I. (2019). Contributions of GRACE to  
876 understanding climate change. *Nature Climate Change*, *9*(5), 358–369. <https://doi.org/10.1038/s41558-019-0456-2>
- 877
- 878 Torrence, C., & Compo, G. P. (1998). A practical guide to wavelet analysis. In *Bulletin of the American  
879 Meteorological Society* (Retrieved December 5, 2018.; Vol. 79, Issue 1, pp. 61–78).  
880 [https://doi.org/10.1175/1520-0477\(1998\)079<0061:APGTWA>2.0.CO;2](https://doi.org/10.1175/1520-0477(1998)079<0061:APGTWA>2.0.CO;2)
- 881 Urióstegui, S. H., Bibby, R. K., Esser, B. K., & Clark, J. F. (2017). Quantifying annual groundwater recharge and  
882 storage in the central Sierra Nevada using naturally occurring <sup>35</sup>S. *Hydrological Processes*, *31*(6), 1382–  
883 1397. <https://doi.org/10.1002/hyp.11112>
- 884 USGS. (2021). *USGS Groundwater Data for the Nation*. <https://waterdata.usgs.gov/nwis/gw>
- 885 Vasco, D. W., Kim, K., Farr, T. G., Reager, J. T., Bekaert, D., Singh, S., & Beaudoin, H. K. (2022). Using  
886 Sentinel-1 and GRACE satellite data to monitor the long- and short-term hydrological variations within the  
887 Tulare Basin, California. *Scientific Reports*, 1–14. <https://doi.org/10.1038/s41598-022-07650-1>
- 888 Vrugt, J. A., Dekker, S. C., & Bouten, W. (2003). Identification of rainfall interception model parameters from  
889 measurements of throughfall and forest canopy storage. *Water Resources Research*, *39*(9).  
890 <https://doi.org/10.1029/2003WR002013>
- 891 Wahi, A. K., Hogan, J. F., Ekwurzel, B., Baillie, M. N., & Eastoe, C. J. (2008). Geochemical Quantification of  
892 Semiarid Mountain Recharge. *Ground Water*, *46*(3), 414–425. <https://doi.org/10.1111/j.1745-6584.2007.00413.x>
- 893
- 894 Wang, H. F. (2000). *Theory of Linear Poroelasticity with Applications to Geomechanics and Hydrogeology*.  
895 Princeton Univ. Press.

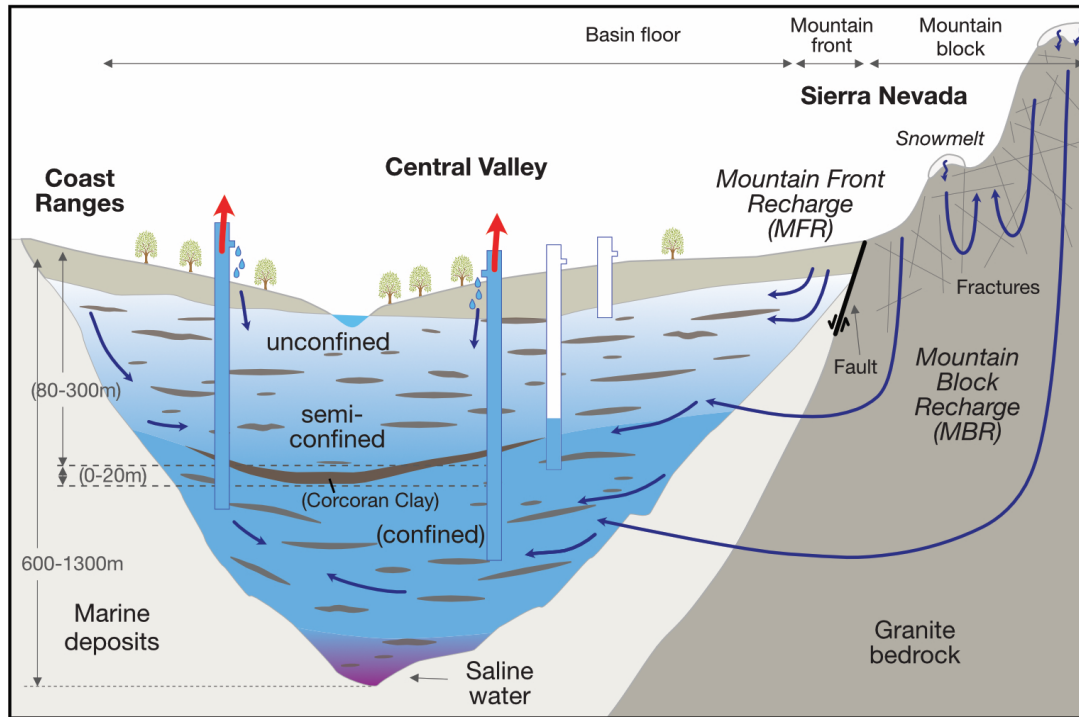
- 896 Welch, L. A., & Allen, D. M. (2014). Hydraulic conductivity characteristics in mountains and implications for  
897 conceptualizing bedrock groundwater flow. *Hydrogeology Journal*, 22(5), 1003–1026.  
898 <https://doi.org/10.1007/s10040-014-1121-5>
- 899 Werner, C., U. Wegmüller, T. Strozzi, & A. Wiesmann. (2000). Gamma SAR and interferometric processing  
900 software. *Proceedings of the Ers-Envisat Symposium, Gothenburg, Sweden.*
- 901 White, A. M., Gardner, W. P., Borsa, A. A., Argus, D. F., & Martens, H. R. (2022). A review of GNSS/GPS in  
902 hydrogeodesy: Hydrologic loading applications and their implications for water resource research. *Water*  
903 *Resources Research*. <https://doi.org/10.1029/2022WR032078>
- 904 Yin, D., & Roderick, M. L. (2020). Inter-annual variability of the global terrestrial water cycle. *Hydrology and*  
905 *Earth System Sciences*, 24(1), 381–396. <https://doi.org/10.5194/hess-24-381-2020>
- 906 Zektser, I. S., & Everett, L. G. (2004). *Groundwater Resources of the World and Their Use* (IHP-VI Series on  
907 Groundwater No. 6). United Nations Educational, Scientific and Cultural Organization (UNESCO).  
908  
909



910

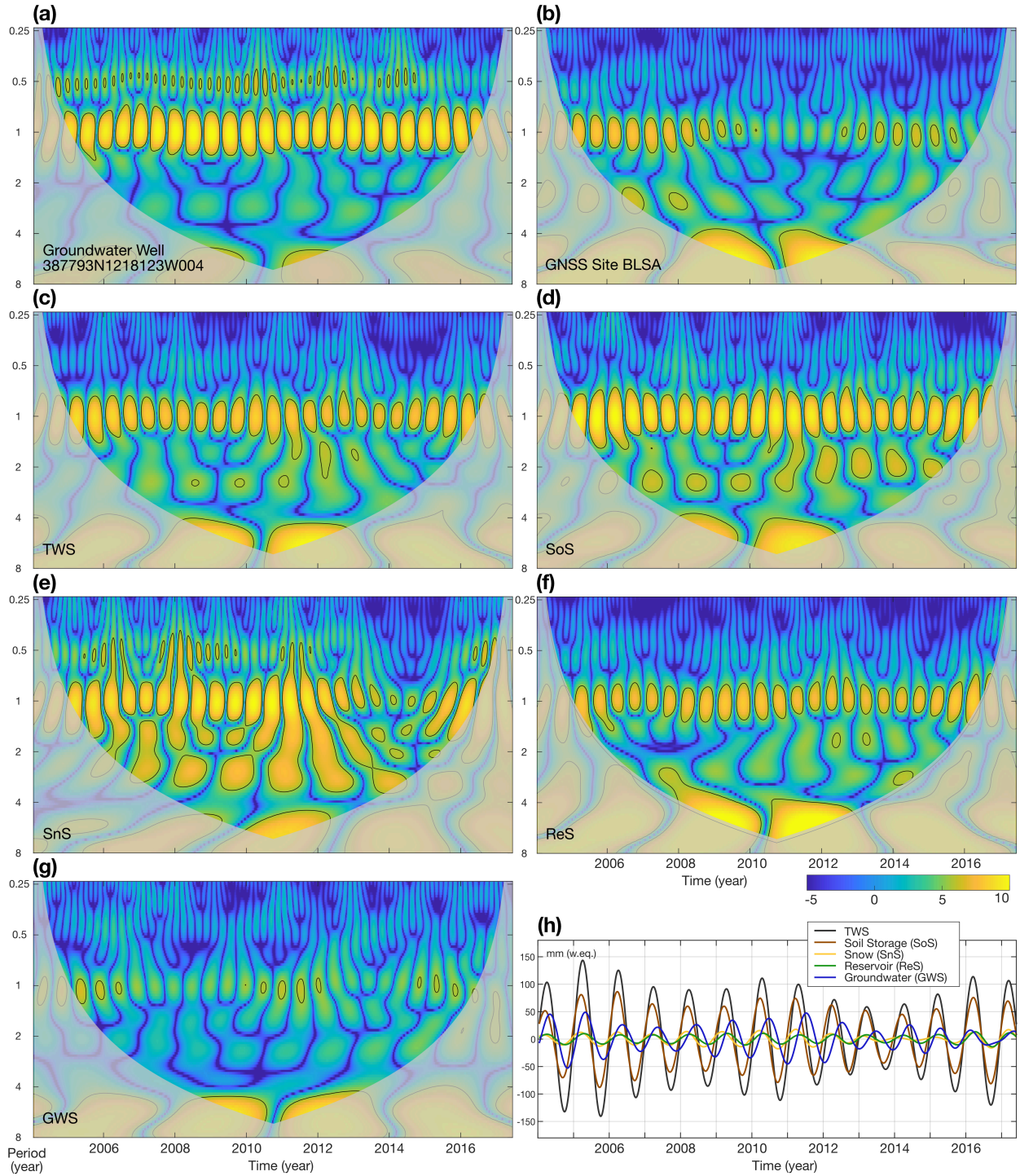
911 **Figure 1.** Overview of study area and data sets applied in this study. **(a)** Study area and  
 912 hydrogeological datasets: Outline of the Central Valley aquifer system (grey line,  $A_{CV} = 53,672$   
 913 km<sup>2</sup>), Sierra Nevada drainage area (red shade,  $A_{SN} = 63,780$  km<sup>2</sup>), location and depth of  
 914 observation wells that provide measurements at depth of 50 m and deeper, and lateral coverage  
 915 and depth of the confining Corcoran clay layer (source USGS:  
 916 [https://water.usgs.gov/GIS/metadata/usgswrd/XML/pp1766\\_corcoran\\_clay\\_depth\\_feet.xml](https://water.usgs.gov/GIS/metadata/usgswrd/XML/pp1766_corcoran_clay_depth_feet.xml)). See  
 917 Figure S4e and S4f for histograms of well depths. Top inset indicates location of the study area  
 918 over contiguous US. Bottom inset shows time series of two selected well sites W1  
 919 (#352958N1193011W001) and W2 (#387793N1218123W004). **(b)** Geodetic data sets: Mass  
 920 change regions of JPL GRACE mascon solutions (black dashed line) and location of GNSS sites  
 921 from the University of Reno, Nevada (red and blue triangles). Red triangles mark stations located  
 922 inside the Central Valley (CV), and blue triangles those outside the CV aquifer boundary. **(c)**  
 923 Time series of TWS from GRACE, composite hydrological storages and estimated GW storage  
 924 are averaged for the GRACE region shown in panel a, after Ojha et al. [2019]. Gray shaded  
 925 background areas (light, medium, dark gray) indicate that the USDM identifies >30% (>30%,  
 926 >60%) of California's area to be in moderate (exceptional, exceptional) dry condition (compare  
 927 Fig. S3).

928



929

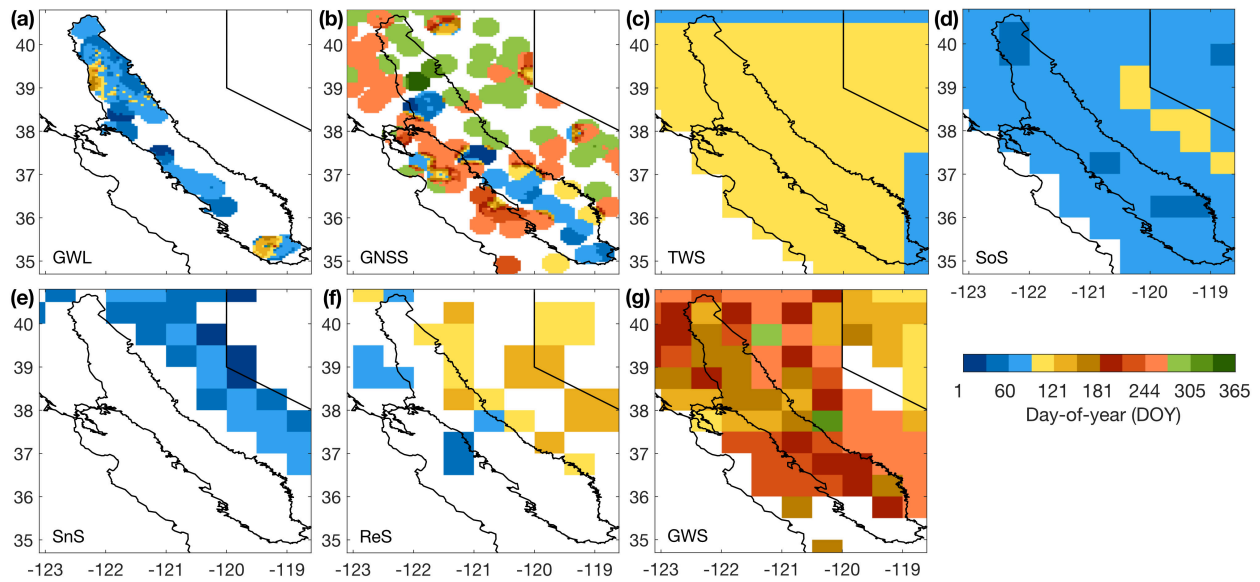
930 **Figure 2.** Conceptual and process-based model of pressure propagation and recharge in the  
 931 Sierra Nevada to deep aquifer layers of the Central Valley. **(a)** Hydrogeological setting in the  
 932 Central Valley (~400 m a.s.l.) and Sierra Nevada Mountains (up to ~4000 m a.s.l.). Indicated are  
 933 major groundwater fluxes in and out from deep aquifer layers, including mountain front and  
 934 mountain block recharge (MFR and MBR). Confining unit of the Corcoran clay is only present  
 935 in the southern San Joaquin Valley, where pumping is more intense compared to the northern  
 936 Sacramento Valley (Fig. 1a). This graph is inspired by Faunt et al. (2009) (Fig. A9 therein),  
 937 Smith et al. (2017) (Fig. 2 therein) as well as Somers and McKenzie (2020) (Fig. 5 therein).  
 938



939

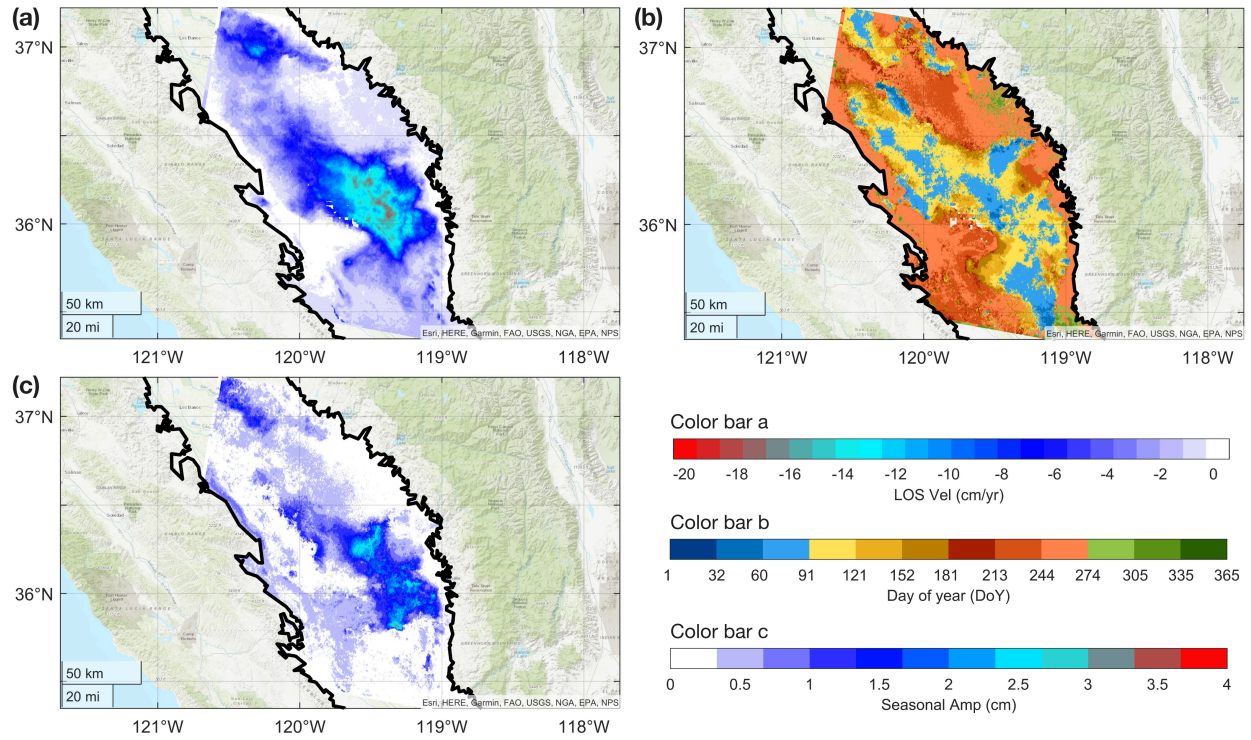
940 **Figure 3.** Wavelet time-frequency analysis. A wavelet analysis was performed for time series of  
 941 all available datasets to isolate the annual signal component. Wavelet spectrum of time series of  
 942 (a) groundwater level at well 387793N1218123W004 and (b) vertical land motion at GNSS site  
 943 BLSA (see Fig. 1 for their location), and of average water storage variations in the GRACE  
 944 region: (c) total water storage (TWS) from GRACE, (d) soil storage (SoS) from GLDAS and  
 945 WGFM, (e) snow storage (SnS) from SNODAS, (f) reservoir storage (ReS) from CDWR and (g)

946 groundwater storage (GWS) in CV. **(h)** Reconstructed annual signal component for periods  
 947 within range of 0.75-0.25 years from water storage wavelet spectra shown in panel c-g.



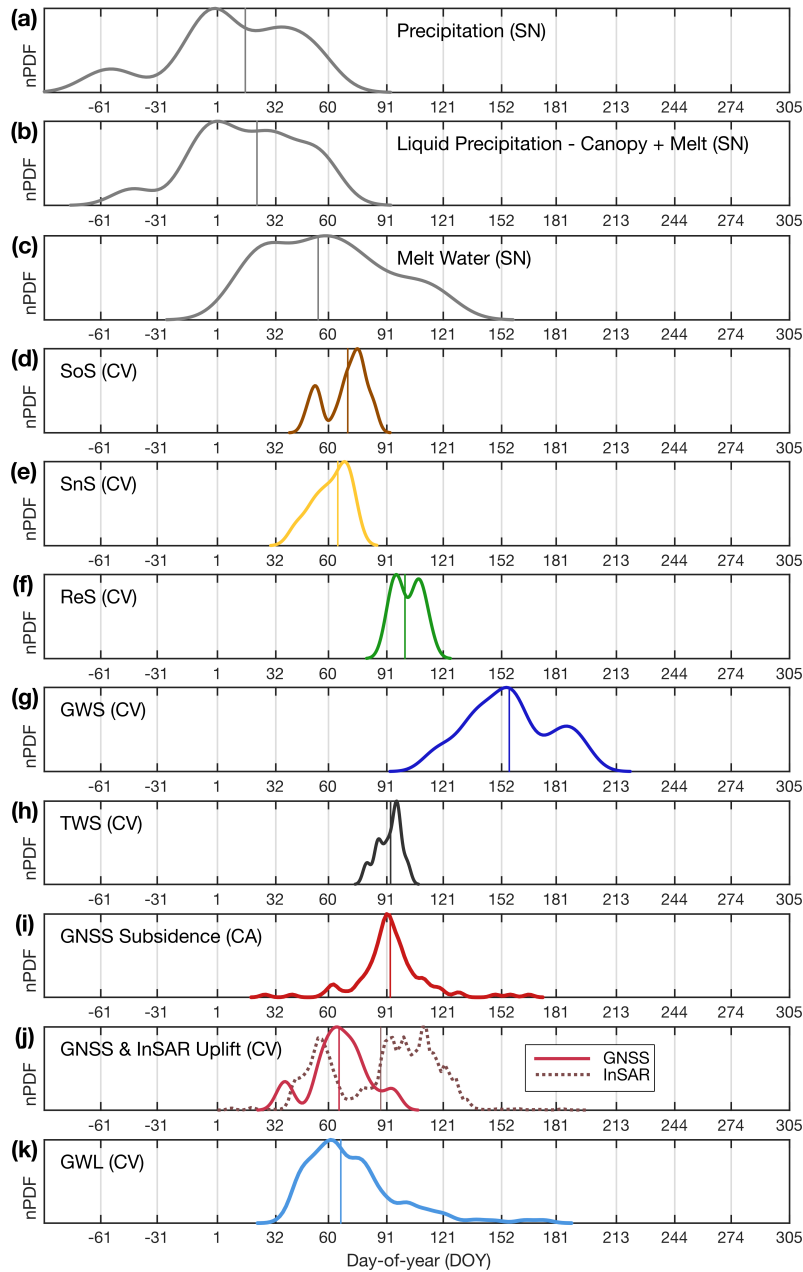
948

949 **Figure 4.** Timing of annual maximum of groundwater related signals. Timings are given in day-  
 950 of-year (DOY). (a) Groundwater levels (GWL) at 250 observation sites throughout the Central  
 951 Valley providing at least three years of data during 2002-2020 at depths below 50 m. (b) Vertical  
 952 land motion (maximum uplift) at 170 GNSS sites throughout entire California with a seasonal  
 953 amplitude larger than the median of the time series error standard deviation. Timing for  
 954 groundwater and GNSS were inversely interpolated using a 25 km correlation radius. Remaining  
 955 panels show timing of annual maximum water storage at 0.5-degree sampling resolution: (c) total  
 956 water storage (TWS) from GRACE, (d) soil storage (SoS) from GLDAS-Noah, (e) snow storage  
 957 (SnS) from SNODAS, (f) reservoir storage (ReS) from CDWR and (g) resulting groundwater  
 958 storage (GWS). White areas have either no data or amplitude of annual variation is near zero.  
 959 Annual oscillations of vertical land motion inside the CV are temporally aligned with those of  
 960 groundwater level variations. In contrast, oscillations of vertical land motion outside the Central  
 961 Valley are in resonance with annual oscillations of total water storage changes detected by  
 962 GRACE (compare panel b with c, and Fig. 6), because maximum VLM outside the Valley is  
 963 driven by minimum elastic load of the water masses. Individual values for groundwater well and  
 964 GNSS sites, timing of minima, related histograms, and standard deviations of annual timing  
 965 during observation periods are shown in Figures S8, S9, S10, and S11.



966

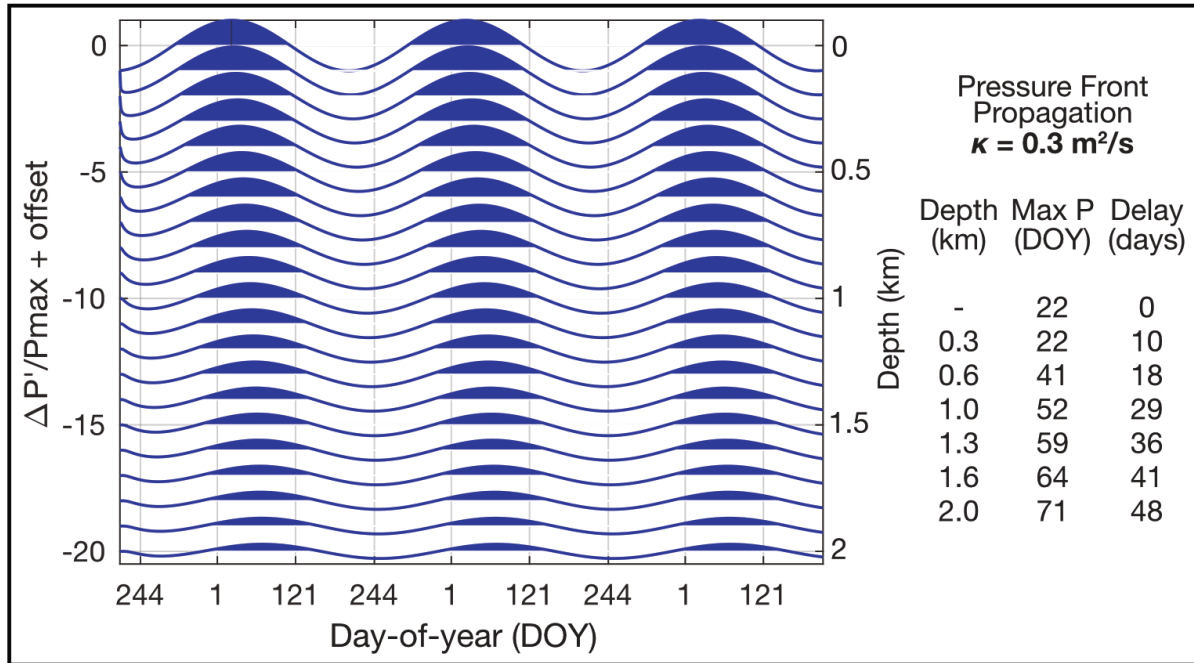
967 **Figure 5.** a) LOS velocity map for period 2015/11/27-2022/12/20. b) Median seasonal phase  
 968 (peak DOY), and (c) amplitude of InSAR deformation time series for water years 2016-2022.  
 969 See Figs. S15 and S16 for yearly phase and amplitude maps, respectively.  
 970



971

972 **Figure 6.** Normalized probability density functions for timing of annual extremes in  
 973 groundwater-related signals across California. Row and line color indicate signal type: **(a)** total  
 974 precipitation in the recharge area of the Sierra Nevada (SN, see Fig. 1a) from SNODAS, **(b)** Sum  
 975 of liquid precipitation and melt water corrected for canopy interception in SN from SNODAS,  
 976 **(c)** Melt water in SN from SNODAS, **(d)** soil storage from hydrological models for GRACE  
 977 region corresponding with the Central Valley (CV, Fig. 1b), **(e)** snow storage from SNODAS for  
 978 CV, **(f)** surface reservoir storage from CDWR for CV, **(g)** GRACE-based estimate of  
 979 groundwater storage for CV, **(h)** total water storage from GRACE for CV, **(i)** vertical land  
 980 motion from GNSS for all available sites in California (CA), and **(j)** for GNSS sites (red) in the  
 981 CV only, and for InSAR pixels in the southern CV from Fig. 5 with a seasonal amplitude larger  
 982 than 3 mm, and lastly, **(k)** groundwater levels from observation wells in CV. See Figure 1 for

983 location of subregions. Each function indicates maximum probability for timing of annual  
984 maximum (a-i, k) or minimum (j) amplitude of the annual signal based on wavelet analysis (Fig.  
985 3 and Fig. S7). Vertical lines represent the mean value for timing of annual maximum.  
986 Distribution is normalized by maximum probability density value and results from year-to-year  
987 variation of the regionally averaged gridded datasets (a-h) and from spatial variation of well and  
988 GNSS data sets (i-k).  
989



990

991 **Figure 7.** Vertical pressure propagation for elevation difference between the Sierra Nevada  
 992 Mountains and the Central Valley aquifers. Normalized pressure change ( $\Delta P'/P_{max}$ ) at different  
 993 depth due to standard 1D calculation of pressure front propagation along mountain block  
 994 recharge conduits in the fractured bedrock of the Sierra Nevada Mountains. Graphs are  
 995 incrementally offset by -1 for each depth. In top groundwater layers, maximum pressure occurs  
 996 on January 22<sup>nd</sup> (DOY 22), which is driven by mean annual water availability in the recharge  
 997 area (Fig. 6b). Table to the right indicates DOY and time delay of the pressure propagation to  
 998 depth of 300-2000 m. Given a hydraulic diffusivity  $\kappa = 0.3 \text{ m}^2/\text{s}$  (reasonable for fractured  
 999 granite bedrocks), the pressure front needs  $\sim 0.6$  (1.2, 1.6) months to propagate to depth of 600  
 1000 (1300, 2000) m. A smaller hydraulic diffusivity would lead to a slower propagation to depth and  
 1001 vice versa, examples for  $\kappa = 0.5, 0.1 \text{ m}^2/\text{s}$  are shown in Figure S14.